

# POLITECNICO DI TORINO

Collegio di Ingegneria Chimica e dei Materiali

**Corso di Laurea Magistrale  
in Ingegneria Chimica e dei Processi Sostenibili**

Tesi di Laurea Magistrale

## **The role of ceria-based catalysts in oxidation reactions**



### **Relatori**

prof. Samir Bensaid

prof. Marco Piumetti

### **Candidato**

Sabrina Ballauri

Ottobre 2020



## Riassunto in italiano

L'obiettivo principale di questa tesi è quello di studiare e comparare i diversi sistemi catalitici al fine di trovare il miglior catalizzatore per l'ossidazione dei principali inquinanti provenienti sia da fonti mobili che stazionarie. Il lavoro è stato suddiviso in diverse sezioni atte a una migliore comprensione e scorrevolezza degli argomenti trattati. Nella prima parte sono descritte le principali caratteristiche delle sostanze inquinanti emesse trattando, in particolar modo, la loro formazione e la loro pericolosità sia per l'ambiente che per la salute umana. Essa è seguita da una trattazione inerente alle principali soluzioni tecnologiche per la loro rimozione e ai diversi catalizzatori ad alta prestazione utilizzati. È, inoltre, presente un capitolo riguardante la caratterizzazione dei materiali catalitici che comprende le tecniche per la determinazione dell'area superficiale nonché le procedure a temperatura programmata quali riduzione, ossidazione e desorbimento. In aggiunta, sono descritte le tecnologie di microscopia elettronica e le differenti tecniche spettroscopiche con particolare approfondimento sulla spettroscopia IR. La sezione di caratterizzazione è seguita poi da uno studio approfondito sui catalizzatori a base ceria trattando le loro peculiari e uniche proprietà, i diversi metodi di preparazione e le prestazioni catalitiche. Dato che queste ultime possono essere ulteriormente migliorate con l'aggiunta di dopanti metallici, è prevista un'apposita sezione dedicata ai catalizzatori a base ceria modificata. Un successivo capitolo riguarda, invece, le prestazioni dei metalli nobili depositati su supporti a base ceria mentre l'ultima parte è focalizzata sullo studio dei diversi meccanismi di reazione attraverso la descrizione degli intermedi formatosi durante le diverse ossidazioni catalitiche.

Oggi giorno l'inquinamento ambientale è un problema molto discusso e sta raggiungendo tenori preoccupanti a livello mondiale. Considerando che le emissioni delle sostanze inquinanti derivano sia da fonti mobili che stazionarie, esse risultano caratterizzate da diverse quantità e composizioni. In particolar modo, le fonti stazionarie comprendono un vasto range di strutture che si estende dalle abitazioni domestiche e dalle piccole imprese fino alle grandi industrie. I principali inquinanti prodotti sono il monossido di carbonio (CO), i combustibili incombusti (HCs), gli ossidi di zolfo e azoto ( $SO_x$  e  $NO_x$ ), i composti organici volatili (VOCs) e, in alcuni casi, particelle di particolato. Per quanto riguarda le emissioni da fonti mobili, invece, il settore automobilistico è uno tra i più importanti settori industriali a livello mondiale, sebbene il numero totale di auto vendute sia diminuito soprattutto negli ultimi due anni a seguito di un picco registrato nel 2018. Le fonti mobili sono responsabili delle emissioni di CO, HC e  $NO_x$ . In questo contesto, nell'ambito del settore automobilistico, i motori a combustione interna che utilizzano diesel come combustibile (motori diesel o ad accensione spontanea) presentano diversi punti positivi come un'alta efficienza energetica, una buona durata e un basso costo operativo. Inoltre, questi dispositivi consentono una minore produzione di CO e HC rispetto ai convenzionali motori ad accensione comandata grazie alle loro particolari condizioni operative che vengono comunemente definite "lean", caratterizzate, quindi, dall'impiego di un largo eccesso di ossigeno. I motori diesel, tuttavia, sono i principali responsabili delle emissioni di ossidi di azoto e particolato che possono causare seri problemi sia per l'ambiente che per la salute umana. A questo proposito, durante gli anni sono state intraprese diverse soluzioni finalizzate a minimizzare la presenza di questi composti inquinanti nell'atmosfera. Tra questi, l'ossidazione catalitica gioca un ruolo fondamentale nel campo della catalisi ambientale per il controllo delle emissioni sia da fonti mobili che stazionarie. Essa, in termini generali, consiste nella reazione tra gli inquinanti e l'ossigeno atmosferico con la formazione di anidride carbonica e acqua in presenza di un catalizzatore. La scelta del sistema catalitico dipende dalle diverse applicazioni e soprattutto dalle condizioni operative in cui viene utilizzato rendendo i metodi

di sintesi e la caratterizzazione dei diversi materiali strumenti fondamentali nel campo della catalisi eterogenea.

Per quanto riguarda le emissioni da fonti mobili, nei motori ad accensione spontanea la presenza di zone più “ricche” di combustibile nella camera di combustione può portare alla formazione di CO e HCs a causa della miscelazione non perfettamente omogenea tra combustibile e comburente. Inoltre, queste condizioni possono causare la nascita di strutture policicliche che costituiscono gli elementi costitutivi del particolato. Queste possono combinarsi tra loro dando origine alla formazione di particelle di forma sferica che porteranno, in seguito a fenomeni di coalescenza, alla nascita di aggregati con dimensione compresa tra 0.1 e 10  $\mu\text{m}$ . Il particolato è caratterizzato da una complessa struttura la cui composizione cambia fortemente a seconda delle diverse condizioni operative del motore. Esso è costituito prevalentemente da agglomerati carboniosi (41%) che raccolgono sulla loro superficie differenti sostanze come combustibile incombusto (7%), olio lubrificante (25%), acqua (14%) e composti inorganici costituiti da ceneri e sostanze solforate (13%), come rappresentato in Figura 2.2 della tesi. La frazione di combustibile incombusto e di olio lubrificante vengono in genere racchiuse nel termine “frazione organica solubile” (SOF) e la sua composizione può variare a seconda del combustibile e delle condizioni operative. In linea generale, il particolato viene classificato in base alla dimensione delle particelle di cui è costituito in quanto esse possono causare problemi di diversa entità sia sull’ambiente che sulla salute umana.

Gli ossidi di azoto sono altri importanti inquinanti prodotti dai motori diesel. Essi sono costituiti per la maggior parte (circa 95%) da NO e possono essere formati in accordo a tre principali meccanismi:

- $\text{NO}_x$  termici derivanti dal meccanismo radicalico di Zeldovich;
- $\text{NO}_x$  veloci dovuti alla reazione dell’azoto con idrocarburi incombusti di tipo radicalico;
- $\text{NO}_x$  formati da composti azotati presenti nel combustibile.

Al fine di minimizzare le emissioni di questi inquinanti, l’Unione Europea ha introdotto negli anni limiti sempre più stringenti combinati a test di emissione sempre più sofisticati al fine di minimizzare la differenza, in termini di emissioni, tra le condizioni di prova e quelle reali. I limiti europei di emissione per le automobili alimentate sia a benzina che a gasolio sono riportati in Figura 2.4 del testo.

I composti organici volatili (VOCs) rappresentano, invece, uno dei principali problemi riguardanti le emissioni da fonti stazionarie. Il termine VOCs racchiude un grande numero di composti chimici provenienti da diversi settori industriali. Essi sono caratterizzati, in accordo con l’Unione Europea, da una pressione di vapore maggiore o uguale a 0.01 kPa a 293.15 K. La natura e il tipo di queste sostanze dipendono fortemente dal processo industriale da cui provengono. Il rilascio di VOCs in atmosfera può causare seri problemi ambientali. I composti alogenati, infatti, sono una delle principali cause della riduzione dell’ozono stratosferico. In aggiunta, i composti classificati come tossici e/o cancerogeni sono responsabili di seri danni per l’uomo.

In merito alle avanzate tecnologie adottate per la rimozione degli inquinanti, il sistema più utilizzato nei motori diesel consiste in un monolita ceramico chiamato DOC. Le pareti di questo dispositivo sono impregnate da un supporto poroso su cui vengono dispersi i metalli nobili attivi per le reazioni di ossidazione catalitica. Questo sistema permette l’abbattimento di HCs, CO, VOCs e la frazione organica solubile di cui è costituito il particolato. Per rispettare i limiti di emissione di quest’ultimo, partendo dalla legislazione Euro 4, è stato introdotto il filtro antiparticolato (DPF). Quest’ultimo è costituito da un monolita a canali ciechi alternati di carburo di silicio in grado di filtrare i composti carboniosi con elevata efficienza. Considerando

che il particolato brucia spontaneamente in aria a temperature superiori a 600-620°C e che questo range non viene normalmente raggiunto dai gas esausti provenienti da questo tipo di motore, i catalizzatori possono giocare un importante ruolo nella riduzione della sua temperatura di ossidazione. In questo contesto, sono stati testati e brevettati diversi sistemi come l'aggiunta di additivi o l'impregnazione del filtro attraverso particolari materiali senza però riuscire a condurre la reazione a così basse temperature. Risulta, quindi, indispensabile l'utilizzo di un sistema di rigenerazione del filtro basato su post-iniezioni di combustibile atte ad aumentare la temperatura del sistema e a promuovere la combustione del particolato. Per evitare la rigenerazione termica, la Johnson Matthey ha brevettato un interessante sistema che consiste nella rigenerazione continua del DPF tramite l'utilizzo di NO<sub>2</sub> come potente mezzo ossidante. Questa specie, infatti, può essere prodotta attraverso l'introduzione nel sistema DOC di una quantità maggiore di metallo nobile in grado di ossidare l'NO in NO<sub>2</sub> in accordo all'Equazione (3.1) descritta nel testo.

Durante gli anni, la tecnica più utilizzata per la riduzione degli NO<sub>x</sub> provenienti dai gas di scarico dei motori diesel è stata la ricircolazione dei gas esausti (EGR). Secondo questa tecnica, una frazione dei gas fuoriuscenti dal sistema è, previo raffreddamento, rinviata in camera di combustione in modo da evitare la formazione della quota parte di ossidi di azoto termici. Questo metodo risulta però responsabile di una maggiore produzione di particolato date le non ottime condizioni operative del motore. Sebbene questa procedura sia stata per diversi anni in grado di rispettare i limiti previsti dall'Unione Europea, al giorno d'oggi, non è più sufficiente. Sono state quindi studiate altre tecnologie atte ad un più efficace abbattimento degli ossidi di azoto. La prima riguarda l'introduzione nell'autoveicolo del sistema SCR tipico degli impianti stazionari. L'iniezione di urea a valle del filtro antiparticolato permette, grazie ad una reazione di idrolisi, la formazione di ammoniaca che risulta un ottimo agente per la trasformazione degli NO<sub>x</sub> in azoto molecolare. La reazione viene condotta in un particolare letto catalitico costituito da zeoliti dopate con rame. È infine presente un sistema ossidativo in grado di abbattere l'eventuale residuo di ammoniaca non utilizzato nella reazione evitando la sua dispersione nell'ambiente. Il sistema LNT rappresenta, invece, la seconda tecnologia testata. Esso è tipicamente costituito da un metallo nobile, un elemento di stoccaggio ed un supporto ad alta area specifica. Grazie alla presenza del metallo nobile, l'NO proveniente da motore è ossidato a NO<sub>2</sub> che verrà successivamente stoccato ed intrappolato dal catalizzatore in forma di nitrati. La rigenerazione del sistema è basata su post-iniezioni di combustibile finalizzate ad aumentare la temperatura del mezzo catalitico promuovendo la decomposizione dei nitrati. Questi verranno successivamente ridotti ad azoto molecolare sui siti di metallo nobile grazie alla presenza di agenti riducenti come idrogeno, CO e HC.

I monoliti a nido d'ape costituiscono i principali sistemi per l'abbattimento dei VOCs prodotti da fonti stazionarie grazie alla combinazione di alte performance, limitate perdite di carico e bassi costi operativi e di fabbricazione. Questi sistemi sono solitamente affiancati da un bruciatore a metano in modo da portare il sistema, in particolar modo nelle fasi di avviamento, alla temperatura ottimale per il buon funzionamento del catalizzatore.

Lo studio del miglior sistema catalitico da utilizzare per l'abbattimento dei vari inquinanti dipende da vari fattori come il contesto operativo e il processo chimico da cui essi derivano. L'ossidazione del particolato è una complessa e singolare reazione in quanto coinvolge la presenza di due fasi solide (catalizzatore e matrice carboniosa) e una fase gassosa (l'ossigeno atmosferico). Questa reazione è, inoltre, influenzata dal tipo di contatto tra materiale catalitico e particolato che tipicamente è di tipo "loose" nelle normali condizioni di lavoro del DPF. Un contatto di tipo "tight" risulta invece utile nel caso in cui si voglia studiare l'attività intrinseca del catalizzatore senza considerare altri fenomeni limitanti la reazione. I catalizzatori a base

ceria modificata tramite l'introduzione del praseodimio nella struttura risulta uno dei più attivi sistemi per l'abbattimento del particolato.

Diversi catalizzatori sono stati studiati per l'ossidazione del NO a NO<sub>2</sub> che è, come descritto precedentemente, uno degli step chiave per l'abbattimento del particolato. Il platino supportato da allumina, titania o silice risulta il materiale più performante per questa reazione data la sua elevata intrinseca attività. In aggiunta, sono stati studiati sistemi a base di ossidi metallici o perovskiti per fronteggiare l'elevato costo dei metalli nobili.

In merito all'ossidazione dei VOCs la scelta del materiale catalitico risulta piuttosto difficile in quanto generalmente è necessario fronteggiare il problema dell'effetto di miscela. Spesso, infatti, i processi tecnologici si trovano a trattare sistemi multicomponenti e le prestazioni catalitiche ottenute dall'ossidazione di un singolo composto possono, in presenza di altre specie, diminuire, aumentare o rimanere invariate. In linea generale, gli alcoli, i composti aldeidici ed i chetoni risultano abbastanza semplici da ossidare. Al contrario, gli alcani e i composti alogenati sono molto difficili da abbattere. I catalizzatori utilizzati per minimizzare la presenza di VOCs nell'atmosfera si dividono in due principali categorie: i metalli nobili e gli ossidi metallici. Lo studio di questi ultimi risulta particolarmente interessante per l'ottenimento di un sistema catalitico stabile, a basso prezzo e con attività comparabili a quelle dei più costosi metalli preziosi.

Una volta sintetizzato un catalizzatore, le tecniche di caratterizzazione sono le tecnologie più avanzate e sofisticate per confermare la buona riuscita della sintesi, per analizzare le proprietà dei diversi sistemi e per testare le loro performance catalitiche. Introdotte per la prima volta nel 1940, queste procedure sono diventate negli anni sempre più fondamentali nel campo della catalisi.

Come descritto in dettaglio nella Sezione 5 della tesi, esse permettono la determinazione dell'area superficiale dei materiali che è uno dei parametri più importanti per le reazioni catalitiche. Le molecole gassose dei reagenti devono, infatti, diffondere nelle porosità del campione in modo da raggiungere i diversi siti attivi su cui successivamente reagiranno. Il risultato dell'analisi, come mostrato in Figura 5.1 della tesi, consiste nell'ottenimento di curve in cui la quantità di azoto fisisorbito è rappresentata in funzione della pressione relativa (pressione assoluta/pressione di saturazione). In aggiunta, il materiale studiato è classificabile come microporoso, mesoporoso e macroporoso in base alla dimensione delle sue porosità.

D'altra parte, le tecniche in temperatura programmata permettono di valutare la reattività e la stabilità delle diverse specie formate sulla superficie catalitica durante una reazione al variare della temperatura. Tipicamente, il catalizzatore viene posto in un reattore (fornace) con velocità di riscaldamento controllabile (in generale 5-20 °C min<sup>-1</sup>) in contatto con una portata gassosa costante. La riduzione in temperatura programmata (TPR) permette lo studio delle proprietà redox del bulk e della superficie dei materiali. Essa è condotta trattando il campione con una corrente contenente idrogeno o CO. D'altro canto, le ossidazioni a temperatura programmata (TPO) sono utilizzate per la valutazione dell'attività catalitica dei vari sistemi e per studiare l'ottimale temperatura di rigenerazione di un catalizzatore soggetto a disattivazione da coking. I desorbimenti a temperatura programmata (TPD), invece, forniscono indicazioni sulla forza relativa del legame tra le differenti specie presenti nella fase gassosa e la superficie catalitica. Per concludere, l'analisi termo-gravimetrica (TGA) è basata sulla perdita di massa osservata sottoponendo il campione ad un incremento di temperatura. Questa procedura fornisce indicazioni sulle percentuali in peso delle diverse specie costituenti un composto eterogeneo e, se abbinata a particolari software, permette la determinazione dei parametri cinetici delle reazioni catalitiche.

La microscopia elettronica, invece, fornisce un'immagine ad alta risoluzione dei materiali sintetizzati ottenendo informazioni qualitative dei diversi campioni. In base all'energia con cui

vengono accelerati gli elettroni utilizzati e alla configurazione del microscopio, le tecniche microscopiche possono essere distinte in due categorie: la microscopia a trasmissione elettronica (TEM) e quella a scansione (SEM). Nella prima vengono utilizzati elettroni ad alta energia (circa 100 keV), mentre nella seconda il fascio di elettroni urta il materiale con un range di energia compreso tra 0.5 e 30 keV. Le analisi TEM sono utilizzate per lo studio delle superfici catalitiche, per la determinazione della loro morfologia, dei vari piani esposti e, infine, per confermare la buona dispersione di metallo attivo. D'altro canto, nella microscopia SEM la presenza di elettroni retrodiffusi uniti alla caratteristica emissione di raggi X fornisce informazioni indicative inerenti alla composizione elementare del campione.

Le tecniche spettroscopiche sono diventate negli anni sempre più fondamentali per lo studio dei catalizzatori eterogenei. Le condizioni operative delle prime analisi prevedevano l'utilizzo di un alto livello di vuoto causando una pronunciata differenza tra le condizioni di prova e quelle di impiego reali dei catalizzatori. Al giorno d'oggi, grazie ad analisi in situ e in operando è possibile ridurre al minimo questa incongruenza. La diffrazione a raggi X (XRD) è basata sullo scattering elastico dei fotoni di raggi X da parte degli atomi di un reticolo ordinato. Essa è quindi essenziale per l'identificazione delle diverse fasi presenti nei materiali cristallini, in cui gli atomi sono disposti su dei piani ordinati caratterizzati da una specifica triade di indici di Miller. Inoltre, questa tecnica permette di ricavare informazioni legate alla dimensione dei cristalliti utilizzando la formula di Debye-Scherrer riportata nell'Equazione (5.9) della tesi. La seconda importante tecnica spettroscopica utilizzata per la caratterizzazione dei materiali catalitici è la spettroscopia fotoelettronica a raggi X (XPS). In accordo alla tecnologia XPS, gli elettroni degli atomi costituenti il campione possono assorbire fotoni di raggi X immagazzinando abbastanza energia per lasciare il sistema. Misurando l'energia cinetica di questi ultimi e conoscendo l'energia dei fotoni incidenti è possibile calcolare l'energia di legame (binding energy) tra elettrone e sistema. Dato che ogni elemento è caratterizzato da tipiche energie di legame, questa analisi permette lo studio della composizione elementare superficiale dei campioni. In aggiunta, sono ricavabili informazioni relative allo stato di ossidazione e all'intorno chimico degli elementi.

Due avanzate e sofisticate tecniche spettroscopiche utilizzate nell'ambito catalitico sono la spettroscopia Raman e la spettroscopia IR. Questi metodi, se condotti in situ o in operando, sono in grado di fornire indicazioni dettagliate sui diversi intermedi di reazione stabili che si formano sulla superficie del catalizzatore variando la temperatura del sistema. Le analisi Raman sono basate sullo studio dell'effetto Raman. In particolare, quanto un fotone della luce incidente interagisce con un fonone del materiale può subire un processo di scattering inelastico, di conseguenza, la sua lunghezza d'onda risulterà differente rispetto a quella della luce incidente. Quindi, durante l'interazione della luce con il campione, il sistema si sposta da uno stato di vibrazione fondamentale a uno eccitato tornando poi ad uno stato differente rispetto a quello di partenza. Le analisi Raman sono utili per lo studio delle specie attive formate sulla superficie del catalizzatore e in particolare per la determinazione dei siti difettivi presenti nel materiale. La spettroscopia IR è invece basata sull'interazione tra le radiazioni IR e le molecole presenti nel campione. Come risultato, queste ultime possono amplificare il loro naturale moto oscillatorio in termini di distanze interatomiche e angoli di legame. Perché la vibrazione risulti attiva questo movimento di vibrazione deve essere correlato ad una variazione del momento di dipolo della molecola. Sono possibili due tipologie di vibrazioni: le vibrazioni di stretching causate da un allungamento ritmico lungo l'asse di legame e vibrazioni di bending legate a variazioni dell'angolo di legame. Le prime sono contraddistinte da picchi a numeri d'onda maggiori rispetto alle altre. Questa tecnica permette lo studio dei materiali catalitici secondo tre differenti livelli. In primo luogo, essa è utilizzata per analizzare le caratteristiche superficiali dei catalizzatori. Questa tecnologia permette, inoltre, l'identificazione della natura e il tipo di siti acidi e basici presenti testando il campione attraverso l'interazione con specifiche molecole

sonda. Per la determinazione dei siti acidi vengono spesso utilizzati il CO, l'ammoniaca e, in passato, la piridina. I siti basici possono essere, invece, studiati tramite interazione con CO<sub>2</sub> e acetonitrile. Oltre ad un'analisi qualitativa, gli spettri FTIR derivanti dalla reazione con le molecole sonda permettono un'analisi quantitativa del numero di siti acidi e basici. Come terzo punto, ma non meno importante, performando analisi in situ è possibile descrivere, in modo abbastanza accurato, il meccanismo delle reazioni studiate attraverso lo studio degli intermedi formatosi sulla superficie del campione. La spettroscopia IR applicata alla catalisi ha iniziato ad essere particolarmente importante partendo dal XX secolo. Sebbene la radiazione IR sia suddivisa in tre segmenti comprendenti lunghezze d'onda da 13333 e 10 cm<sup>-1</sup>, la regione del medio infrarosso (da 4000 a 400 cm<sup>-1</sup>) è la più importante nell'uso di questa spettroscopia vibrazionale.

Tra i diversi campi di impiego delle terre rare e dei loro ossidi, la catalisi rappresenta la loro terza importante applicazione tecnologica. Essi consistono in 17 elementi e, tra questi, il cerio e il lantanio costituiscono circa i due terzi del loro consumo mondiale. L'ossido di cerio o ceria è uno dei materiali più studiati nel campo della catalisi ambientale, in particolar modo, per le reazioni di ossidazione catalitica. Esso può essere utilizzato come supporto o come catalizzatore vero e proprio. Inoltre, l'incorporazione nella sua struttura di cationi metallici consente la formazione di catalizzatori stabili con alte prestazioni. La ceria stechiometrica (CeO<sub>2</sub>) è contraddistinta da un colore giallo e presenta una struttura a fluorite con gli atomi disposti in celle unitarie cubiche a facce centrate. Ad alte temperature e in ambienti riducenti essa può rilasciare ossigeno con la formazione delle ceria non-stechiometrica avente formula CeO<sub>2-x</sub> con x compreso tra 0 e 0.5. Le singolari proprietà redox dell'ossido di cerio sono studiate in molti laboratori di ricerca; esso può velocemente e facilmente stoccare e rilasciare ossigeno grazie alla presenza della coppia Ce<sup>4+</sup>/Ce<sup>3+</sup> mantenendo una buona stabilità strutturale attraverso il processo completamente reversibile descritto nell'Equazione (6.1) del testo. Questa sua peculiare proprietà prende il nome di "capacità di stoccaggio di ossigeno" (OSC) e dipende da diversi fattori tra cui l'inserimento di un metallo nella struttura, nonché aspetti geometrici e operativi. La spettroscopia IR consente di identificare se la ceria è nella sua fase ossidata o ridotta (stechiometrica e non-stechiometrica). Infatti, la presenza dell'accentuata banda centrata a 2115 cm<sup>-1</sup> indica la presenza di Ce<sup>3+</sup> caratterizzante la sua forma ridotta.

Le tecniche di sintesi odierne consentono di sintetizzare la ceria in forma di nanoparticelle in accordo ad un preciso controllo dei differenti parametri di sintesi come ad esempio pressione, pH e temperatura. Questi innovativi metodi promuovono la formazione di precise nano-forme caratterizzate dall'esposizione di specifici piani cristallini aventi diversa attività. In particolare, grazie alla maggiore esposizione dei piani (110) e (100) le nanofibre e i nanocubi di ossido di cerio risultano molto più attivi rispetto ai nano-ottaedri costituiti, invece, dall'esposizione preferenziale di facce di tipo (111). Queste ultime risultano decisamente più stabili delle precedenti. Il metodo idrotermale è la più comune procedura di sintesi volta all'ottenimento di catalizzatori nanostrutturati. Generalmente questo processo prevede l'utilizzo di un sale di cerio che viene disciolto in acqua in presenza di una base. Il materiale ottenuto è successivamente posto in un'autoclave per 20-50 ore a 100-200°C. Questo periodo di tempo è chiamato "fase di aging". Il catalizzatore così ottenuto è poi lavato con etanolo ed acqua e calcinato a alte temperature. La temperatura della fase di aging è importante per l'ottenimento di nanomateriali contraddistinti da diverse morfologie. Precisamente, a temperature prossime ai 100°C si ottengono primariamente nano-ottaedri e nanocubi, mentre a circa 180°C è favorita la formazione di nanofibre. Lo sviluppo dei nano-ottaedri è favorito a pH bassi mentre alti pH promuovono la realizzazione di nanofibre. Le immagini TEM dei nano-ottaedri, nanocubi e nanotubi di ceria sono riportati in Figura 6.3 del testo e ripresentati nelle righe sottostanti.

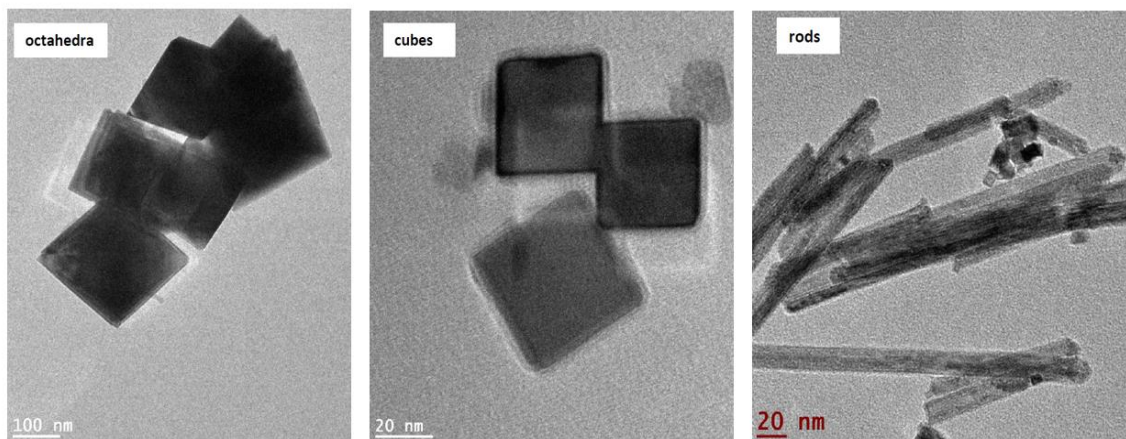


**Figure 1:** immagini TEM di nano-ottaedri, nanocubi e nanofibre di ceria adattata da ref. [62]

Un'altra tecnica per la produzione di nanoparticelle di ceria è la solution combustion synthesis (SCS). In essa un precursore della ceria e un combustibile vengono disciolti in un solvente e successivamente trattati ad alta temperatura. Il metodo SCS non consente la produzione di nanostrutture, ma origina una morfologia spugnosa dovuta al veloce rilascio di una grande quantità di gas. Le immagini SEM di questo tipo di materiali sono presentate in Figura 6.7 del testo.

Per quanto riguarda la caratterizzazione dei catalizzatori a base ceria, il fisisorbimento di azoto a 77 K mostra una bassa area superficiale dei catalizzatori nanostrutturati, mentre un più alto valore è osservato per quelli sintetizzati tramite SCS. L'analisi XRD mostra la presenza dei piani (111), (200), (220), (311), (222) e (400) tipici della struttura a fluorite della ceria. L'analisi Raman della ceria idrotermale, ottenuta utilizzando una sorgente monocromatica con lunghezza d'onda nel visibile, mostra un'intensa banda centrata a  $462\text{ cm}^{-1}$  data dalla vibrazione del legame Ce-O caratterizzante l'ossido di cerio. Questa viene definita come  $F_{2g}$ . Lo spettro ottenuto da un'analisi Raman-UV risulta, invece, più sensibile alla presenza di difetti strutturali nel materiale. La loro presenza è osservata grazie alla banda D a  $592\text{ cm}^{-1}$ . Essa viene assegnata a difetti intrinseci dell'ossigeno di tipo Frenkel. Il rapporto tra l'intensità della banda D e quella del picco  $F_{2g}$  fornisce un'indicazione del contenuto relativo di difetti nei vari materiali, in particolare più alto è questo rapporto e più elevato è il numero di siti difettivi presenti. Le nanofibre di ceria presentano un rapporto  $I_D/I_{F_{2g}}$  maggiore rispetto ai nanocubi, che a loro volta presentano più difetti in confronto ai nano-ottaedri. Questo è stato anche dimostrato tramite l'interazione del campione con la molecola sonda metanolo studiata tramite analisi FTIR. L'adsorbimento del metanolo a temperatura ambiente, infatti, promuove la formazione di diverse specie sulla superficie della ceria. La presenza o l'assenza di queste può essere assegnata all'esistenza o meno di difetti strutturali, come le vacanze di ossigeno. L'assorbimento di piridina come molecola sonda ha invece dimostrato l'assenza di siti acidi di Brønsted sulla ceria, ma ha confermato la presenza di siti di Lewis. Lo spostamento dei picchi verso più alte frequenze vibrazionali, in confronto al picco centrato a  $1582\text{ cm}^{-1}$  della piridina libera, risulta circa lo stesso per le tre nanostrutture che presentano quindi simile forza acida.

D'altro canto, per quanto riguarda le prestazioni catalitiche le nanofibre presentano generalmente maggiore attività in confronto alle altre nanostrutture. Recenti studi hanno però dimostrato l'efficiente abbattimento del monossido di carbonio su particolari nanocubi di ceria. Essi, in seguito al trattamento termico di calcinazione, risultano costituiti da bordi e angoli arrotondati. L'esposizione sia di piani (100) che (110) rende queste strutture molto interessanti dal punto di vista catalitico. In aggiunta, i catalizzatori preparati tramite sintesi idrotermale, presentano maggiore attività di quelli sintetizzati attraverso la tecnica SCS a causa della loro

maggior intrinseca attività. L'ossidazione catalitica del particolato sulla ceria viene solitamente performata in contatto di tipo "tight" - per studiare l'attività intrinseca del catalizzatore - e in contatto di tipo "loose" - per valutare le effettive prestazioni del sistema catalitico. Anche in questo caso, i nanocubi hanno dimostrato attività superiore alle altre nanostrutture ed ai campioni preparati tramite SCS. Per quanto riguarda quest'ultimo metodo, la scelta del solvente e del combustibile può contribuire in modo positivo o negativo alla reazione di ossidazione del particolato. L'uso di glicina come combustibile e acetone come solvente permette di ottenere il minore valore di  $T_{50\%}$ . Campioni di ceria SCS preparati utilizzando glicole etilenico come combustibile hanno dimostrato buona attività nella conversione del naftalene ottenendo una selettività del 100% in  $CO_2$ . A questo proposito, nelle ossidazioni catalitiche dei VOCs la selettività è un parametro fondamentale in quanto una combustione non completa potrebbe portare alla formazione di prodotti secondari aventi pericolosità maggiore rispetto al composto di partenza.

Il metodo più efficace per rendere i catalizzatori a base ceria più attivi e performanti è l'incorporazione nella struttura di dopanti metallici. È possibile ottenere ossidi misti attraverso l'aggiunta di terre rare come terbio e praseodimio o di metalli di transizione quali zirconio, rame e manganese. I catalizzatori di ceria modificata possiedono caratteristiche strutturali ed energetiche diverse in confronto alla ceria pura. L'aggiunta di elementi differenti dal cerio causa un incremento della proprietà di stoccaggio di ossigeno a causa della formazione di siti difettivi, in particolare di vacanze di ossigeno. Il terbio e il praseodimio risultano particolarmente interessanti in quanto essi coesistono, come la ceria, in due differenti stati di ossidazione (3+ e 4+) sia nei loro ossidi puri che nelle soluzioni solide. Di conseguenza l'uso di questi materiali permette una maggiore mobilità dell'ossigeno ed un aumento delle proprietà redox del sistema. A questo proposito, l'ossido di praseodimio o praseodimia ha mostrato elevata importanza tra gli ossidi dei metalli delle terre rare. Esistono differenti ossidi stechiometrici aventi formula  $Pr_nO_{2n-2}$  con  $n = 4, 7, 9, 10, 11, 12, \infty$  e i due casi limite sono rappresentati da  $Pr_2O_3$  e  $PrO_2$ . L'ossido di praseodimio più stabile a temperatura ambiente è il  $Pr_6O_{11}$  che può essere visto come un campione modificato della struttura fluoritica  $PrO_2$  caratterizzato da un deficit di ossigeno. Come accennato precedentemente, la praseodimia può contenere cationi con due diversi stati di ossidazione:  $Pr^{4+}$  e  $Pr^{3+}$ . La veloce transizione tra questi due stati di ossidazione rende il  $Pr_6O_{11}$  il catalizzatore con più alta mobilità di ossigeno tra gli ossidi dei lantanidi. Inoltre, esso risulta più riducibile rispetto alla ceria. La praseodimia può essere preparata sia con tecniche tradizionali, come la calcinazione del nitrato o la procedura sol-gel, che con sintesi più sofisticate. Queste ultime includono l'approccio di Pechini e il metodo dei citrati. È interessante notare, però, che tutte queste tecniche portano alla formazione di strutture molto simili sia dal punto di vista catalitico che strutturale. L'ossido di praseodimio può essere anche ottenuto tramite procedura idrotermale ottenendo una morfologia caratterizzata prevalentemente da nanofibre.

I catalizzatori ceria-praseodimia risultano molto interessanti dal punto di vista della catalisi ossidativa. In letteratura sono state studiate la caratterizzazione e le prestazioni catalitiche di campioni Ce-Pr preparati con tre diverse tecniche: idrotermale, SCS e co-precipitazione. Questi ossidi sono stati sintetizzati con diverse composizioni in accordo alla formula generale  $Ce_xPr_{1-x}O_{2-\delta}$ . Le composizioni trattate sono descritte in dettaglio nella Tabella 7.2 della tesi. Tramite analisi XRD è interessante notare che, partendo dalla ceria pura e aumentando progressivamente il contenuto di praseodimio, non tutte le composizioni mostrano la formazione di una soluzione solida tra i due elementi. Questo può essere dimostrato dalla segregazione di fase presente nel campione  $Ce_{0.2}Pr_{0.8}O_{2-\delta}$ . Infatti, i diffrattogrammi a raggi X

della ceria-praseodimia ottenuta tramite metodo di co-precipitazione mostrati in Figura 7.8 della tesi e qui sotto riportati, mostrano la presenza di doppi picchi a circa 33, 47 e 56°.

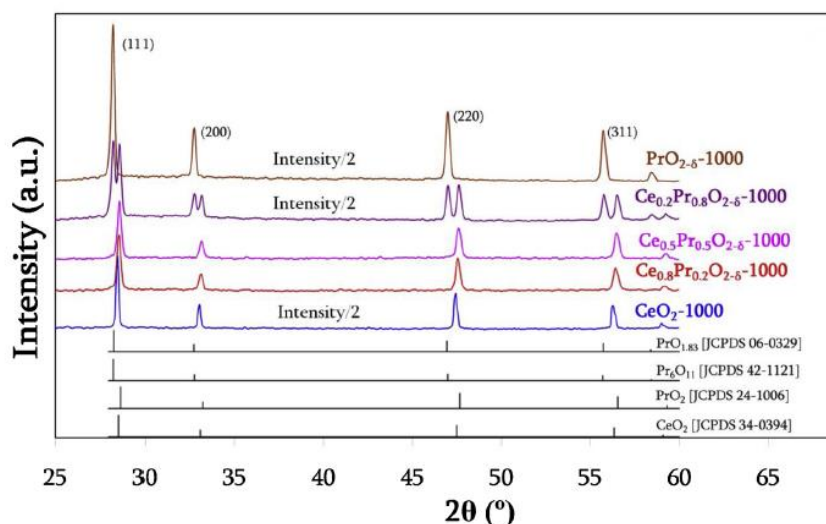


**Figure 2:** Diffratogrammi a raggi X della ceria-praseodimia ottenuta tramite metodo di co-precipitazione adattata da ref. [88]

Le analisi di microscopia elettronica mostrano che la ceria preparata tramite processo idrotermale con temperatura di aging di 180°C risulta sottoforma di nanocubi, in accordo alla procedura di sintesi precedentemente descritta. Aggiungendo il praseodimio nel sistema è possibile notare la formazione di strutture fibrose sui lati dei cubi. Questa morfologia diventa prevalente con elevate quantità di Pr. Analisi Raman eseguite sul campione ottenuto tramite co-precipitazione mostrano che la banda  $F_{2g}$  tipica della ceria diminuisce la sua intensità, diventa sempre più ampia e subisce uno spostamento verso minori numeri d'onda aumentando il quantitativo di praseodimio nel sistema. La diminuzione di intensità è dovuta alla perdita di simmetria della struttura a causa dell'introduzione di un diverso catione e la banda subisce uno spostamento causato dalla maggiore concentrazione di specie  $Pr^{3+}$  che vengono inevitabilmente formate essendo l'ossido di praseodimio più riducibile della ceria.

L'ossido di praseodimio si è rivelato un buon catalizzatore per l'ossidazione dell'NO. Partendo dalla ceria pura e aggiungendo quantità sempre maggiori di questo elemento la produzione di  $NO_2$  viene registrata a più basse temperature e in maggiore quantità, come illustrato in Figura 7.11 della tesi. Il catalizzatore  $Pr_{0.5}Ce_{0.5}O_{2-\delta}$  preparato tramite sintesi idrotermale risulta il più attivo per l'ossidazione del particolato rispetto alle altre composizioni e ai campioni preparati con tecnica SCS sia conducendo la reazione con contatto di tipo "tight" che di tipo "loose". È bene tenere in considerazione che i motori diesel producono anche una quantità non trascurabile di NO, generalmente compresa tra 100 e 700 ppm. Nelle automobili esso può essere in parte convertito in  $NO_2$  dal platino presente nel sistema DOC, a monte del filtro antiparticolato. Sapendo che il potere ossidante di questa specie è maggiore di quello dell'ossigeno, è bene eseguire i test catalitici in presenza di  $NO_2$  cercando di spingere al massimo la conversione dei composti carboniosi. Il catalizzatore più performante è risultato, anche in questo caso, la Ce-Pr equimolare. La presenza del praseodimio sembra, infatti, favorire l'ossidazione dell'NO con la continua formazione, in situ, di specie  $NO_2$  attive.

Sebbene lo zirconio sia un materiale non riducibile, il suo inserimento nei sistemi ceria-praseodimia migliora l'attività catalitica dei campioni per la creazione di un maggior numero di siti difettivi. Il sistema risulta, in aggiunta, più stabile sia termicamente che strutturalmente. La preparazione di diversi ossidi misti con formula generale  $Zr_{0.1}(Ce_{1-x}Pr_x)_{0.9}O_2$  tramite

metodo sol-gel dimostra che ad alti valori di  $x$ , quindi in presenza di un'alta percentuale di praseodimio, l'area superficiale del campione diminuisce. Mentre la proprietà di OSC presenta un picco a  $x$  pari a 0.5, in accordo con le migliori prestazioni ottenute utilizzando la ceria-praseodimia equimolare rispetto alle altre composizioni. Analisi XPS svolte su altri campioni ceria-zirconia-praseodimia evidenziano che le specie ossigeno attivo di tipo  $\alpha$  sono maggiormente presenti nei catalizzatori preparati tramite procedura idrotermale rispetto a quella SCS che risultano, invece, caratterizzati da una più grande presenza di ossigeno di tipo  $\beta$ . Le prime specie descritte si riferiscono all'ossigeno superficiale debolmente legato alla struttura e di conseguenza molto attivo per le reazioni ossidative, mentre il secondo riguarda l'ossigeno strutturale con minore reattività catalitica.

Per giunta, un recente e avanzato esperimento ha provato la possibilità di produrre catalizzatori in continuo utilizzando reagenti a basso costo. Esso consiste nell'utilizzo di un dispositivo microfluidico basato sull'uso di un reattore multi-ingresso e consente di ottenere campioni con caratteristiche molto più riproducibili in confronto a quelli ottenuti tramite metodi batch.

I catalizzatori ceria-praseodimia-zirconia non si sono rivelati come i migliori sistemi per l'abbattimento del CO e in generale i catalizzatori preparati tramite sintesi idrotermale hanno mostrato attività maggiore in confronto a quelli SCS e ai sistemi preparati nel dispositivo microfluidico. Per quanto riguarda l'ossidazione del particolato, invece, i campioni sintetizzati sia attraverso metodo idrotermale che SCS e caratterizzati dalla formula  $Ce_{0.8}Zr_{0.1}Pr_{0.1}O_2$  si sono rilevati molto attivi per la sua ossidazione. Al contrario, l'aggiunta di praseodimio e zirconio nei campioni preparati tramite reattore microfluidico non ha rivelato particolare attività nell'abbattimento delle sostanze carboniose. Questi catalizzatori, probabilmente, risultano meno performanti a causa della loro non disordinata microstruttura osservabile in Figura 7.21 del testo.

I sistemi binari basati su ossidi di rame e ceria hanno attirato l'attenzione di diversi gruppi di ricerca grazie alla loro elevata attività catalitica nelle reazioni di ossidazione. Essa è dovuta alla presenza di due cicli redox combinati ( $Ce^{3+}/Ce^{4+}$  e  $Cu^{2+}/Cu^+$ ) capaci di promuovere il meccanismo di Mars van Krevelen, tipico delle reazioni ossidative. In questo contesto, nella seconda metà del 1900 è stato introdotto il concetto di cooperazione di fase, secondo cui, in un sistema bifasico, una fase svolge la vera e propria attività catalitica, mentre la seconda è finalizzata a migliorare alcune addizionali proprietà del sistema stesso. La proprietà di OSC risulta migliorata in modo significativo dopo l'inserimento di rame nella struttura della ceria a causa dell'elevata quantità di siti difettivi che si vengono a formare. L'area superficiale di ossidi misti di cerio e rame caratterizzati da diversi rapporti Ce/Cu e preparati tramite metodo SCS risulta diminuire con l'aumentare del quantitativo di rame presente. Simile tendenza è osservata per la dimensione dei cristalliti in quanto il raggio ionico del  $Cu^{2+}$  è minore di quello dei due cationi della ceria. Per giunta, il test  $H_2$ -TPR ha dimostrato che l'introduzione di rame nella struttura promuove la riducibilità del catalizzatore. Le analisi HRTEM di campioni ottenuti tramite sintesi idrotermale, invece, provano che l'aggiunta di rame causa una perturbazione della struttura del campione lungo i bordi e gli angoli delle nanostrutture di ceria. La presenza di siti difettivi è stata, inoltre, confermata tramite la spettroscopia Raman. La frequenza vibrazionale del legame Ce-O cambia in seguito all'introduzione del  $Cu^{2+}$  nella struttura della ceria causando uno spostamento del caratteristico picco  $F_{2g}$  verso minori numeri d'onda. Oltre a ciò, gli spettri mostrano due addizionali bande a 606 e 1154  $cm^{-1}$  assegnate alla formazione di vacanze di ossigeno. Analisi FTIR risultanti dall'interazione del campione con la piridina hanno mostrato la presenza di siti acidi sia di Brønsted che di Lewis sulla superficie del materiale catalitico.

Gli ossidi misti  $CuO-CeO_2$  possono essere anche prodotti partendo da nanoparticelle di rame stabilizzate attraverso un composto organometallico e successivamente depositate sulla ceria

nella forma di CuO. Le immagini TEM hanno confermato una buona distribuzione delle specie CuO sulla superficie di ossido di cerio preparato tramite SCS, mentre è possibile osservare la segregazione di questi domini in seguito alla deposizione sulle nanostrutture di ceria probabilmente a causa della loro bassa area superficiale.

I catalizzatori preparati tramite quest'ultimo metodo hanno dimostrato particolare attività per la reazione di ossidazione di NO a NO<sub>2</sub>. In particolare, il catalizzatore contenente il 5% di rame depositato sulla ceria SCS ha mostrato le migliori performance. Considerando la povera attività della ceria inerente questa reazione, le molecole di NO vengono ossidate grazie alla presenza dei domini di rame. In aggiunta, il catalizzatore 5% Cu/CeO<sub>2</sub>-SCS presenta alta attività catalitica nell'abbattimento del CO. D'altro canto, buone prestazioni sono anche ottenute con il campione Ce<sub>0,6</sub>Cu<sub>0,4</sub> sintetizzato tramite metodo SCS partendo da nitrati di cerio e di rame come precursori. L'ossidazione del particolato, viceversa, sembra diminuire aumentando il contenuto di rame nel sistema catalitico dei campioni preparati tramite sintesi SCS testati in diverso rapporto Ce/Cu a causa della riduzione del numero di centri attivi Ce<sup>4+</sup>/Ce<sup>3+</sup>. L'analisi TPO sui catalizzatori contenenti domini CuO depositati sulla ceria partendo da nanoparticelle di rame stabilizzate tramite composto organometallico in assenza e in presenza di NO<sub>x</sub> ha indicato che l'utilizzo di supporti a base ceria nanostrutturata ottenuta tramite metodo idrotermale risultano più attivi di quelli in cui la fase CuO è stata depositata su catalizzatori SCS a causa della loro più elevata attività intrinseca. Questi ultimi catalizzatori hanno però mostrato che, in presenza di NO<sub>x</sub>, la conversione del particolato diminuisce performando test catalitici successivi e il fenomeno risulta particolarmente accentuato sui campioni contenenti la maggiore quantità di rame. Questo fatto è dovuto alla sinterizzazione delle particelle di CuO che, in seguito a diversi cicli catalitici, subiscono fenomeni di aggregazione e coalescenza. Essendo le nanoparticelle di CuO molto attive nell'ossidazione dell'NO, questa reazione risulta particolarmente inibita. Come conseguenza principale vi è la mancata produzione di NO<sub>2</sub>, attivo agente ossidante per le sostanze carboniose. Infine, riguardo alla distruzione dei VOCs, i catalizzatori a base CuO-CeO<sub>2</sub> preparati tramite SCS si sono rivelati molto attivi per l'ossidazione dell'etilene.

I metalli nobili, come regola generale, sono i catalizzatori più attivi per diversi ambiti della catalisi sebbene, soprattutto negli anni recenti, i diversi gruppi di ricerca stiano continuamente cercando materiali sostitutivi con comparabili performance dato l'alto e variabile costo del platino, del palladio e del rodio. Essi vengono generalmente dispersi su supporti porosi in forma di cluster nanometrici. Quando l'attività catalitica della ceria o della ceria modificata non è sufficiente, è possibile depositare sulla sua superficie questi metalli in grado di promuovere l'attività del sistema.

Il platino viene comunemente depositato sui catalizzatori a base ceria tramite le tradizionali tecniche di impregnazione. Utilizzando una percentuale di metallo nobile minore dell'1%, i picchi dovuti alla presenza di specie Pt e PtO<sub>x</sub> non sono rilevati dall'analisi XRD. Le dimensioni delle particelle di platino disperso sono in genere comprese tra 1 e 4 nm e le immagini HRTEM mostrano il possibile ottenimento di una loro buona dispersione. D'altra parte, le analisi XPS indicano che il più abbondante stato di ossidazione del platino disperso su catalizzatori di ceria nanostrutturati e preparati tramite SCS è 2+ a causa dell'ossidazione del platino con valenza zero nel processo di calcinazione. Questi campioni contengono, in aggiunta, una piccola quantità di Pt<sup>4+</sup>. In particolare, il metallo nobile disperso sulle nanostrutture di ceria è costituito da Pt<sup>2+</sup>, da un significativo quantitativo di Pt<sup>4+</sup> e da una piccola percentuale di Pt<sup>0</sup>.

Il platino è il catalizzatore più attivo per l'ossidazione di NO a NO<sub>2</sub>. È però interessante notare che performance comparabili sono ottenute utilizzando un sistema di ceria-praseodimia nanostrutturata equimolare. Quindi, in questo caso, la sostituzione del platino con la soluzione

solida formata da questi due ossidi metallici può essere considerata come una buona scelta al fine di diminuire i costi globali del sistema catalitico.

D'altro canto, per quanto riguarda l'abbattimento del CO, il platino depositato su ceria SCS risulta più attivo rispetto alla deposizione su ceria nanostrutturata probabilmente a causa dell'elevata area superficiale dei materiali spugnosi.

Come descritto precedentemente, la ceria-praseodimia equimolare è un catalizzatore piuttosto attivo per l'ossidazione del particolato. L'aggiunta di platino a questo sistema ha dimostrato di non fornire ulteriori effetti positivi riguardo all'abbattimento delle sostanze carboniose. La presenza di metallo nobile, tuttavia, permette una maggiore selettività della reazione nella produzione di CO<sub>2</sub> ossidando l'eventuale CO prodotto come intermedio della reazione.

Infine, il platino è uno dei catalizzatori più utilizzati per l'abbattimento dei VOCs. In particolare, l'ossidazione del toluene sulle tre nanostrutture della ceria impregnate con platino si è rivelata particolarmente positiva in presenza di nanofibre.

In accordo al "Intergovernmental Panel on Climate Change" (IPCC) le emissioni di CO<sub>2</sub> variano considerevolmente utilizzando diversi combustibili fossili. Considerando che la produzione di anidride carbonica cresce all'aumentare del numero di atomi di carbonio nel combustibile fossile considerato, il carbone risulta il composto più inquinante mentre il metano quello più rispettoso per l'ambiente. Nel contesto di riduzione delle emissioni di CO<sub>2</sub>, soprattutto negli ultimi anni, l'utilizzo del gas naturale è cresciuto significativamente sebbene il metano si sia rivelato un aggressivo gas serra. È diventato quindi necessario lo studio di un sistema catalitico atto a promuovere l'ossidazione del metano. A questo proposito, i catalizzatori a base palladio emergono come i più attivi campioni testati. I sistemi a base Pd possono cambiare la loro fase termodinamicamente stabile variando la pressione parziale di ossigeno e la temperatura. Diversi studi hanno dimostrato che probabilmente la specie PdO è la più attiva riguardo l'ossidazione del metano, sebbene sia contraddistinta da una bassa stabilità ad alte temperature. Essa, infatti, viene decomposta a palladio metallico a circa 1000 K con una pressione parziale di ossigeno pari a 20 mbar. Questa transizione porta ad una diminuzione delle performance catalitiche del sistema. D'altro canto, però, la specie PdO può essere ripristinata in accordo ad un processo di riossidazione del palladio metallico che può essere promosso tramite l'utilizzo della ceria come supporto su cui disperdere i siti nobili attivi. In linea generale, i diversi esperimenti hanno mostrato che il tipo di supporto su cui il palladio viene disperso non influisce né positivamente né negativamente sullo sviluppo della reazione. Utilizzando supporti a base ceria, invece, oltre a prevenire la perdita di fase attiva ad altre temperature, l'interazione con il palladio ne promuove la sua riducibilità. La determinazione della fase attiva rimane tuttora ancora incerta, in quanto, se ad alta temperatura la presenza di PdO risulta determinante, a bassa temperatura la reazione sembra performante in presenza di diversi stati di ossidazione del palladio come Pd<sup>0</sup>, Pd<sup>2+</sup>, Pd<sup>4+</sup> e siti PdO<sub>x</sub> sotto-coordinati.

Questi catalizzatori possono essere ottenuti tramite metodo idrotermale sottoforma di nanofibre e nanosfere; inoltre, è possibile ottenere particolari nano-ottaedri caratterizzati da una struttura a lamelle costituiti da una maggiore esposizione dei piani di tipo (110), come è possibile osservare dall'immagine SEM riportata nella Figura 8.5 del testo. La tecnica SCS condotta partendo da precursori a base di nitrati di palladio, ceria e allumina risulta efficace nel contesto di produrre catalizzatori attivi tramite una metodologia semplice e veloce. Le immagini TEM e la loro trasformata veloce di Fourier hanno dimostrato che le particelle di palladio così prodotte si presentano circondate dalla ceria in una struttura a guscio chiamata struttura core-shell capace di aumentare sia l'attività che la stabilità del sistema. La struttura core-shell è mostrata in Figura 8.6 del testo ed è qui sotto riportata.

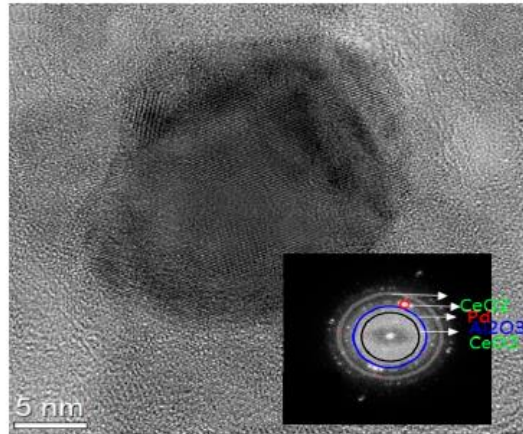


**Figura 3:** Immagine HRTEM e sua trasformata veloce di Fourier (FFT) performata su catalizzatori Pd-CeO<sub>2</sub>-Al<sub>2</sub>O<sub>3</sub> adattata da ref. [116]

L'analisi XPS mostra che i campioni preparati con questa tecnica presentano la formazione di una soluzione solida tra la ceria e il palladio, non osservata attraverso i comuni metodi di impregnazione. Questi ultimi, infatti, sono caratterizzati prevalentemente dalla presenza di palladio nella forma Pd<sup>0</sup> e PdO. La forte interazione tra il palladio e la ceria nei catalizzatori SCS accresce la produzione di vacanze di ossigeno, particolarmente attive nelle reazioni di ossidazione.

Un altro avanzato ed ingegnerizzato metodo di preparazione di questi catalizzatori è la procedura in mulino. In accordo a questa, le nanoparticelle di palladio vengono mischiate a quelle di ceria e trattate a 900°C in un mulino. Le analisi HRTEM di quest'ultime mostrano cristalliti di ossido di cerio circondati da uno strato amorfo di dimensioni tra i 2 e i 5 nm composto da una fase mista palladio-ceria. In aggiunta, in questo strato risultano presenti altre nanoparticelle di palladio con dimensione non superiore ai 5 nm.

Per quanto riguarda le performance catalitiche di questi catalizzatori, la deposizione del palladio sulle diverse morfologie della ceria può risultare in una diversa attività. In particolare, i campioni in cui il palladio viene depositato su microsferiche hanno dimostrato maggiore attività rispetto alla presenza di nanofibre. Questo è dovuto alla migliore dispersione ottenuta su questi sistemi unita all'esposizione preferenziale dei piani attivi (110). Buone prestazioni sono state anche ottenute dai particolari ottaedri caratterizzati da struttura lamellare. I catalizzatori ottenuti tramite procedura in mulino hanno dimostrato attività superiore a quelli sintetizzati con procedura SCS che a loro volta risultano più performanti di quelli in cui il palladio è inserito nella struttura utilizzato il metodo di impregnazione. Questo è sicuramente dovuto alla formazione dello strato amorfo Ce-Pd attorno ai cristalliti di ceria capace di aumentare il numero di vacanze e il disordine chimico del sistema. I campioni SCS hanno dimostrato buone attività grazie alla struttura core-shell che presenta, inoltre, elevata efficacia per la minimizzazione dei fenomeni di disattivazione.

L'ultima sezione della tesi riguarda lo studio dei principali meccanismi di reazione che contraddistinguono l'ossidazione dei principali inquinanti. La spettroscopia IR, come prima citato, gioca sicuramente un ruolo fondamentale in questo ambito. Essa, infatti, permette di identificare gli intermedi stabili formatosi durante le diverse reazioni. Il principale meccanismo che governa la catalisi ossidativa promossa tramite l'utilizzo di catalizzatori a base ceria è il meccanismo di Mars va Krevelen. Esso prevede l'interazione diretta tra l'inquinante e l'ossigeno superficiale del catalizzatore con la formazione di vacanze. L'ossigeno gassoso potrà

successivamente interagire con questi siti permettendo la formazione di nuovo ossigeno strutturale.

Il meccanismo di reazione del CO sulla praseodimia prevede l'interazione tra il CO e l'ossigeno superficiale della struttura con la formazione di carbonati bidentati. Essi sono poi trasformati in specie monodentate con la simultanea formazione di vacanze di ossigeno. I carbonati monodentati verranno successivamente decomposti in CO<sub>2</sub>. La reazione segue quindi il tipico meccanismo di Mars van Krevelen in quanto l'inquinante reagisce direttamente con l'ossigeno superficiale della struttura. L'abbattimento del CO su catalizzatori a base ceria, invece, può avvenire in accordo a tre distinti percorsi. Il primo riguarda un meccanismo di tipo water gas shift che consiste nell'interazione tra il CO e i gruppi -OH superficiali del catalizzatore con la formazione di idrogeno e CO<sub>2</sub>. Il secondo è invece basato sul classico meccanismo di Mars van Krevelen e quindi si basa sulla reazione del CO con l'ossigeno superficiale strutturale della ceria. I carbonati formati sono poi decomposti in CO<sub>2</sub>. I due meccanismi descritti precedentemente sono osservati su tutte e tre le nanostrutture. Il terzo meccanismo proposto, al contrario, è stato rilevato solamente su nanofibre tramite analisi Raman. Esso si basa sulla reazione di sproporzionamento o di Boudouard che consiste nella reazione di due molecole di CO con la formazione di anidride carbonica e specie carboniose.

D'altro canto, la combustione catalitica del particolato segue il classico meccanismo di Mars van Krevelen. In aggiunta è stato osservato un altro fenomeno legato alla formazione di specie ossigeno attive, quali perossidi e superossidi, in seguito all'interazione tra l'ossigeno gassoso e le vacanze di ossigeno presenti sulla superficie catalitica. Queste specie risultano essenziali nell'abbattimento del particolato in quanto, tramite un fenomeno di spillover, possono muoversi sulla superficie del materiale raggiungendo le particelle carboniose e promuovendone una più facile ossidazione. Un altro punto fondamentale inerente all'abbattimento del particolato è la presenza di siti acidi superficiali sui materiali catalitici. Essi, infatti, reagendo con il particolato possono portare alla creazione di intermedi radicalici cationici più facilmente ossidabili dalle specie ossigeno presenti nel sistema. L'ossidazione della matrice carboniosa risulta particolarmente interessante su catalizzatori a base ceria-praseodimia in presenza di NO<sub>2</sub>. A questo proposito, l'NO viene convertito in NO<sub>2</sub> probabilmente attraverso un meccanismo di tipo Langmuir-Hinshelwood con produzione di NO<sub>2</sub> gassoso. Esso verrà successivamente riadsorbito sulla superficie del catalizzatore sotto forma di nitrato. L'ossidazione del particolato quindi può avvenire per interazione della matrice carboniosa con l'ossigeno, le specie ossigeno attive formatesi sulla superficie catalitica, NO<sub>2</sub> gassoso e NO<sub>2</sub> adsorbito sotto forma di nitrato, come dettagliatamente descritto in Figura 9.8 della tesi. È stato notato che il ruolo del praseodimio è quello di promuovere la conversione di NO a NO<sub>2</sub> promuovendone il suo adsorbimento sulla superficie catalitica. La presenza di platino svolge lo stesso ruolo, ma in questo caso esso non incentiva il chemisorbimento di NO<sub>2</sub>. Il platino, d'altro canto, migliora la selettività della reazione nella formazione di CO<sub>2</sub>.

Per quanto riguarda i VOCs, la loro ossidazione catalitica può avvenire in accordo a tre percorsi distinti:

- Il meccanismo di Mars van Krevelen
- Il meccanismo di Langmuir-Hinshelwood
- Il meccanismo di Eley-Rideal

Dato che questa classe di composti comprende un grande numero di molecole, è difficile definire un meccanismo di reazione generale che accomuni i diversi composti. Risulta quindi opportuno uno studio sostanza per sostanza. A titolo di esempio, lo step determinante la velocità di ossidazione del metano risulta il suo adsorbimento dissociativo. Considerando il PdO come fase attiva, il ciclo catalitico inizia con l'adsorbimento dissociativo dell'ossigeno sul palladio. Successivamente il metano interagisce con l'ossigeno chemisorbito con la produzione di specie -OH e -OCH<sub>3</sub>. Il monossido e il biossido di carbonio possono essere considerati come i

principali prodotti della reazione con simultaneo ripristino del sito ossigeno attivo e la formazione di acqua chemisorbita. Il CO prodotto può reagire ulteriormente con i siti -OH dell'allumina, se presente, dando origine alla formazione di gruppi formiati sulla superficie del catalizzatore. Dopo il desorbimento veloce dell'acqua, invece, il CO può interagire con i siti di ossigeno attivo del campione con la formazione di anidride carbonica e la chiusura del ciclo catalitico.

Il meccanismo di ossidazione dell'NO su catalizzatori a base platino dispersi su ceria inizia tramite il chemisorbimento dissociativo dell'ossigeno sul catalizzatore con la formazione di specie  $OPt^{x+}O$ . Queste possono interagire con le molecole di NO con la formazione di intermedi di tipo  $OPt^{x+}O(NO)$  la cui decomposizione produrrà  $NO_2$  e ripristinerà il sito catalitico.

Con questa tesi si è potuto dimostrare l'importante ruolo dei catalizzatori a base ceria e ceria modificata nelle reazioni di ossidazione catalitica date le uniche e peculiari proprietà di questo materiale.

Se per la molecola di CO sono stati trovati e testati catalizzatori che ne permettono l'abbattimento con elevate prestazioni, oggigiorno non è ancora presente un catalizzatore capace di promuovere la reazione di ossidazione del particolato alla tipica temperatura di scarico dei motori diesel. A questo proposito, il catalizzatore più performante per l'ossidazione delle sostanze carboniose risulta la ceria-praseodimia equimolare sintetizzata tramite procedura idrotermale. L'uso dei metalli nobili, sfortunatamente, ha dimostrato di non migliorare significativamente l'attività catalitica del sistema.

Considerando che la zirconia ha provato di aumentare sia la stabilità che l'attività di questo sistema catalitico, il catalizzatore  $Zr_{0.1}(Ce_{0.5}Pr_{0.5})_{0.9}O_2$  potrebbe permettere una riduzione della temperatura di ossidazione del particolato.

Inoltre, combinando analisi Raman e IR potrebbe risultare interessante lo studio del ruolo dei siti difettivi, acidi e basici in modo da poter sviluppare un materiale costituito dall'ottimale combinazione di queste proprietà.

Considerando che il termine VOCs comprende un grande numero di composti, è difficile, in linea generale, fare considerazioni riguardo alla migliore scelta del sistema catalitico. Risulta necessario, caso per caso e quindi molecola per molecola, lo studio del migliore materiale e della migliore tecnica di sintesi al fine di ottenere le massime prestazioni possibili. A questo proposito, la ceria-SCS si è rivelata un buon materiale per la conversione del naftalene, mentre il campione  $Ce_{0.6}Cu_{0.4}$ -SCS è attivo per l'ossidazione dell'etilene. È però necessario tenere in considerazione che, sebbene il loro costo sia particolarmente elevato e variabile nel tempo, l'uso dei metalli nobili è difficilmente evitabile data la loro elevata intrinseca attività.

I sistemi Pd/CeO<sub>2</sub> hanno mostrato elevate prestazioni riguardo all'ossidazione del metano. In particolare, le moderne e avanzate tecniche si sono rivelate più performanti rispetto a quelle convenzionali. Si pensi, per esempio, alla sintesi di strutture core-shell o alla produzione in mulino. Risulta quindi fondamentale continuare a studiare queste tecniche in modo da migliorarne ulteriormente le prestazioni. Una nuova sfida potrebbe essere l'ideazione di nuove avanzate ed ingegnerizzate procedure di sintesi al fine di ottenere risultati sempre più performanti. A questo proposito, un aspetto chiave risulta la determinazione della fase attiva, in particolare a bassa temperatura, per la reazione di ossidazione del CH<sub>4</sub>. Questa potrebbe essere studiata tramite l'utilizzo dell'analisi IR in situ identificando i vari intermedi stabili di reazione alle diverse temperature o effettuando invii di molecole sonda in modo da determinare le differenti specie che caratterizzano la superficie del catalizzatore. Per concludere, dato che l'ossido di praseodimio ha dimostrato buona attività per l'ossidazione del metano con un'elevata selettività nella produzione di CO<sub>2</sub>, l'utilizzo di un supporto a base di un ossido misto costituito da cerio e praseodimio potrebbe migliorare le performance del sistema.



## Table of contents

1. Introduction	1
2. Pollutants from stationary and mobile sources	5
2.1 Mobile sources – Pollutants from Diesel engines	5
2.1.1 Formation of CO, HCs and particulate matter	5
2.1.2 Formation of nitrogen oxides	7
2.1.3 Emission limits for passenger cars	7
2.2 Stationary sources – Pollutants from industries	8
2.2.1 Formation of Volatile Organic Compounds (VOCs)	8
3. Technologies for the abatement of pollutants	9
3.1 Mobile sources – Abatement of pollutants from Diesel engines	9
3.1.1 CO, HC and particulate matter removal technologies	9
3.1.2 NO <sub>x</sub> removal technologies	11
3.2 Stationary sources – Abatement of pollutants from industries	12
3.2.1 Volatile Organic Compounds (VOCs) removal technologies	12
4. High-performance catalysts for oxidation reactions	15
4.1 Catalysts for soot oxidation	15
4.2 Catalysts for NO oxidation	15
4.3 Catalysts for Volatile Organic Compounds (VOCs) oxidation	16
5. Chemical and physical characterization of catalysts	19
5.1 Surface area determination and pore size distribution	19
5.2 Temperature-Programmed Techniques	21
5.2.1 Temperature-Programmed Reduction (TPR)	21
5.2.2 Temperature-Programmed Oxidation (TPO)	21
5.2.3 Temperature-Programmed Desorption (TPD)	21
5.2.4 Thermal Gravimetric Analysis (TGA)	22
5.3 Electron microscopic techniques	23
5.3.1 Transmission Electron Microscopy (TEM)	23
5.3.2 Scanning Electron Microscopy (SEM)	23
5.4 Spectroscopic techniques	24
5.4.1 X-Ray Diffraction (XRD)	24
5.4.2 X-Ray Photoelectron Spectroscopy (XPS)	25
5.4.3 Raman Spectroscopy	25
5.4.4 IR Spectroscopy	26

6. Ceria catalysts	35
6.1 General proprieties of ceria catalysts	35
6.1.1 Redox features and Oxygen Storage Capacity (OSC) property	35
6.1.2 Ceria catalysts at nanoscale	37
6.1.3 Ceria catalysts at nanoscale – Preparation methods	38
6.2 Characterization of ceria catalysts	40
6.3 Catalytic performance of ceria catalysts in oxidation reactions	44
7. Modified ceria catalysts	49
7.1 Nanostructured ceria-praseodymia catalysts	49
7.1.1 General properties and catalyst characterization of ceria-praseodymia catalysts	53
7.1.2 Catalytic performance of ceria-praseodymia catalysts in oxidation reactions	56
7.2 Nanostructured ceria-praseodymia-zirconia catalysts	60
7.2.1 General properties and catalyst characterization of ceria-praseodymia-zirconia catalysts	60
7.2.2 Catalytic performance of ceria-praseodymia-zirconia catalysts in oxidation reactions	64
7.3 Nanostructured copper-ceria catalysts	66
7.3.1 General properties and catalyst characterization of copper-ceria catalysts	66
7.3.2 Catalytic performance of copper-ceria catalysts in oxidation reactions	69
8. Noble metals supported on ceria catalysts	75
8.1 General properties and catalyst characterization of NM/ceria catalysts	75
8.1.1 Platinum supported on ceria catalysts	75
8.1.2 Palladium supported on ceria catalysts	77
8.2 Catalytic performance of NM/ceria catalysts in oxidation reactions	81
8.2.1 Catalytic performance of platinum supported on ceria catalysts	81
8.2.2 Catalytic performance of palladium supported on ceria catalysts	85
9. Reaction mechanisms	89
9.1 CO oxidation	89
9.1.1 Reaction mechanism of CO oxidation on praseodymium oxides	89
9.1.2 Reaction mechanism of CO oxidation on ceria catalysts	89
9.2 Soot oxidation	92
9.2.1 Reaction mechanism of soot oxidation on ceria catalysts	92
9.2.2 Soot oxidation on ceria-praseodymia catalysts in the presence of NO <sub>x</sub> molecules	94
9.3 VOCs oxidation	96

9.3.1 Toluene oxidation on ceria catalysts	96
9.3.2 CH <sub>4</sub> oxidation on palladium-based catalysts	97
9.3.3 CH <sub>4</sub> oxidation on praseodymium oxides	98
9.4 NO oxidation	99
9.4.1 NO oxidation on ceria catalysts	99
10. Final discussion and future prospects	101
11. Symbol list	103
12. References	105
13. Acknowledgments	115
14. Acknowledgments – Italian version	117



# 1. Introduction

Environmental pollution has long been a discussed issue and is now reaching alarming levels worldwide. As it comes from both mobile and stationary sources which release different quantities and compositions of emissions, over the years several sophisticated technologies have been studied to minimize the presence of pollutants in the atmosphere. The first law regarding the pollutant emissions from stationary sources dates back to 1863 with the British Alkali Act, providing for a reduction of acid gas emissions from soda ash plants. As for the mobile applications, the first limits concerning the unburned hydrocarbons and carbon monoxide emissions from passenger cars were introduced in California in 1966.

Stationary sources enclose a wide range of structures, including people's houses, small industries and large plants. Therefore, the knowledge of the various processes is crucial to find the best solution for the abatement of pollutants. In this respect, the most produced substances are carbon monoxide (CO), unburned hydrocarbons (HCs), nitrogen oxides and sulphur oxides (NO<sub>x</sub> and SO<sub>x</sub>), volatile organic compounds (VOCs) and, in some cases, soot particles.

Regarding the mobile sources, as shown in Figure 1.1, the automotive sector is one of the most important industry segments although, according to statistical data, the global sales of passenger cars have decreased to 59.5 million units in 2020 compared with a peak of 78.9 million units reported in 2018 [1].

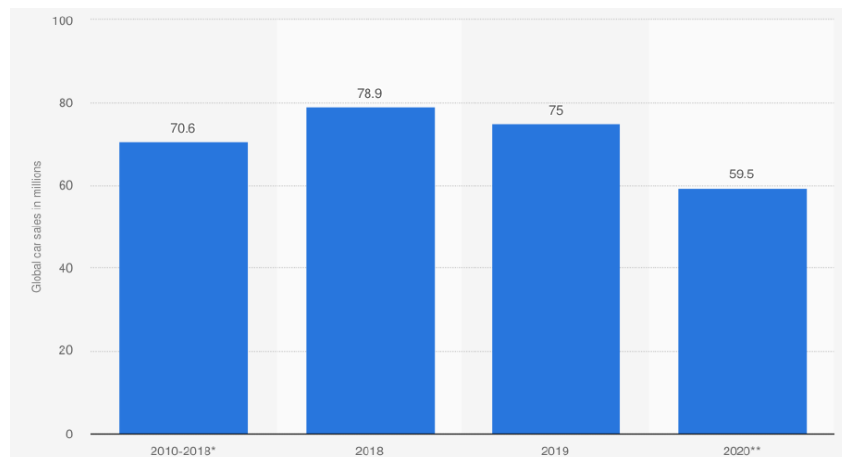


**Figure 1.1:** Number of cars sold worldwide between 2010 and 2020 (in million units) from ref. [1]

Mobile sources are primarily responsible for CO, HC and NO<sub>x</sub> emissions. In this respect, the internal combustion engines which use diesel as fuel (diesel engines or compression ignition engines) have many positive points such as high energy efficiency and low-operating costs. Furthermore, these devices show a lower concentration of CO and HC in the exhaust gases than the gasoline engines, due to the “lean” operative conditions. However, diesel engines are the main actors in nitrogen oxides and particulate matter (PM) emissions, responsible for environmental and health injuries.

Therefore, a solution has to be found to reduce the presence of these dangerous substances in the atmosphere. The catalytic oxidation certainly plays an essential role in the environmental catalysis for the pollutant emissions control from both mobile and stationary sources [2].

Generally speaking, it consists of the total oxidation reaction of pollutants in the presence of a catalyst with the formation of carbon dioxide and water, as illustrated in Equation (1.1).



The catalytic system depends on the different operative conditions and applications. Short examples can be found in the lines below.

Nitrogen oxides are responsible for acid rains and their reaction with unburned hydrocarbons contributes to the formation of toxic and reactive molecules such as peroxyacetyl nitrates or PANs. Nowadays the primary technology for NO<sub>x</sub> removal is the Selective Catalytic Reaction (SCR) which consists of the use of ammonia as a reducing agent. V<sub>2</sub>O<sub>5</sub>-WO<sub>3</sub>/TiO<sub>2</sub> is the most common catalytic system used in the stationary applications. Moreover, there are studies about different systems such as the Fe<sub>2</sub>O<sub>3</sub>-WO<sub>3</sub>/Ce<sub>x</sub>Zr<sub>1-x</sub>O<sub>2</sub> monolith catalyst and, in this regard, the Ce/Zr ratio equal to 0.68/0.32 has proved the best performance [3]. In contrast to stationary applications, zeolites are used in the automotive sector for their excellent activity under a wide range of temperature.

Carbon monoxide is a toxic substance resulting from partial combustion of fuels. CO, in contact with the bloodstream, irreversibly binds to haemoglobin; therefore, a sufficient oxygen quantity cannot reach the brain, causing serious health damages. Noble metal supported on transition metal oxides or perovskites are efficient catalysts for the CO removal. According to other studies, the dispersion of gold nanoparticles on porous supports promotes both the stability and the catalytic activity of the CO oxidation reaction [4]. However, the stability of these samples decreases by increasing the temperature.

Several techniques for the volatile organic compounds (VOCs) abatement are known, such as the use of liquid or solid adsorbents, precipitation methods and condensation technologies. Among all these, catalytic oxidation is the most efficient system to obtain the total oxidation of the volatile organic compounds. Noble metals supported on a porous material are the most widely used catalysts, but especially in recent years, metal oxide catalysts have been studied and tested to obtain a catalytic system with the equivalent performance at a lower cost [5].

Finally, remarkable progress has been achieved in the environmental catalyst field. Many catalysts have been tested and characterized by more and more sophisticated characterization techniques. In this respect, several preparation techniques of catalytic systems are studied in order to find the optimal configuration for any application. Furthermore, the selection of the correct catalyst is the fundamental step to improve the oxidation process in terms of stability, activity and selectivity, avoiding the formation of dangerous by-products or substances coming from incomplete combustion.

The main aim of this thesis is the study of different catalytic systems to find the best catalyst for the catalytic oxidation of pollutants coming from both stationary and mobile sources. The work has been divided into different sections in order to guarantee a better comprehension and fluidity of the treated topics. In the first part, the main features of the emitted pollutants are described, in particular, their formation and dangerousness for the environment and human health. Afterwards, a discussion on the most important technological solutions for the removal of these substances is presented with a specific focus on the different high-performance catalysts in use. Then, there is a section concerning the characterization of the catalytic materials which aims at a good understanding of the features of the samples treated in the following chapter of this work. The characterization section deals with the different techniques used in a typical research laboratory. Starting from the determination of the surface area, the temperature-programmed reduction, the oxidation and the desorption are investigated.

The electron microscopy technologies and the different spectroscopic techniques are also analysed with an in-depth analysis of the IR spectroscopy. This section is followed by a study on the ceria-based catalysts with particular attention on their properties and catalytic performance. Given that the latter can be further improved with the addition of foreign metallic dopants in the CeO<sub>2</sub> lattice structure, a section devoted to modified ceria catalysts is present in this work. It includes ceria-praseodymia, ceria-praseodymia-zirconia and copper-ceria oxides. As a matter of fact, ceria and modified ceria materials play an essential role in the environmental catalytic field, especially in the oxidation processes. Another chapter talks about the catalytic activity and the performance of noble metals dispersed on ceria-based supports. Lastly, in the final section, the different reaction mechanisms are investigated focusing on the stable intermediate species formed during the catalytic process.



## 2. Pollutants from stationary and mobile sources

### 2.1 Mobile sources – Pollutants from Diesel engines

#### 2.1.1 Formation of CO, HCs and particulate matter

The typical working principle of Diesel engines involves fuel injection in the cylinder at high pressure. Nowadays, there is a sophisticated system that splits the quantity of fuel into different injections to improve the combustion process. The presence of rich areas in the combustion chamber is the leading cause of the formation of carbon monoxide (CO) and unburned hydrocarbons (HCs), due to the not optimal mixing between fuel and combusive agent.

Moreover, these conditions allow the creation of polycyclic structures, called “platelets”, which are the building blocks of soot particles [6]. As shown in Figure 2.1, these compounds are formed from the closure in ring structures of polyethyne molecules resulting from the polymerization of small unsaturated species with ethyne as the primary component. The platelet combination allows the formation of spherical particles which increase in size due to the coagulation and the surface growth phenomena. The union of these primary soot particles leads to the creation of aggregates with dimensions between 0.1 and 10  $\mu\text{m}$ .

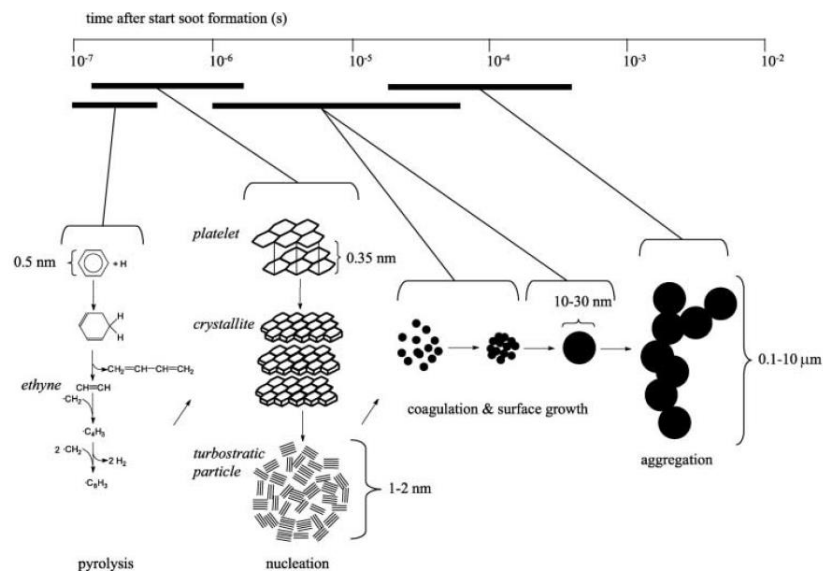
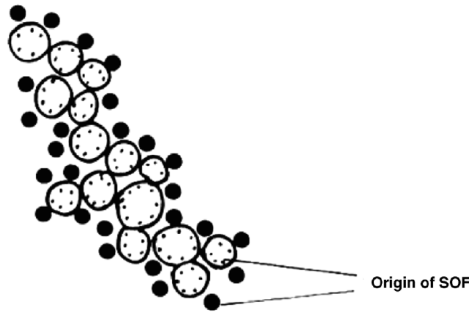


Figure 2.1: Mechanism of soot particles formation from ref. [6]

The particulate matter (PM) is characterized by a complex structure and its composition is strongly temperature dependant. As a general rule, it consists predominantly of carbonaceous agglomerates (41%) which collect on their surface other different substances such as unburned fuel (7%), unburned lubricating oil (25%), water (14%) and inorganic compounds characterized by ash and sulphur species (13%) [7]. As illustrated in Figure 2.2, the fractions of unburned fuel and lubricating oil are generally enclosed in the term soluble organic fraction (SOF) and it can vary greatly depending on the engine design, the operative conditions and the fuel composition.



**Figure 2.2:** Representation of diesel particulate matter adapted from ref. [8]

Classification and dangerousness of particulate matter

The classification of particulate matter is carried out according to the size of the particles because these imply environmental and health problems with a different entity. Therefore, soot particles can be classified in four different categories: large particles ( $>10 \mu\text{m}$ ), coarse particles PM-10 (from  $2.5$  to  $10 \mu\text{m}$ ), fine particles PM-2.5 (from  $1.0$  to  $2.5 \mu\text{m}$ ) and ultra-fine particles PM-1 ( $<1 \mu\text{m}$ )[7]. Furthermore, the size of these aggregates establishes their residence time in the atmosphere; the larger particles show a shorter sedimentation time than the smaller ones, consequently these last can be carried by the wind for long distances.

Regarding the effect of particulate matter on human health, the human body has no protective system or barriers against particles smaller than  $10 \mu\text{m}$  and, as shown in Figure 2.3, aggregate systems with these dimensions are typical of diesel engines [7]. Therefore, during breathing, these particles can reach the lungs and eventually enter the bloodstream causing irritations, headache, bronchitis, chronic respiratory, cardiovascular and cardiopulmonary diseases. Regarding instead the impact of particulate matter on the environment, it contributes to the pollution of air, water and soil, and soot deposition negatively affects agricultural productivity and the preservation of materials over time.

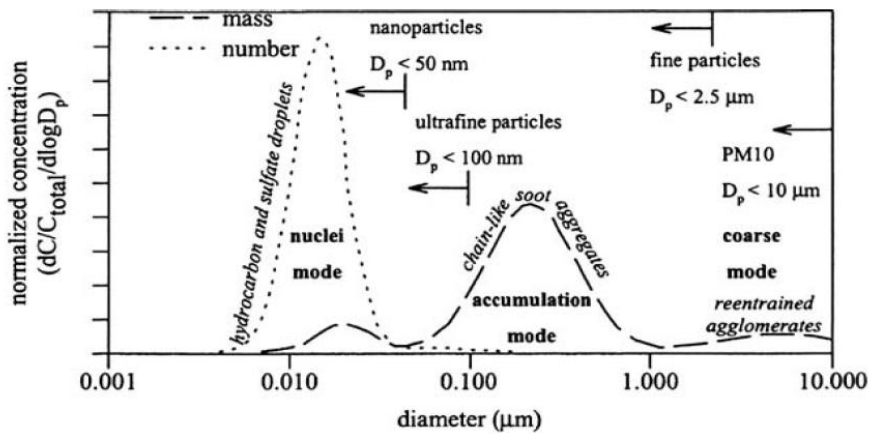


**Figure 2.3:** Typical particle size distribution from diesel engines from ref. [7]

### 2.1.2 Formation of nitrogen oxides

Nitrogen oxides are mainly formed during combustion processes and typically made up by 95% of NO and 5% of NO<sub>2</sub>. The NO<sub>x</sub> formation depends on various factors such as temperature, residence time and oxygen and nitrogen concentrations and, as a general rule, it is based on three mechanisms [9]:

- Thermal nitrogen oxides derive from the direct combination of N<sub>2</sub> and O<sub>2</sub> at a temperature greater than 1500 K following the Zeldovich's radical according to Equation (2.1) and (2.2)



Lowering the combustion temperature and the residence time in these conditions allows the reduction of NO<sub>x</sub> molecules

- Prompt nitrogen oxides come from the reaction between hydrocarbon radicals, resulting from not-perfect combustion, and nitrogen as described in Equation (2.3)



The HCN compound, due to an oxidation process in the presence of oxygen, allows the formation of carbon dioxide, NO<sub>x</sub> and water. The only way to the prompt NO<sub>x</sub> removal is to ensure a mixing as homogeneous as possible between combustible and oxidizing to avoid the formation of hydrocarbon radicals

- Nitrogen oxides from fuel are formed as the result of the oxidation of nitrogen present in organic molecules of the fuel

### 2.1.3 Emission limits for passenger cars

The EU emission standards for passenger cars are summarized in Figure 2.4. The formation of pollutants depends on the type of engine. Positive ignition and compression ignition vehicles differ in term of operative conditions and therefore different emission limits are provided by the EU regulations. The emissions are tested following the Worldwide harmonized Light vehicles Test Cycle (WLTC) which replaced the previous NEDC procedure [10]. To minimize the difference in emissions between the results obtained with the test bench and the real systems, the Real Driving Emissions (RDE) test procedure has been gradually introduced since 2017. This latter consists in a road test from 60 to 120 minutes along three difference segments: urban (< 60 km/h), rural (60-90 km/h) and motorway (> 90 km/h).

To compensate the discrepancy between laboratory and road emissions, two conformity factors [10], one for nitrogen oxides and the other for the particulate number, are adopted. Currently, the conformity factor for PN is 1.5 for all the vehicles, whereas for NO<sub>x</sub> the CF value is 1.43 for the new models and it must be respected for all vehicles starting from 2021. Therefore, a passenger car can emit CF times more than the result obtained in laboratory conditions.

As to compression ignition vehicles (Diesel engines), the value of the carbon monoxide has been stable at 500 mg/km since 2005. Furthermore, there are two emission limits concerning the nitrogen oxides and nitrogen oxides plus unburned hydrocarbons. In this regard, it is important to note that the NO<sub>x</sub> value has been reduced by about an order of magnitude from 2000 until today. The limits for particulate emissions are considered in two values: PM and PN which represent the mass and the number of particles, respectively. PM is not a satisfactory

parameter to quantify the emission of these aggregates; PN, on the other hand, is a fundamental factor to take into account the presence of a large number of tiny particles having a little contribution in the total mass.

Stage	Date	CO	HC	HC+NOx	NOx	PM	PN
		g/km					#/km
<b>Positive Ignition (Gasoline)</b>							
Euro 1†	1992.07	2.72 (3.16)	-	0.97 (1.13)	-	-	-
Euro 2	1996.01	2.2	-	0.5	-	-	-
Euro 3	2000.01	2.30	0.20	-	0.15	-	-
Euro 4	2005.01	1.0	0.10	-	0.08	-	-
Euro 5	2009.09 <sup>b</sup>	1.0	0.10 <sup>d</sup>	-	0.06	0.005 <sup>e,f</sup>	-
Euro 6	2014.09	1.0	0.10 <sup>d</sup>	-	0.06	0.005 <sup>e,f</sup>	6.0×10 <sup>11</sup> e,g
<b>Compression Ignition (Diesel)</b>							
Euro 1†	1992.07	2.72 (3.16)	-	0.97 (1.13)	-	0.14 (0.18)	-
Euro 2, IDI	1996.01	1.0	-	0.7	-	0.08	-
Euro 2, DI	1996.01 <sup>a</sup>	1.0	-	0.9	-	0.10	-
Euro 3	2000.01	0.64	-	0.56	0.50	0.05	-
Euro 4	2005.01	0.50	-	0.30	0.25	0.025	-
Euro 5a	2009.09 <sup>b</sup>	0.50	-	0.23	0.18	0.005 <sup>f</sup>	-
Euro 5b	2011.09 <sup>c</sup>	0.50	-	0.23	0.18	0.005 <sup>f</sup>	6.0×10 <sup>11</sup>
Euro 6	2014.09	0.50	-	0.17	0.08	0.005 <sup>f</sup>	6.0×10 <sup>11</sup>

\* At the Euro 1..4 stages, passenger vehicles > 2,500 kg were type approved as Category N<sub>1</sub> vehicles  
† Values in brackets are conformity of production (COP) limits  
a. until 1999.09.30 (after that date DI engines must meet the IDI limits)  
b. 2011.01 for all models  
c. 2013.01 for all models  
d. and NMHC = 0.068 g/km  
e. applicable only to vehicles using DI engines  
f. 0.0045 g/km using the PMP measurement procedure  
g. 6.0×10<sup>12</sup> 1/km within first three years from Euro 6 effective dates

**Figure 2.4:** EU emission standards for passenger cars from ref. [10]

## 2.2 Stationary sources – Pollutants from industries

### 2.2.1 Formation of Volatile Organic Compounds (VOCs)

The term “volatile organic compounds” (VOCs) encloses a large number of compounds which contribute to air pollution. They come from several industrial processes such as chemical plants, petroleum refineries, pharmaceutical companies, food processes, automobile or aeroplane manufactures and many more. The definition of this group of chemical species differs from country to country. In this regard, the European Union defines the volatile organic compounds as “any organic compound having at 293.15 K a vapour pressure of 0.01 kPa or more, or having a corresponding volatility under the particular conditions of use. For the purpose of this Directive, the fraction of creosote which exceeds this value of vapour pressure at 293.15 K shall be considered as a VOC” [11].

The nature and the type of VOCs are highly dependent on the industrial process from which they come. They consist of several chemical families such as alkanes, olefins, ketones and aldehydes, as well as sulphur and halogenated compounds [12]. Considering the great variety of VOCs, they can cause several negative consequences for human health. Some of them cause eye and nose irritation or liver and central nervous system damages, others, instead are toxic or carcinogenic. Furthermore, VOCs are responsible for serious environmental problems. The gaseous compounds, which are not oxidized into the atmosphere, can intensify the greenhouse effect and, especially halogenated hydrocarbons, can cause the stratospheric ozone depletion [13].

### 3. Technologies for the abatement of pollutants

#### 3.1 Mobile sources – Abatement of pollutants from Diesel engines

##### 3.1.1 CO, HC and particulate matter removal technologies

The exhaust composition of a typical diesel vehicle is called “lean” as the engine operates under excess air conditions, thus the exhaust gas composition consists of a greater amount of oxidizing agents than the reducing ones. For this reason, it is unthinkable to use a three-way catalyst, as for the gasoline engines, because it requires the operation of the engine under stoichiometric conditions.

The first contribution to the reduction of pollutants consists of a non-filter-based honeycomb monolithic system called Diesel Oxidation Catalysts (DOCs). The walls of this latter are impregnated with a porous washcoat containing noble metals active sites. The DOC system is essential for the oxidation of carbon monoxide, unburned hydrocarbon and eventually, the VOCs formed during the combustion process. Moreover, this system contributes to the reduction of the SOF fraction of the particulate matter [14].

To respect the stricter and stricter limits on the particulate matter, the Diesel Particulate Filter (DPF) has been introduced starting from the Euro 4 legislation. The DPF is placed after the DOC system and consists of a wall-flow monolithic structure, as shown in Figure 3.1. The silicon carbide (SiC) is the typical material used for these filters, indeed, due to its high melting point and its high thermal conductivity, it can guarantee a quick and efficient heat dispersion combined with a good mechanical stability.

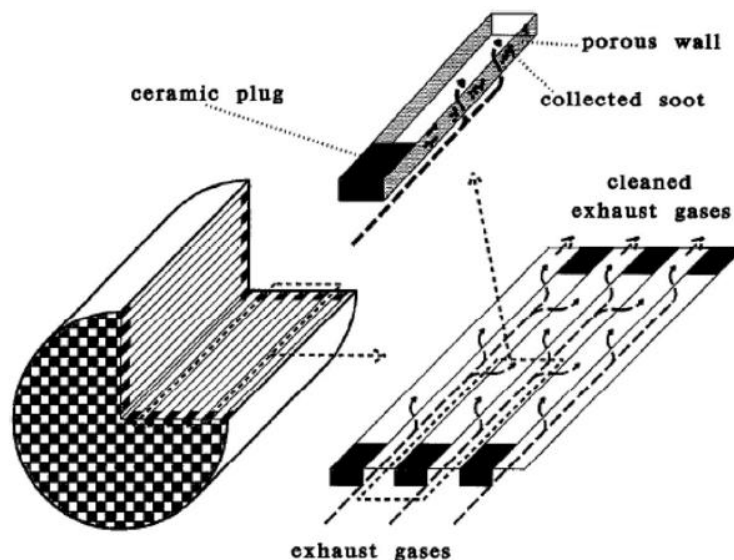


Figure 3.1: Schematic representation of a wall-flow monolith from ref. [15]

Diesel particulate spontaneously burns, in presence of air, at 600-620°C. Given that this value range is not reached by diesel exhaust gases in the DPF, catalysts can play an important role in leading to a low-temperature soot oxidation reaction. In this regard two methods have been studied. The first one is the system promoted by the PSA group: it consists in the use of Ce-fuel additives to favour the formation of CeO<sub>2</sub> particles in the combustion chamber, above which the particulate matter can grow obtaining an efficient contact between the catalysts and

the soot [14]. However, the soot oxidation temperature is reduced by only 100°C, therefore, a periodically regenerating system is necessary. The second approach, instead, consists in the use of a coated DPF, although the main challenge today is to develop a catalytic system able to decrease the soot oxidation temperature from 600°C to 300-400°C, in order to obtain an oxidation temperature compatible with the typical temperature of the diesel exhaust gas.

In these cases, the particulate matter settles on the filter promoting a cake-filtration mechanism. The thickness of the deposited soot increases and, when the engine control unit registers a prearranged value of pressure drops of the gaseous flow through the DPF, a regeneration process is necessary. The post-injection system is the most efficient method among those studied over the years. Post-injection of fuel into the cylinder allows its vaporization, but not its oxidation, therefore a fraction of unburned fuel reaches the DOC system. In this apparatus, the fuel is catalytically oxidized following an exothermic reaction to reach the correct soot oxidation temperature in the DPF [16]. This fact emphasizes the importance of the study of a catalyst capable of decreasing the oxidation soot temperature to 300-400°C to avoid the fuel penalties of the system.

The Continuously Regenerating Trap (CRT) system by Johnson Matthey company is another patented and tested technology [14]. NO<sub>2</sub> is used as an oxidizing agent in the soot combustion reaction obtaining, as shown in Figure 3.2, higher performance than in the presence of oxygen. Knowing that the most of the formed NO<sub>x</sub> are constituted by NO due to the engine operative conditions, it is possible to use a higher quantity of noble metals in the DOC system than in the previous situations to promote the oxidation of NO to NO<sub>2</sub>. This latter reacts with the deposited soot on the DPF with the formation of NO and CO<sub>2</sub> according to Equation (3.1).



Therefore, in this case, the trap can continuously be regenerated [7]. Another way to improve the system efficiency is the utilization of a catalyst on the DPF capable of transforming the NO coming from the previous reaction into NO<sub>2</sub>, to always have the active substance available for the soot oxidation.

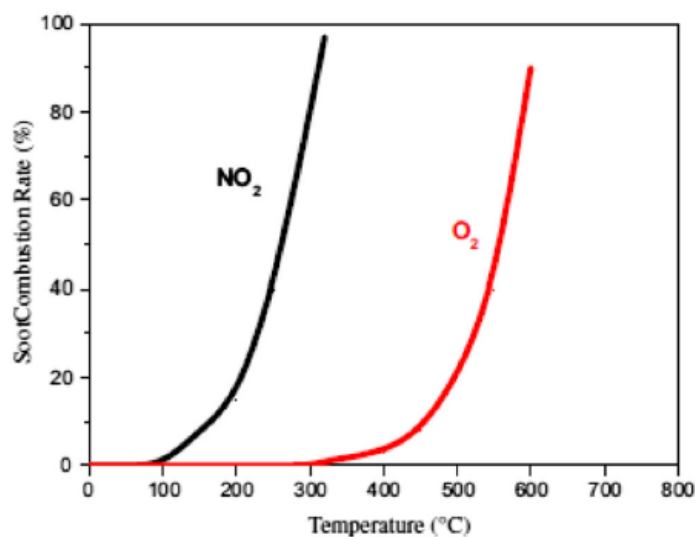


**Figure 3.2:** Soot combustion rate as a function of temperature in the presence of O<sub>2</sub> and NO<sub>2</sub> from ref. [15]

### 3.1.2 NO<sub>x</sub> removal technologies

As for the NO<sub>x</sub> reduction to molecular nitrogen, the exhaust gas recirculation (EGR) has been the most used system for many years. It is based on the recycling of an outgoing gas fraction in the combustion chamber to reduce the combustion temperature and, therefore, to avoid the formation of thermal NO<sub>x</sub>. However, this system involves an increase in the number of soot particles due to the not-optimal engine working conditions. Nowadays, although the influence of the NO<sub>x</sub>-PM trade-off has been experimentally studied to reduce the nitrogen oxides without increasing the particulate matter [17], this method is no longer sufficient due to the stricter limits on the NO<sub>x</sub> emissions.

Other different technologies have been studied. A solution is the selective catalytic reduction (SCR) technology. According to this latter system, there are three reaction mechanisms by which the mixture NO/NO<sub>2</sub> can be transformed into N<sub>2</sub> depending on the NO<sub>2</sub>/NO ratio and the presence of oxygen [15]. In the automotive sector, it is possible to take advantages of the fast-SCR reaction, which is based on a NO/NO<sub>2</sub> equimolar ratio, by converting a part of NO produced in the engine to NO<sub>2</sub> in the DOC system, due to the presence of noble metals. The SCR technology consists of a urea injection after the DOC reactor, followed by in situ generation of ammonia, which is the reducing agent for the reaction, as shown in Figure 3.3. Doped zeolites with copper or iron, in particular chabasites, are the most used catalysts for the SCR application. Finally, an oxidation system for the possible ammonia residue is used to avoid its environmental dispersion.

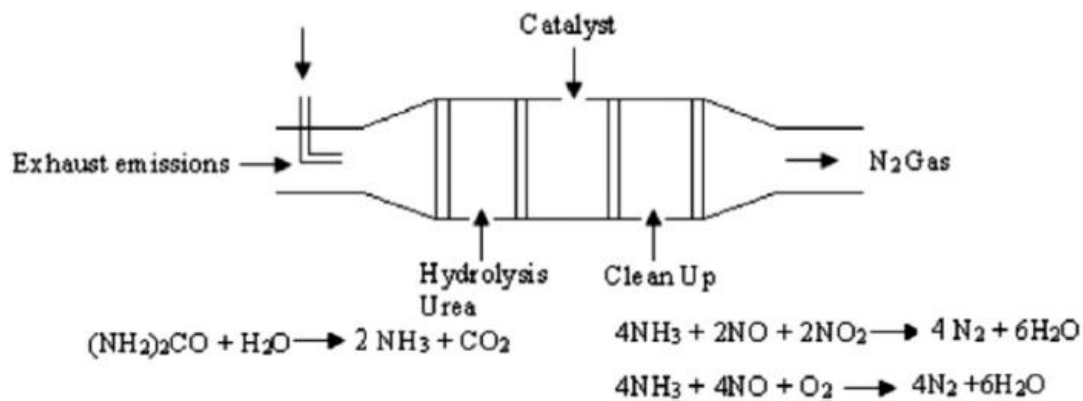


**Figure 3.3:** SCR system in mobile applications from ref. [15]

Considering that a catalyst capable to perform the soot oxidation at low temperature has not been found yet, the SCR technology can be used directly on the diesel particulate filter by depositing on this latter the catalyst for the NO<sub>x</sub> reduction. As a urea injection is released before the DPF, it is possible to combine the soot filtration function and the NO<sub>x</sub> reduction in a single unit called SCRoF (SCR on Filter) [18].

Lean NO<sub>x</sub> Trap (LNT) is another technology for nitrogen oxides reduction [19]. As described in Figure 3.4, the LNT catalysts are typically made of a noble metal, a storage element and a high surface area support material. The NO coming from the engine is oxidized to NO<sub>2</sub> due to the presence of the noble metal. The catalyst can store and trap these species in a nitrate form under lean operation conditions and, due to the post-injection apparatus, it is possible to periodically perform the regeneration process. In this respect, a fraction of unburned fuel reaches the DOC system and is oxidized, increasing the temperature and causing the

decomposition of the barium nitrates to BaO and NO<sub>x</sub>. These last are reduced to N<sub>2</sub> in the presence of noble metals and reducing agents such as hydrogen, HC and CO.

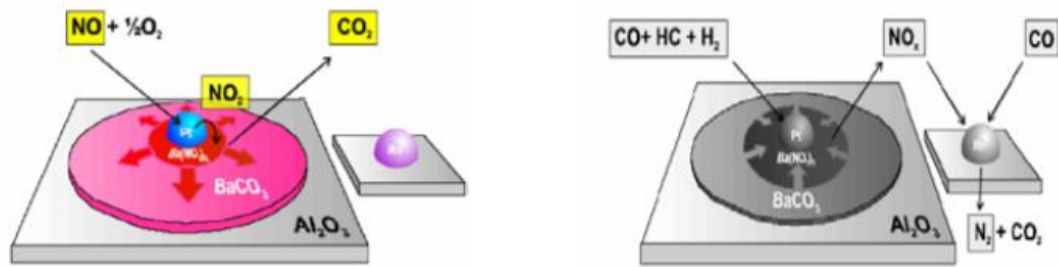
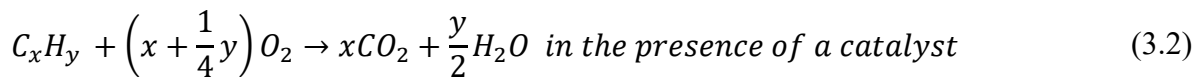


**Figure 3.4:** LNT system under lean and regeneration conditions from ref. [19]

## 3.2 Stationary sources – Abatement of pollutants from industries

### 3.2.1 Volatile Organic Compounds (VOCs) removal technologies

As explained above, the catalytic oxidation is one of the most advanced systems for the volatile organic compounds removal. In general, it is performed according to Equation (3.2) [13].



The main products of the reaction are CO<sub>2</sub> and water. However, as explained in Equation (3.3), in the presence of halogenated hydrocarbons the formation of other species also occurs. For instance, in case of chlorinated compounds, water vapour should be added to the gas stream to improve the selectivity of hydrochloric acid and to avoid formation of gaseous chlorine [5].



In this context, several structures are studied to find the best combination of low-pressure drops, high conversions of pollutants and good thermal and attrition resistance. The most widespread and economically significant system to obtain these three features is the use of honeycomb monoliths. In these structures, a catalytic layer is deposited onto the channel walls to perform the catalytic oxidation of VOCs. It is possible to use metallic or ceramic monoliths. The first ones are characterised by a high thermal conductivity which allows the quick achievement of the working temperature of the catalytic system. However, they are more expensive compared to ceramic monoliths. These last generally consist of cordierite and have good stability at high temperature due to the low thermal expansion coefficient [13].

Figure 3.5 shows the most used technological systems for the VOCs abatement. The catalytic oxidation of hydrocarbons is carried out at 250-400°C, while for the halogenated compound, a temperature higher than 400°C is required. Thus, a burner is necessary to preheat and to adjust the gas flow rate temperature reaching an adequately high catalytic activity [5]. As a general rule, the following configurations are possible:

- a: the polluted air is heated and sent to the catalytic converter
- b: the polluted air is preheated by the gas leaving the system and sent to the catalytic converter. A burner is required if the temperature of the treated gases is lower than that required for the good activity of the catalyst
- c: this configuration is like the previous one, with the addition of further heat recoveries of the outgoing gases

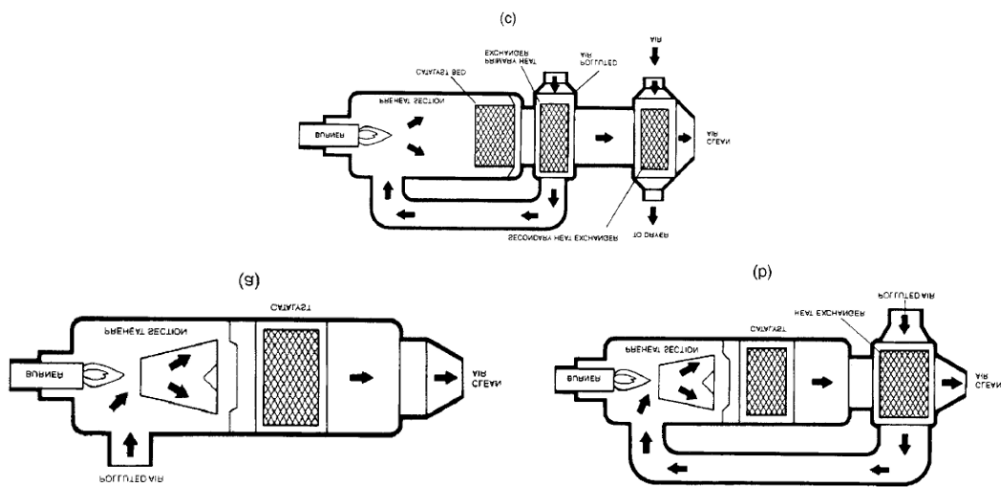


**Figure 3.5:** Technological systems for VOCs abatement form ref. [5]



## 4. High-performance catalysts for oxidation reactions

### 4.1 Catalysts for soot oxidation

The soot oxidation is a complex and peculiar reaction due to the presence of two solid phases, the catalyst and the particulate matter, and a gaseous phase. Furthermore, as seen before, soot is a heterogeneous material whose composition changes depending on the fuel and the lubricant oil used, the age of the engine and the operative conditions. Another critical point of this reaction concerns the soot-catalyst contact, which is typically defined as “loose” in a coated particulate filter. This weak interaction is obtained in the laboratory by gently shaking the catalyst-soot mixture. On the contrary, the intimate mixture between soot and catalyst called “tight contact” is obtained in a ball milling. Although the latter method does not show the real features present in a DPF, it is fundamental for the study of the intrinsic catalytic activity of a catalyst, not considering other limiting reaction phenomena. Figure 4.1 shows the performance of different catalysts tested for the soot oxidation reaction under the same experimental conditions in a typical diesel exhaust gas composition.

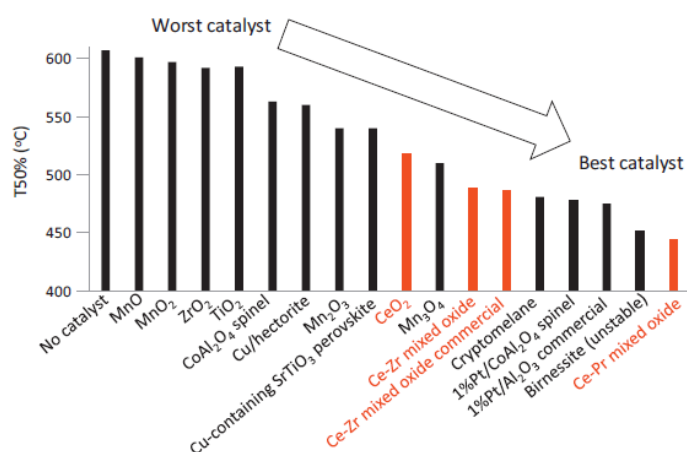


**Figure 4.1:** T<sub>50%</sub> of different catalysts tested for the soot combustion reaction [20]

As a general rule, pure oxides as ZrO<sub>2</sub>, TiO<sub>2</sub>, MnO, MnO<sub>2</sub> show minimal catalytic activity in contrast to noble metals, such as platinum supported on porous materials. The most active manganese-based catalyst for soot oxidation is the birnessite sample, but unfortunately, it is not stable at high temperature. Nevertheless, it is a mixed oxide which combines Mn (IV) and Mn (III) cations with alkali cations in a laminar structure of [MnO<sub>6</sub>] octahedra [20]. The most active catalyst for soot oxidation is a Ce-Pr mixture oxide due to the unique redox properties of the ceria sample combined with the beneficial role of praseodymium.

### 4.2 Catalysts for NO oxidation

Several catalytic systems have been studied for the catalytic oxidation of NO to NO<sub>2</sub>, which is a key step for NO<sub>x</sub> and soot elimination. Platinum is the primary choice due to the higher activity of noble metals than the other samples. The Pt dispersion, its loading and the type of support play an essential role in the reaction performance. Furthermore, the NO oxidation is a size-dependent reaction, indeed, the reaction rate decreases with the reduction of the particles size due to the formation of Pt-oxides, which are less active than metallic platinum. Different

supports have been tested reaching a maximum activity with the TiO<sub>2</sub>, SiO<sub>2</sub> and Al<sub>2</sub>O<sub>3</sub> samples due to the obtainment of a high platinum dispersion. The activity of the NO oxidation more strongly depends on the deposition method of the active species and the different pre-treatment of the catalyst. In this respect, Pt/TiO<sub>2</sub> pre-treated in O<sub>2</sub>/He shows higher NO activity than in the presence of an H<sub>2</sub>/He mixture, whereas catalysts prepared by wet impregnation shows different performance than samples obtained through photo dispersion. Different metal oxides catalysts have also been tested due to their low cost and high stability: good performance has been obtained using Mn-Ce-O<sub>x</sub> samples and some perovskites such as LaCoO<sub>3</sub> and LaMnO<sub>3</sub> [21].

### 4.3 Catalysts for Volatile Organic Compounds (VOCs) oxidation

The gaseous streams coming from the different processes generally contains a multicomponent mixture of volatile organic compounds. As it is impossible to test gaseous mixtures with so many components in the laboratory, the choice of a catalytic system can be complex. In this respect, the catalytic tests are typically performed on the compound present in larger quantity and/or on the most difficult compound to oxidize [5]. Consequently, the mixture effects produce a gap between the experimental results and the real conditions; in fact, the catalytic oxidation for individual components can be inhibited, enhanced or remain unchanged in a mixture. In this scenario, the destructibility of VOCs changes according to the chemical class of the compounds, as described in Table 4.1 [22].

**Table 4.1:** Relative Destructibility of VOCs adapted from ref. [22]

Compound Class	Relative Destructibility
Alcohols	High ↓ Low
Cellosolves/dioxane	
Aldehydes	
Ketones	
Acetates	
Alkanes	
Chlorinated hydrocarbons	

The destruction efficiency increases with the presence of insaturations for hydrocarbons characterized by the same number of carbon atoms. Chlorinated compounds are the most difficult VOCs to oxidize: their low destruction efficiency is due to the formation of by-products during the catalytic oxidation and the interaction between these species and the catalyst surface can cause deactivation problems [5].

The catalysts used for catalytic oxidation of VOCs can be classified into two categories [12]:

- Noble metals catalysts
- Metal oxide catalysts

Precious metals, especially rhodium, platinum and palladium, are typically dispersed on a suitable support such as Al<sub>2</sub>O<sub>3</sub>, ZrO<sub>2</sub>, CeO<sub>2</sub>, TiO<sub>2</sub> and others. Noble metals are widely used due to their high activity even at low temperature. The catalytic performance of these systems depends on several factors, including the particle size, the metal loading, the nature of support,

the presence of water and the mixture effects. Interestingly, each metal shows a different activity in any oxidation reactions. For example, rhodium supported on alumina is the most active catalyst in hexene oxidation, but its activity decreases in the presence of aromatics compounds. Platinum on alumina is very active in benzene oxidation, whereas Pd/Al<sub>2</sub>O<sub>3</sub> is active in toluene and methane removal [23]. However, the performance of noble metals can be compromised in the presence of chlorinated compounds. These last have two negative effects on the catalytic oxidation of VOCs. First of all, halogenated compounds are adsorbed on the sites that are normally used for the adsorption and the activation of oxygen, causing a deficit of active oxygen species on the catalytic surface. Secondly, the interaction between noble metals and chlorine allows the formation of platinum or palladium oxide-chloride species, making the catalytic oxidation sites less active in the VOCs removal reaction [24], [25].

Metal oxide catalysts are studied to find a compromise between their good resistance to poisons and the high cost of noble metals. These catalysts are readily available with a low cost and are generally used in the catalytic oxidation of VOCs, although they are less active than platinum, palladium and rhodium [12]. The most studied systems based on metal oxides are the following:

- Vanadium-based catalysts are not selective in the VOCs oxidation because of the high production of CO; however, the catalytic system of the SCR reaction constituted by V<sub>2</sub>O<sub>5</sub>/WO<sub>3</sub>/TiO<sub>2</sub> appears highly active in the oxidation of chlorine compounds [26]. It is possible to use a single catalytic system for both VOCs and NO<sub>x</sub> abatement
- Manganese-based catalysts are highly efficient in the catalytic oxidation of CO and VOCs: they are tested for the abatement of several compounds, such as n-hexane, acetone, benzene, toluene and propane [12]. In particular, the oxidation of benzene and toluene has been performed over different manganese oxides obtaining the following catalytic activity: Mn<sub>3</sub>O<sub>4</sub> > Mn<sub>2</sub>O<sub>3</sub> > MnO<sub>2</sub>, due to the different oxygen mobility on the catalysts. The addition of K, Ca and Mg can improve the catalytic activity of the samples [27]. Manganese-based catalysts are sensitive to chlorine poisoning
- CeO<sub>2</sub> and CeO<sub>2</sub>-based catalysts are cheaper and show good abatement efficiency for non-chlorinated VOCs, such as methanol and propane. They are also tested for the catalytic oxidation of VOCs, which contain chlorine in their structure. In this context, the main reaction products are HCl, Cl<sub>2</sub>, CO<sub>2</sub> and traces of CO [28]. Ceria catalysts are highly active in the oxidation of trichloroethylene due to their surface basicity and oxygen-supplying ability. However, the catalytic activity drastically drops due to the strong adsorption of the reaction products on the ceria active sites, followed by the sample deactivation [29]

Furthermore, systems based on cobalt, nickel and chromium oxides have shown good performance in the catalytic oxidation of volatile organic compounds [12].



## 5. Chemical and physical characterization of catalysts

As described above, with the development of chemical processes, the catalytic materials have begun to play an increasingly important role in chemical reactions. The catalytic field is in continuous evolution thanks to the research of new preparation methods, new samples and new reaction mechanisms. The major difference between the past and the present years is the development of technologically advanced characterization techniques, necessary for a complete knowledge of these materials. The main characterization techniques will be described in the paragraphs below.

### 5.1 Surface area determination and pore size distribution

Catalytic reactions mainly concern the surface of a solid. Most of heterogeneous catalysts are porous material with a medium-high surface area that increases the number of available active sites. The pore size and volume depend on the preparation method of the sample. According to the pore dimensions, it is possible to classify catalysts as:

- Microporous materials with a diameter less than 2 nm
- Mesoporous materials with a diameter between 2 and 50 nm
- Macroporous materials with a diameter greater than 50 nm

The morphology is a key point to understand the behaviour of a catalyst in a chemical reaction. The reactive molecules must indeed diffuse from the bulk phase to the catalytic interface and, from here on, towards the internal porosity to reach the active sites. An essential point is, therefore, the pore size optimization considering that small pores guarantee high surface area values, but internal diffusional limitation can occur [30]. The main morphological features of a catalyst are the specific surface area and the pore size distribution. The physical adsorption of nitrogen gas at the liquid nitrogen temperature (77 K) is the most used technique for the surface area evaluation. This method allows the measurement of pores with size between 0.4 and 50 nm, therefore, it is helpful for the characterization of both microporous and mesoporous materials. This phenomenon is related to the presence of van der Waals forces between the gas phase and the catalyst surface. Knowing the amount of adsorbed gas on the adsorbent material in a monolayer coverage, it is possible to evaluate the surface area according to Equation (5.1).

$$S_{BET} = n_m A_m N_A \quad (5.1)$$

- $S_{BET}$ : specific surface area ( $\text{m}^2 \text{g}^{-1}$ )
- $n_m$ : monolayer capacity ( $\text{moles g}^{-1}$ )
- $A_m$ : area occupied by a molecule ( $\text{m}^2 \text{molecule}^{-1}$ )
- $N_A$ : Avogadro number ( $\text{molecule mole}^{-1}$ )

The result of this analysis is a graph in which the amount of the adsorbed gas is plotted as a function of the relative pressure (absolute/saturation pressure). Also, according to the IUPAC classification [31] established in 1985, it is possible to subdivide the physisorption isotherms in six types, as shown in Figure 5.1.

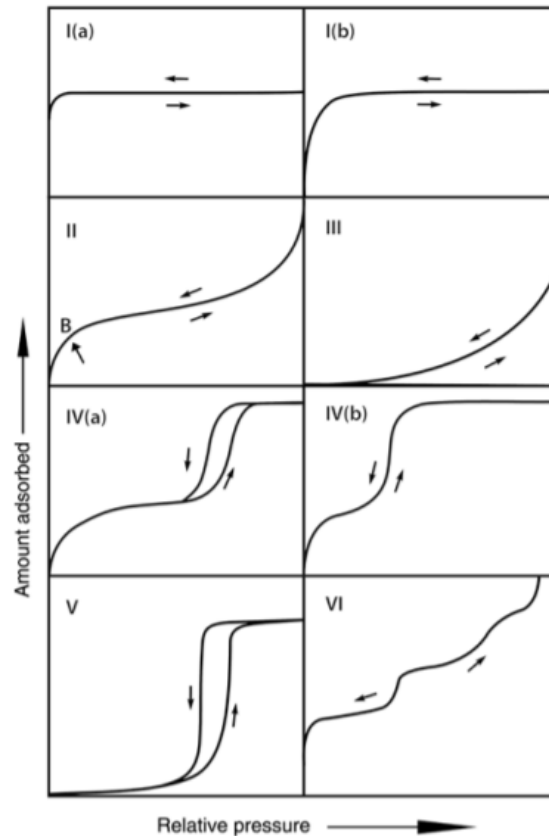


**Figure 5.1:** IUPAC classification of physisorption isotherms from ref. [31]

- The reversible Type I isotherm is a concave curve given by the presence of a microporous solid. It is called Langmuir isotherm and consists of a monolayer coverage due to the small pore size
- The reversible Type II isotherm is the typical curve obtained with non-porous or macroporous solids. The graph shows an inflection point (point B in Figure 12) which represents the achievement of a monolayer coverage and the start of a multilayer adsorption
- The reversible Type III isotherm is a convex curve. As it does not exhibit a point B like in the previous case, there is no monolayer formation. The adsorbent-adsorbate interactions are fairly weak, and molecules are preferentially adsorbed on other molecules
- The reversible Type IV isotherm is typical of mesoporous adsorbents. A peculiarity of this curve is the presence of a hysteresis loop associated with a pore capillary condensation at a pressure less than the saturation one. Different materials can show various types of hysteresis loops, from which it is possible to achieve information about the pore shapes. The first part of the chart, as described in the case of Type II, consists of an inflection point typical of monolayer adsorption of molecules
- The reversible Type V isotherm is uncommon and, like Type III curve, the adsorbent-adsorbate interactions are weak. This behaviour is observed for water adsorption on hydrophobic materials
- The reversible Type VI isotherm represents layer-by-layer adsorption on a uniform non-porous surface

During the procedure, multilayer adsorption can occur, and consequently, not all the molecules are in contact with the surface of the sample. It is still possible to calculate the volume of molecules adsorbed in a monolayer, as well as the surface area, with the Brunauer-Emmett-Teller (BET) method. In the BET theory, only the first layer of molecules is energetically attracted to the solid surface; for the other layers, a layer acts as an adsorbent site for the molecules of the upper level. The interactions between the molecules in multilayer adsorption are considered equal to the forces responsible for the condensation of a gaseous phase [32].

The distribution of the pore volume as a function of the pore size is called pore size distribution and is obtained through the application of the Kelvin equation to the system.

## 5.2 Temperature-Programmed Techniques

Temperature-programmed (TP) techniques are used to evaluate the reactivity of the different species formed on a catalytic material due to temperature variations. In a typical TP analysis, the catalyst is put in a reactor (furnace) with controllable heating rates, generally 5-20°C/min, under a constant flow rate of a gas stream [33]. The outgoing gases are monitored in a thermal conductivity detector (TCD) and/or in a mass spectrometer (MS).

### 5.2.1 Temperature-Programmed Reduction (TPR)

The temperature-programmed reduction is implemented to study the redox properties of the bulk and supported metal heterogeneous catalysts. The TPR analysis involves the use of a hydrogen or carbon monoxide stream (molar fraction 3-15%) in nitrogen or helium to evaluate the effectiveness of these substances when the oxidation state of a catalyst is decreased by temperature variations, according to Equation (5.2) [34].



TPR measurements are typically used to find the optimal temperature for the metal oxide reduction. The reducibility of a catalyst is a fundamental point in the evaluation of its oxidative properties.

### 5.2.2 Temperature-Programmed Oxidation (TPO)

In temperature-programmed oxidation, the catalyst is treated with an oxygen flux in a gaseous carrier, such as helium. A TPO analysis can be used to understand the optimal regeneration temperature for a catalyst affected by coking deactivation. Furthermore, this method is fundamental in the oxidation reactions for the catalytic activity evaluation, using, in addition to oxygen, the substances to be oxidised.

### 5.2.3 Temperature-Programmed Desorption (TPD)

A temperature-programmed desorption enables the evaluation of the species linked with the active sites of a catalyst by heating the sample under an inert gas flow. Moreover, this technique is commonly used for the determination of the relative-strength distribution of acidic sites treating the fresh catalyst with a probe molecule, such as ammonia or carbon dioxide. Subsequently, as seen before, the catalyst is heated using a carrier gas flow and the desorbed gas is monitored with a downstream detector as a function of temperature [33]. The desorption

temperature is an essential information to understand the relative strength of catalytic species: molecules with a high desorption temperature are bonded with stronger acidic sites.

#### 5.2.4 Thermal Gravimetric Analysis (TGA)

The thermal gravimetric analysis is based on the mass change as a function of temperature. As it is possible to operate under different conditions, the atmosphere used in the experimental procedure plays an essential role in the analysis results. The sample weight loss can occur due to the presence of several phenomena such as the evaporation of volatile compounds, gases desorption, loss of water and the decomposition of organic substances in the presence of oxygen. Furthermore, a TGA analysis enables the percentage weight quantification of complex heterogeneous compounds such as the diesel particulate, combining the system with a mass spectrometer for outgoing components evaluation.

TGA data can be used in technologically advanced software for the global kinetic parameters determination. For that reason, it is possible to evaluate the activation energy  $E_a$ , the pre-exponential factor  $A$  and the reaction order  $p$  of the studied chemical reaction [35]. The reaction rate expression applied to a thermogravimetric analysis can be written according to Equations (5.3) and (5.4), where  $k$  is the rate coefficient and the function  $g(m)$  depends on the reaction mechanism.

$$-\frac{dm}{dt} = k \cdot g(m) \quad (5.3)$$

$$g(m) = m^p \quad (5.4)$$

Considering  $g(m)$  equal to the weight raised to the reaction order  $p$  and  $k$  in agreement with the Arrhenius equation it is possible to obtain a more sophisticated equation both in differential and integral form. Using Equation (5.5) and (5.6) it is possible to obtain a kinetic evaluation of a given reaction through the thermogravimetric data.

$$-\frac{dm}{dt} = A e^{\frac{-E_a}{RT}} \cdot m^p \quad (5.5)$$

$$\Delta m = -A e^{\frac{-E_a}{RT}} \cdot m^p \cdot \Delta t \quad (5.6)$$

Equation (5.7) can be applied in the study of parallel or consecutive reactions.

$$\Delta m = \sum_i \Delta m_i = \sum_i -A_i e^{\frac{-E_a}{RT}} \cdot m_i^p \cdot \Delta t \quad (5.7)$$

### 5.3 Electron microscopic techniques

Electron microscopy in the catalytic field provides high-resolution real images of the considered catalyst and, depending on the accelerated electron energy, two different types of microscopic analysis can be performed. The combination of morphological, crystallographic and structural information is the result of a visual characterization, useful for a more complete study of the catalytic system in a qualitative way.

#### 5.3.1 Transmission Electron Microscopy (TEM)

The transmission electron microscopy is an important tool to probe the shape, the size and the local defects of crystalline materials. High-resolution images are obtained from a TEM analysis using high-energy electrons, of approximately 100 KeV. Electrons are more advantageous than photons because they can move with smaller wavelengths compared to the light. The maximum magnification for an optical microscope is 1200x and with a TEM microscope, it is possible to get enlargement up to 1.000.000x [36]. The observed sample must be thin enough for the transmission of a sufficient number of electrons: this is the biggest limitation for the TEM microscopy. However, observations on powdered materials are also possible following a specific preparation method. In this regard, the powder is suspended in an alcoholic solution and put in an ultrasonic bath in order to avoid the agglomerations formation. To perform the TEM analysis, a small quantity of this solution is placed on a fine copper net, which in turn is put on a polymeric grid.

TEM investigations can be used for different purposes: the determination of the shape and the distribution of small clusters of atoms on porous materials, the observation of the catalytic deactivation processes, such as coking or the sintering of active sites and, in case of nanocrystals, the evaluation of the main exposed planes, which are responsible for greater or less activity of the catalytic reactions [37].

#### 5.3.2 Scanning Electron Microscopy (SEM)

The scanning electron microscopy is the most widely used surface technique. In a SEM analysis, a primary electron beam interacts with the catalyst at an energy range between 0.5 and 30 eV, much smaller than the range required in TEM technology. The electron-surface interplay can generate the following species [38]:

- Backscattered electrons (BSE) coming from an elastic scattering with approximately the same energy of primary electrons. The BSE intensity can be correlated with the atomic number of the elements present in the interactive volume between primary electrons and the sample
- Secondary electrons (SE) which are low energetic species (< 50 eV) used for the obtainment of a high-resolution image
- Transmitted electrons (TE) for the obtainment of additional information on the structure of the sample
- Characteristic X-rays essential for the elementary composition determination of the interested interactive volume

The sample surface image is obtained by measuring the secondary electrons intensity. Additionally, the presence of backscattered and transmitted electrons combined with the characteristic X-ray emission provide qualitative information about the elemental composition of the sample.

## 5.4 Spectroscopic techniques

Especially in recent years, spectroscopic techniques have become essential for a very thorough study of the heterogeneous catalysts. Scientists, indeed, are interested in understanding the complex factors that describe a catalytic process to optimize the activity and the selectivity of the chemical reactions through an elaborate design of the catalytic system. The operative conditions of the first spectroscopic investigation were based on a very high vacuum level, therefore there was a gap between the study conditions and the real applications. This difference is now getting smaller and smaller due to the presence of in situ and in operando methods, which have made the on-line spectroscopy an increasingly widespread technology. Vibrational methods are probably one of the most powerful tools for the catalytic characterization. In this regard, IR and Raman spectra allow to define the nature of chemical bonds, to study the chemical structures of intermediates species, which explain a reaction, and to examine the defective sites of a catalyst [39].

### 5.4.1 X-Ray Diffraction (XRD)

X-rays are high-energy electromagnetic waves with a wavelength between  $10^{-3}$  and  $10^1$  nm [40], thus, they have enough energy to penetrate a solid to probe its internal structure. The XRD technique is based on the elastic scattering of X-ray photons by atoms in an ordered lattice. In a polycrystalline material, X-rays are diffracted by the crystalline phases according to the Bragg's law [36], Equation (5.8).

$$n \lambda = 2 d \sin \theta \text{ where } n = 1, 2, \dots, d \quad (5.8)$$

In Equation (15)  $n$  is the order of diffraction,  $\lambda$  is the wavelength of the incident beam in nm,  $d$  is the lattice spacing in nm and  $\theta$  is the diffraction angle, as illustrated in Figure 5.2.

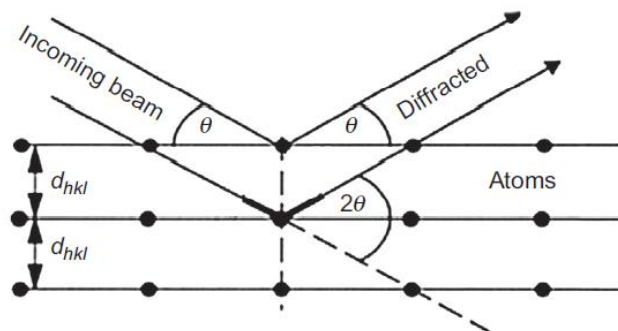


**Figure 5.2:** Geometrical conditions for the diffraction phenomenon from ref. [40]

The outcome of an XRD analysis is a diffraction pattern in which the intensity of X-rays is plotted as a function of the diffraction angle; therefore, it is possible to identify the different crystalline phases present in the studied sample. The diffraction pattern of a material is composed of several peaks due to the presence of different crystalline planes, characterized by a specific triad of Miller indices.

The crystallites size is another remarkable information achieved from an XRD analysis through the Debye-Scherrer formula [36], as per Equation (5.9).

$$D = \frac{k \lambda}{b \cos \theta} \text{ with } k \text{ generally equal to } 0.9 \quad (5.9)$$

In Equation (16)  $b$  is the peak width at mid-height and  $k$  is a constant which represents the crystallites sphericity.

#### 5.4.2 X-Ray Photoelectron Spectroscopy (XPS)

In an XPS analysis, the sample is irradiated with monochromatic X-ray photons, which do not have sufficient energy to go deep into the sample. That is the reason why this technique allows the study of some surface features of a solid. In this context, the X-Ray photoelectrons spectroscopy is based on the photoelectric effect observed for the first time by Hertz in 1887 [41]. Therefore, electrons can adsorb an incident photon, obtaining enough energy to leave the atom and to run away from the surface of the sample with characteristic kinetic energy given by Equation (5.10) in which  $h\nu$  is the energy of the incident photon and  $E_b$  is the binding energy [36].

$$E_k = h\nu - E_b \quad (5.10)$$

Considering that the electrons of each element have characteristic binding energies, the surface elemental composition of a material can be analysed using the XPS technology.

Moreover, the information about the oxidation state of the elements and their chemical environment can be found with the XPS technique. According to the different atoms present in the studied structure, a variation of the binding energy is observed through a chemical shift in the XPS pattern, which is generally included between 0 and 3 eV. As a general rule, the binding energy increases with the oxidation state and, for an established oxidation state, with the electronegativity of ligands [42].

#### 5.4.3 Raman Spectroscopy

Raman spectroscopy is a powerful tool for the study of the active species formed on the surface of a catalyst and for the investigation of the chemical structure of materials with particular focus on their defect sites. The fundamental principle of this technique is the Raman effect, thus, when the photons of the incident light interact with the phonons of a material, the light can undergo an inelastic scattering process [43].

Going into the details, when a monochromatic light beam interacts with a sample, it is scattered according to different processes, as shown in Figure 5.3. The largest part of the scattered light follows the Rayleigh scattering procedure. Therefore, during the light-sample interaction, the system goes from a fundamental vibrational level to an excited state and it quickly returns to the starting position without an energy transfer between the incident light and the scattered light. This latter maintains the same frequency and wavelength of the incident one. The elastically scattered light fraction must be removed in a Raman spectrometer avoiding obscuring the Raman signals. Conversely, a little amount of light is scattered in an inelastic way, thus, it shows different wavelength compared to the incident radiation. Starting from fundamental vibration energy, the system reaches an excited state returning then to a different state, compared to the initial one. The inelastic scattering was studied by Smekal in 1923 and was experimentally observed by Raman in 1928. Raman scattering can be classified in Stock Raman Scattering and anti-Stock Raman scattering. The anti-Stokes Raman scattering phenomenon occurs when the scattered light has higher energy and lower wavelength than the incident beam. In the Stokes Raman scattering, instead, the scattered light has lower energy and higher wavelength than the incident light [43], [44].

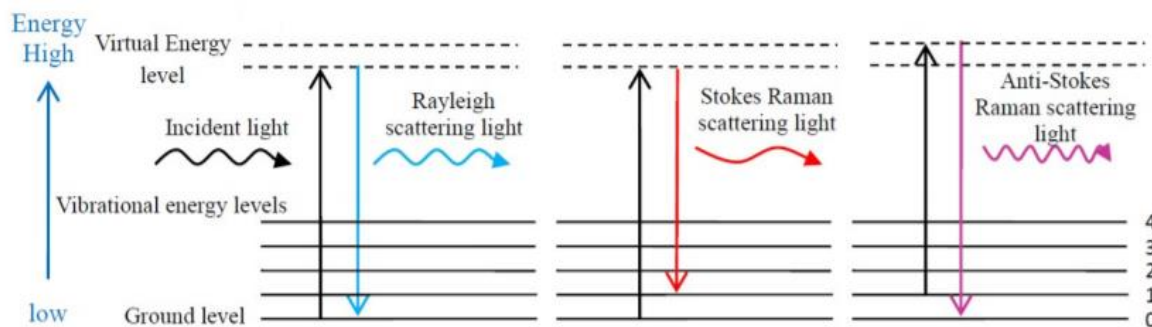


**Figure 5.3:** Rayleigh and Raman scattering processes from ref. [43]

Figure 5.4 shows all the information obtainable from a typical Raman spectrum depending on the Raman shift, represented by the energy difference between the incident light and the scattered light. This latter is generally expressed in wavenumbers.

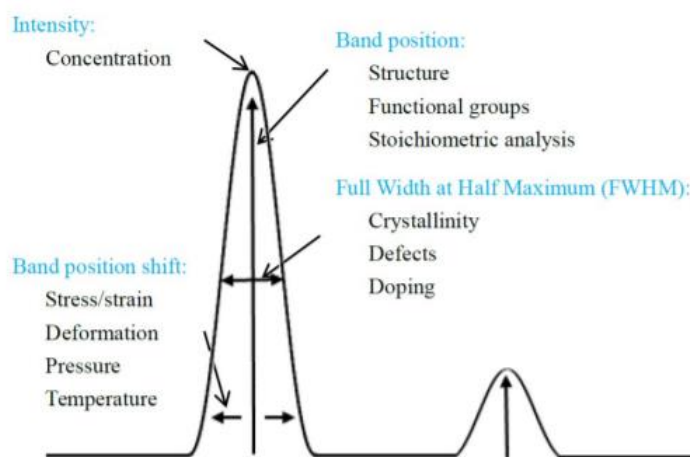


**Figure 5.4:** Information from a Raman spectrum from ref. [43]

#### 5.4.4 IR Spectroscopy

##### Principles and applications

IR spectroscopy is based on the interaction between the IR radiation and the studied sample. This technique allows the study of material in three levels of detail; therefore, it is considered one of the most effective spectroscopic method for catalyst characterization. First of all, IR spectroscopy is used for the examination of the surface features of heterogeneous catalysts. This technology is also a powerful tool for the identification of the nature of acidic and basic sites of a metal oxide, testing the sample with a specific probe molecule. Finally, using in situ and in operando methods, it is possible to describe the reaction mechanism of a catalytic reaction studying the different species, which are formed on the catalyst surface in different operative conditions.

Concerning the development of this technology, in the nineteenth century, the astronomer William Herschel demonstrated for the first time the existence of IR radiations [45]. The use of IR spectroscopy in the surface investigation and in the catalytic research has grown rapidly

starting from the work of Terenin and other Russian researchers around the middle of the 20th century up to the important studies of Eischens on supported catalysts [46].

IR radiations are invisible to the human eye and, as illustrated in Figure 5.5, are characterized by a larger wavelength compared to the visible region. The IR area is divided into three different segments [45]:

- The near-infrared (NIR) between 750 and 2500 nm or 13333 and 4000  $\text{cm}^{-1}$
- The mid-infrared (MIR) between 2500 and 25000 nm or 4000 and 400  $\text{cm}^{-1}$
- The far-infrared (Far IR) between 25 and 1000  $\mu\text{m}$  or 400 and 10  $\text{cm}^{-1}$

The mid-infrared region is the most important region for the vibrational spectroscopy and, in general, the absorption of infrared radiation causes an energy change of about 2-10 kcal/mol.

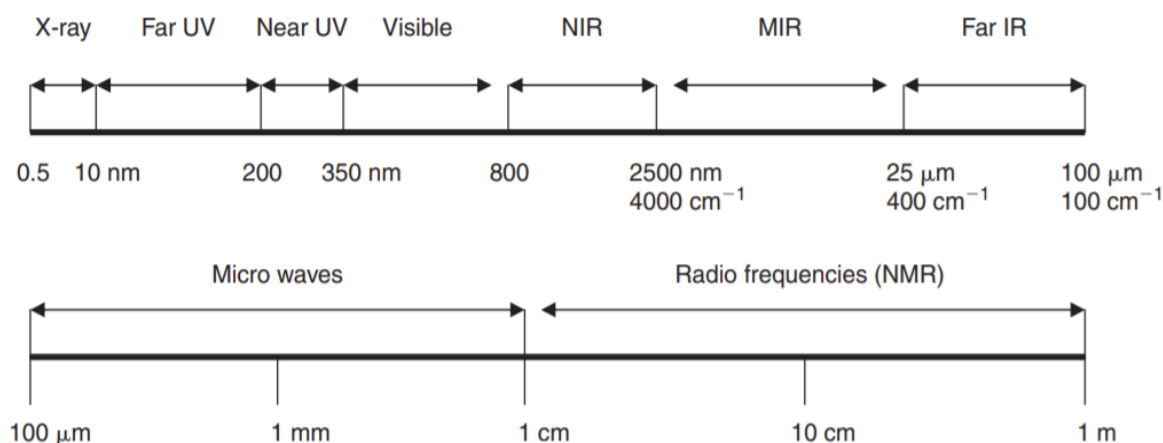


**Figure 5.5:** Electromagnetic spectrum of light from ref. [45]

The IR spectroscopy is based on the interaction between IR radiations and a molecule to magnify its natural oscillations in terms of interatomic distances and bond angles. According to the classical theory, a molecule can be treated as a set of harmonic oscillators and the chemical bond is represented as a spring in which the oscillating masses are the bonding atoms. The energy connected with this oscillation is shown in Equation (5.11), in which  $h$  is the Planck constant and  $\nu$  the oscillation frequency.

$$E_{\text{vibrational}} = h \nu \quad (5.11)$$

If an IR radiation has a frequency equal to that of the natural oscillation of the molecule, it is absorbed causing an increase in the oscillations amplitude of the system. Furthermore, the vibration movement must provide a dipole moment variation; therefore, the vibrating molecule produces an electric field capable of exchanging energy with the electromagnetic waves. This is the fundamental condition for an IR adsorption.

Quantum mechanics, instead, provides a more complete interpretation of this phenomenon. According to the quantum theory, the vibration energy of molecules is quantized and only adopts the values obtained by Equation (5.12).

$$E_{\text{vibrational}} = \left( K + \frac{1}{2} \right) h \nu \quad \text{where } K = 0, 1, 2, \dots \quad (5.12)$$

Following a general rule, in Equation (5.12) all molecules are in their fundamental vibration state in normal conditions because the thermal energy of a molecule at room

temperature is lower than the energy required to jump from the ground state to higher levels. In this regard, the absorption of IR radiations causes almost exclusively the transition between  $K=0$  to  $K=1$ , therefore the permitted transitions are characterized by a  $\Delta K$  equal to  $\pm 1$ . Moreover, according to quantum mechanics, the chemical bond is described as an an-harmonic oscillator as the retraction force is not perfectly proportional to the elongation [47].

Furthermore, the number of vibrational degrees of freedom for a molecule can be calculated using Equation (5.13) and (5.14) considering a polyatomic molecule constituted by  $n$  atoms.

$$\text{Vibrational DOF for a nonlinear molecule} = 3n - (3 + 3) \quad (5.13)$$

$$\text{Vibrational DOF for a linear molecule} = 3n - (3 + 2) \quad (5.14)$$

Where:

- $3n$  is the number of degrees of freedom of the molecule
- 3 is the number of translational degrees of freedom of the molecule
- 3 or 2 are the numbers of rotational degrees of freedom for a nonlinear and linear molecule respectively

Two main types of vibrations are possible. In particular, the stretching vibration is caused by a rhythmic elongation along the bonding axis and its absorption bands fall at higher wavenumbers compared to the bending vibrations, which are linked to the bonding angle variations. As explained in Figure 5.6, in an IR spectrum there are bands due to both stretching and bending vibrations [45].

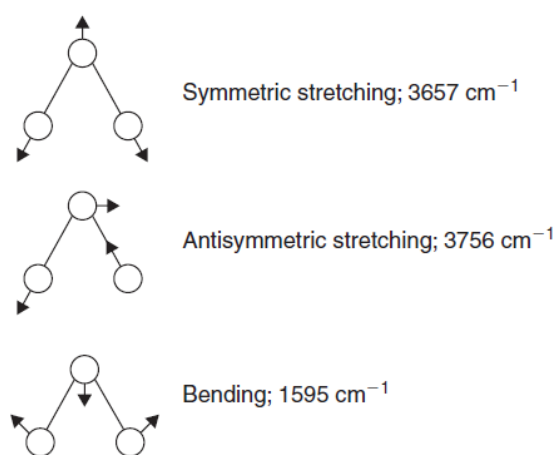


**Figure 5.6:** Stretching and bending vibrations of a water molecule from ref. [45]

The result of an IR analysis is a graph in which the absorption intensity is plotted as a function of the wavenumber. The definition of this latter is shown in Equation (5.15) and is proportional to the energy difference between the ground and the first excited vibrational state [44].

$$\text{Wavenumber} = \frac{1}{\lambda} \quad (5.15)$$

The absorption bands present in the graph are characterized by the position, the intensity and the shape and are used for a quantitative and qualitative investigation of the several chemical species formed on the catalyst surface.

## FT-IR spectrophotometers

The IR spectrophotometers are based on the working principle of the Michelson interferometer, which dates back to the second half of the 19th century. During the same years, Lord Rayleigh realized that the results obtained by the interferometer could be converted into a spectrum using the Fourier transformation. However, the dispersive instruments were slowly replaced by FT-IR spectrophotometers only in 1960 [48].

An interferometer is an optical device for the controlled generation of time-dependent interferograms. As shown in Figure 5.7, it consists of a beam splitter, a moving mirror and a fixed one. The incident IR light, coming from the source, is divided into two equal parts due to the presence of the beam splitter, therefore 50% of the radiations is transmitted to the moving mirror and the other 50% is reflected on the fixed one. Then, the two reflected beams are recombined at the beam splitter and, crossing the sample, are sent to the detector. The difference between the distances covered by the light beams, caused by the movement of the moving mirror, is called optical retardation. The working principle of this device is easily understood when the source contains a single monochromatic wavelength. In this regard, whenever the moving and fixed mirrors are in an equal position compared to the beam splitter, the optical retardation is zero and the combination of the light beams provides a constructive interference. Therefore, the maximum signal at the detector is observed when the optical retardation is equal to an integer multiple of the wavelength, such as  $0$ ,  $\lambda$ ,  $2\lambda$  and so on, and conversely, it is minimum with a destructive interference at optical retardation values with intervals of  $\lambda/2$  [49]. Finally, it is possible to convert the interferogram into a spectrum using the Fourier transformation (FT).

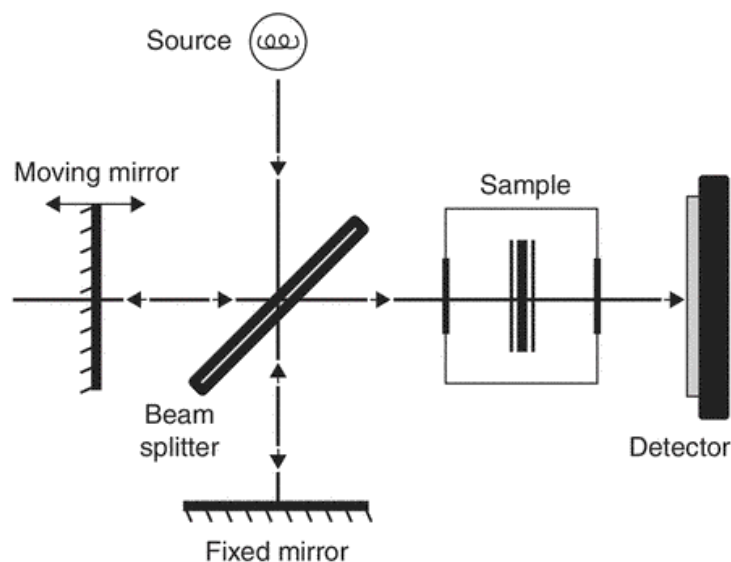


**Figure 5.7:** Schematic illustration of a Michelson interferometer from ref. [48]

## Study of the acidic and basic properties of the catalytic surfaces through IR spectroscopy

The catalytic properties of several heterogeneous catalysts are associated with the acidic and basic groups present on their surface. In this regard, IR spectroscopy is a powerful tool to distinguish the type (Brønsted or Lewis sites) and the nature (type and strength) of these sites taking advantage of the interaction between the sample and a probe molecule [50]. The probe molecules are simple molecules that can bind to the acid/base sites of a material with the formation of a real chemical bond. This interplay causes a change in the vibration frequency of the used molecule.

The interactions between the most used probe molecules and the metal oxides are described in the rows below. Generally, for these studies, the catalytic sample is preheated in the presence of oxygen. Subsequently the temperature is lowered to the desired value and the probe molecule is sent to the system. Furthermore, a successive flow of an inert gas is necessary to obtain stable spectra [51].

### 1) Ammonia as a probe molecule for the acidic sites characterization

The spectra obtained from the probe molecule-sample interaction is shown in Figure 5.8. A band around 1450  $\text{cm}^{-1}$  confirms the production of ammonium ions ( $\text{NH}_4^+$ ) resulting from the reaction between ammonia and Brønsted sites, instead, the bands around 1200 and 1620  $\text{cm}^{-1}$  derive from the interaction of ammonia and Lewis sites [51].  $\text{CeO}_2$  and  $\text{ZrO}_2$  show only Lewis acidity instead of  $\text{Al}_2\text{O}_3$ ,  $\text{TiO}_2$  and  $\text{Nb}_2\text{O}_5$ , which present both Lewis and Brønsted sites.

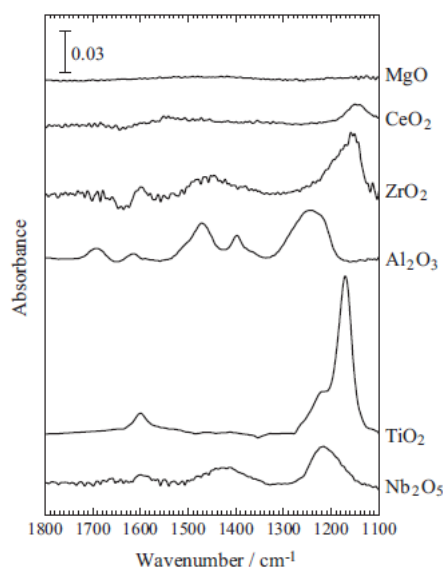


**Figure 5.8:** IR spectra of ammonia adsorbed at 150°C on different metal oxides from ref. [51]

### 2) Pyridine as a probe molecule for the acidic sites characterization

According to Figure 5.9, the reaction between pyridine and Brønsted acid sites is observed due to the formation of pyridinium ion  $\text{PyH}^+$  with bands around 1545 and 1638  $\text{cm}^{-1}$ , conversely, the interaction with Lewis sites occurs because of the presence of bands around 1445 and 1610  $\text{cm}^{-1}$  [51].

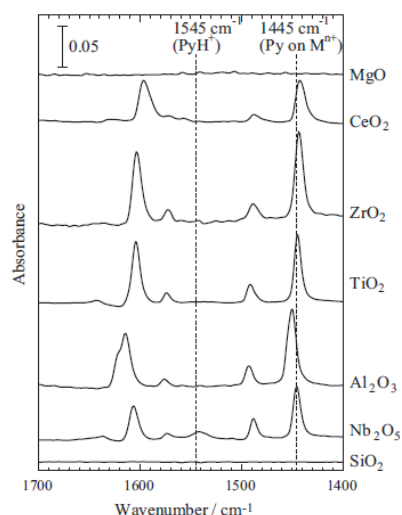


**Figure 5.9:** IR spectra of pyridine adsorbed at 150°C on different metal oxides from ref. [51]

The IR spectra obtained with pyridine provide different results compared to the previous experiment, indeed only Nb<sub>2</sub>O<sub>5</sub> shows Brønsted acidic sites. Generally, the interaction between pyridine and metal oxides allows the formation of bands more defined and spaced compared to the ammonia results, although the use of this latter is preferred due to the higher toxicity of pyridine.

### 3) CD<sub>3</sub>CN as a probe molecule for the acidic sites characterization

The acetonitrile molecule is particularly sensitive to the uncoordinated cations which are present on the surface of the materials, indeed the bands around 2300 cm<sup>-1</sup> are assigned to the interaction between CD<sub>3</sub>CN and Lewis acidic sites, as shown in Figure 5.10. It is also important to note that the characteristic band of CD<sub>3</sub>CN is at 2265 cm<sup>-1</sup> in the liquid phase and the interaction of these probe molecules with all the metal oxides, except for SiO<sub>2</sub> and MgO which do not have acidic sites, shows a peak shift compared to the previous value. The band shift is linked to the strength of the acidic sites present on the material surface and, in this particular case, the higher is the acidity of the solid, the greater is the shift [51].

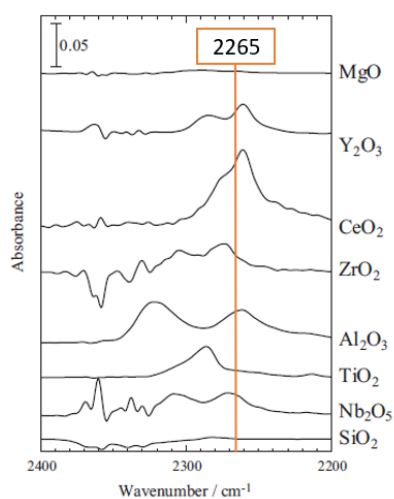


**Figure 5.10:** IR spectra of CD<sub>3</sub>CN adsorbed at 30°C on different metal oxides adapted from ref. [51]

Therefore, using IR spectroscopy it is possible to have a qualitative idea of the strength of the acidic sites on a material. This analysis is also possible for the other probe molecule, although with pyridine the shift is very small and in the case of ammonia, the evaluation is difficult due to the presence of not well-defined peaks.

#### 4) CO<sub>2</sub> and CHCl<sub>3</sub> as probe molecules for the basic sites characterization

Carbon dioxide can be a good probe molecule to characterize the type of basic sites on the surface of a material and to test their stability with the temperature. However, it is an unsuitable molecule to study the strength of the basic sites because of the complexity of the obtained spectra. Indeed, the interaction between the CO<sub>2</sub> and the solid allows the formation of several species such as formates and different types of carbonates. Furthermore, it is necessary to take into account that the metal oxides are generally ionic solids, thus their structure consists of Lewis acidic sites adjacent to basic sites forming an acid-base pair. The CH<sub>3</sub>Cl molecule can be used to study the different nature of acidic and basic sites present on the material surface. As illustrated in Figure 5.11, there are different types of interactions between the probe molecule and the material sites [51]:

- a: interaction between CH<sub>3</sub>Cl and basic sites
- b: interaction between CH<sub>3</sub>Cl and acid-base pairs
- c: interaction between CH<sub>3</sub>Cl and Lewis acidic sites

Considering that the C-H stretching of CH<sub>3</sub>Cl shows a band at 3033 cm<sup>-1</sup> in the liquid phase, the first two cases are characterized by a redshift in the spectrum, in other words, a movement of the band towards smaller wavenumbers compared to the previous value, whereas the third case presents a blueshift to high wavenumbers.

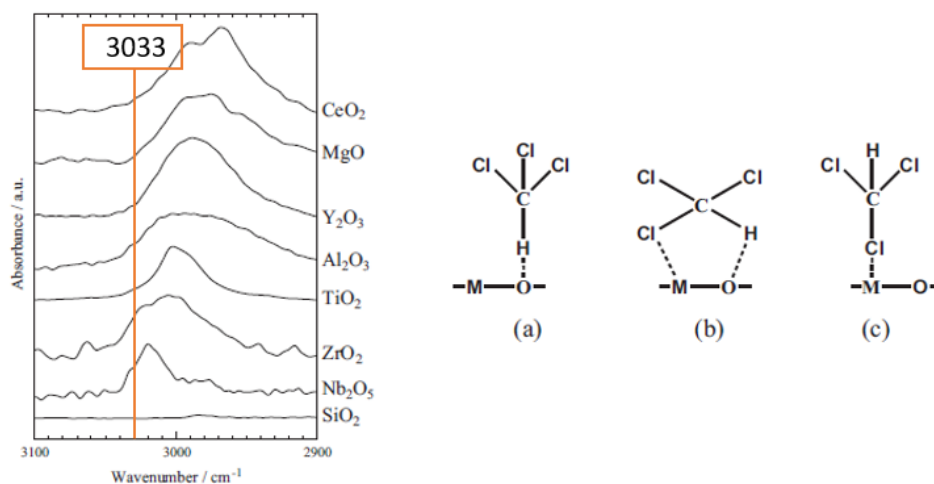


**Figure 5.11:** IR spectra of CH<sub>3</sub>Cl adsorbed at 30°C on different metal oxides and the different types of interactions adapted from ref. [51]

### Determination of the number of basic and acidic sites

The interaction between a probe molecule and a catalyst also allows a quantitative analysis of the number of acidic and basic sites. For the determination of the number of acidic sites is important to choose a material with predominantly Lewis or Brønsted domains. First of all, it is necessary to obtain IR spectra of the material by increasing the amount of probe molecule. The IR intensity increases linearly with the adsorbed probe molecule; therefore, it is possible to obtain a graph in which the slope is an estimation of the molar extinction coefficient. Finally, the number of acidic and basic sites can be calculated from the Lambert-Beer law described in Equation (5.16), in which  $m$  is the weight (kg),  $C_w$  the acid/base sites concentration (mol/kg) and  $S$  the disk area (m<sup>2</sup>).

$$A_{IR} = \frac{\varepsilon m C_w}{S} \quad (5.16)$$



## 6. Ceria catalysts

Rare earth elements and their oxides are used in different fields and the catalysis is their third most important technological application [52]. They consist of 17 elements and among them, cerium and lanthanum represent about two-third of the worldwide consumption of rare earth elements [53], as demonstrated by Figure 6.1.

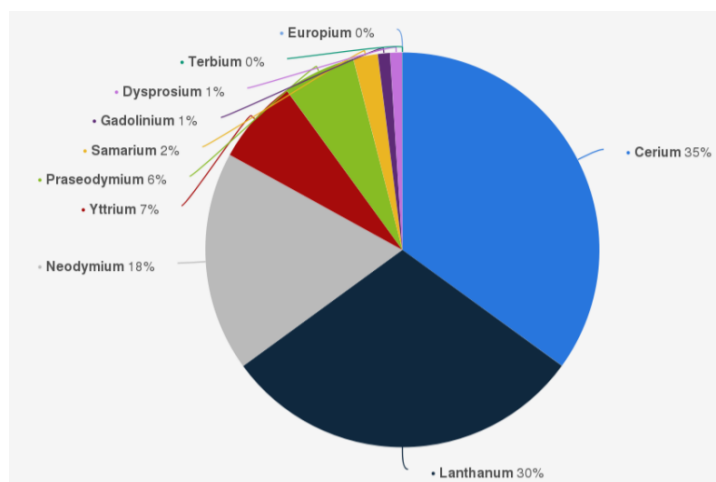


**Figure 6.1:** Distribution of rare earth consumption volume worldwide in 2018 by element from ref. [53]

Cerium oxide is one of the most studied materials in the field of environmental catalysis, especially for the catalytic oxidation reactions [54]. Ceria can also be used as a support in heterogeneous catalysis and doped with foreign cations to obtain solid solutions with different compositions in order to improve the catalytic activity of the system whilst making the reaction more stable.

### 6.1 General proprieties of ceria catalysts

#### 6.1.1 Redox features and Oxygen Storage Capacity (OSC) property

The stoichiometric ceria ( $\text{CeO}_2$ ) is characterized by a yellow colour and has a fluorite structure with atoms arranged in a face-centred cubic unit cell. At high temperature and in a reducing atmosphere, it can release oxygen atoms with the formation of nonstoichiometric  $\text{CeO}_{2-x}$  oxides, in which  $x$  is between 0 and 0.5 [55]. The unique redox nature of ceria is studied worldwide. Cerium oxide can quickly store and release oxygen due to the  $\text{Ce}^{4+}/\text{Ce}^{3+}$  couple maintaining a stable fluorite structure according to the fully reversible process described in Equation (6.1).



The symbol  $\square$  in Equation (24) specifies the formation of an oxygen vacancy.

The extent of this property is called Oxygen Storage Capacity (OSC). The OSC makes the cerium oxide one of the most used catalysts for catalytic oxidations. In this regard, the reactant molecules can react directly with the lattice oxygen of ceria by providing good conversion yields also in low oxygen conditions. Therefore, it is highly important to know the features and the surface property of the cerium oxide, both in the oxidized and reduced form.

According to the IR spectra, the stoichiometric form is characterized by the presence of different hydroxyl compounds which differ in the number of  $\text{Ce}^{4+}$  cations linked to the  $-\text{OH}$  group. The stretching of these species shows bands between  $3400$  and  $3700\text{ cm}^{-1}$ , as described in Figure 6.2. Furthermore, the type I hydroxyl groups, in which the  $-\text{OH}$  is connected to only one  $\text{Ce}^{4+}$  site, are less stable than the others because they disappear by increasing the temperature. It should be noted that the stretching region of hydroxyl groups changes considerably in the case of nonstoichiometric ceria. In this spectrum, indeed, there is no presence of type III hydroxyl groups [55].

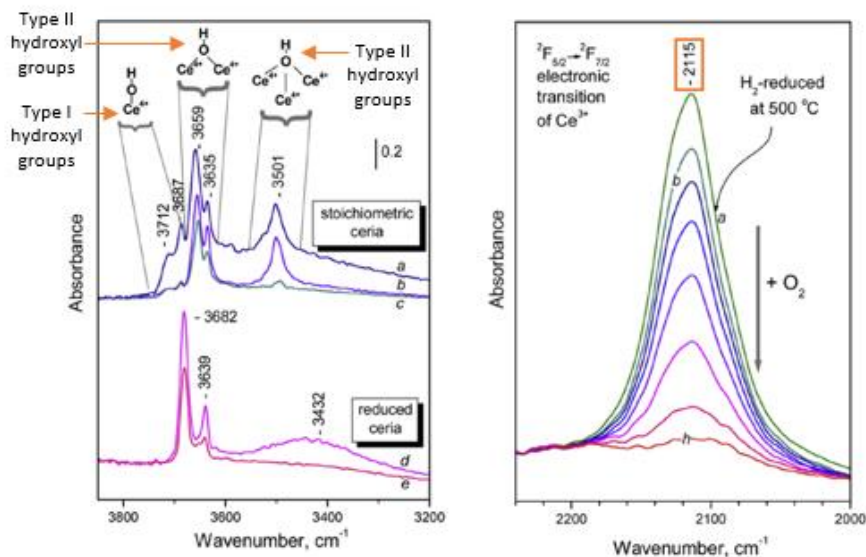


**Figure 6.2:** FTIR spectra of oxidized and reduced ceria at  $447$  (a, d),  $487$  (b) and  $500^\circ\text{C}$  (c, e) to the left & FTIR spectra of reduced ceria (a) with subsequent additions of oxygen to the system at room temperature to the right adapted from ref. [55]

It is also possible to find carbonates groups on the ceria surface due to the interaction between the material and the carbon dioxide normally present in the atmosphere. Carbonates species show bands in the region between  $1600$  and  $1260\text{ cm}^{-1}$ . The band at  $2115\text{ cm}^{-1}$  is certainly one of the most important features of the reduced ceria spectrum. Indeed, the band indicates the presence of  $\text{Ce}^{3+}$  species in the structure [55]. The band disappears by adding oxygen and the nonstoichiometric ceria is re-oxidized to  $\text{CeO}_2$ .

As described above, the oxygen storage capacity is a powerful property of ceria catalysts. More specifically, two types of OSC have been defined, namely: the total OSC and the dynamic OSC. The first is a thermodynamic parameter which defines the total transferable oxygen of a sample at a given temperature, while the second is a kinetic property linked to the mobility of surface oxygen [56]. Understanding the different factors which change the OSC property is important in order to study the best catalytic configuration and to enhance both the OSC property and the sample performance. In this context, the total oxygen storage capacity (OSCC) decreases with the addition of low-valence elements such as trivalent metals, due to the replacement of  $\text{Ce}^{4+}$  ions by non-reducible  $\text{M}^{3+}$  species [57]. Conversely, the dynamic OSC increases due to the formation of oxygen vacancies improving the oxygen mobility in the catalytic structure. Last but not least, the addition of tetravalent elements to the ceria samples represents the most effective way to improve both the total and the dynamic oxygen storage capacity [56]. Tetravalent elements can be divided into two groups: non-reducible and reducible

elements. Zirconium is an example of the first category. Different composition of  $\text{CeO}_2$  and  $\text{ZrO}_2$  enable the formation of a solid solution in which some cerium atoms are substituted by the zirconium in the lattice structure. As the Zr cations are smaller than the cerium ions, the bond distance between the oxygen and the metal in the structure increases, making the oxygen less connected to the structure - and consequently more mobile – and boosting the OSC property [58]. Regarding instead the reducible elements, the presence of other redox pairs such as  $\text{Pr}^{4+}/\text{Pr}^{3+}$  and  $\text{Ti}^{4+}/\text{Ti}^{3+}$  emphasizes the oxygen storage capacity of the ceria samples. The geometrical factors can also play an important role in this property. In this respect, the OSC increases as the surface area is increased due to the high availability of surface oxygen, which provides a major contribution to the OSC capacity [56], [59].

### 6.1.2 Ceria catalysts at nanoscale

Nowadays, it is possible to obtain ceria nanoparticles with different morphology by monitoring the different synthesis parameters such as pressure, pH and temperature. In this regard, the hydrothermal synthesis allows the obtainment of desirable nanoshapes with well-defined crystallographic planes, which instead are not obtainable with the standard preparation techniques [60].

From the thermodynamic point of view, the most stable surfaces of the ceria nanoparticles are the  $\{111\}$ ,  $\{110\}$  and  $\{100\}$ . It should be taken into account that on these surfaces the coordination number is lower compared to the bulk of  $\text{CeO}_2$  in which the cerium and the oxygen are 8 and 4 coordinated. In particular:

- In the  $\{111\}$  surface the cerium is linked to 7 oxygens and the oxygen to 3 cerium atoms
- In the  $\{110\}$  surface the cerium is linked to 6 oxygens and the oxygen to 3 cerium atoms
- In the  $\{100\}$  surface the cerium is linked to 6 oxygens and the oxygen to 2 cerium atoms

Due to the different degree of unsaturation on these surfaces, the catalytic properties of ceria nanoshapes change by preparing crystals with different exposed faces. In particular, the exposure of planes (110) and (100), rather than (111), makes ceria rods and cubes more active than octahedra [61]. TEM images for ceria octahedra, cubes and rods are illustrated in Figure 6.3.

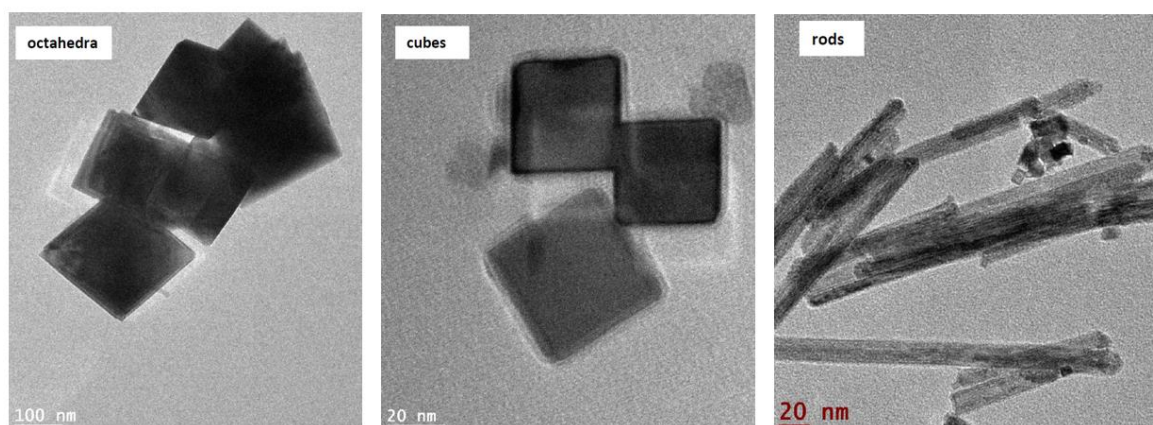


**Figure 6.3:** TEM images for ceria octahedra, cubes and rods adapted from ref. [62]

The energy of oxygen vacancies formation is characterized by the following order: (111) > (100) > (110) [63], thus the oxygen vacancies are preferentially formed on ceria cubes and rods with an increase in their oxygen storage capacity.

### 6.1.3 Ceria catalysts at nanoscale – Preparation methods

The synthesis of nanostructures catalysts is based on careful control of the nucleation and growth rates in different directions during the crystal formation. In this context, the use of organic and inorganic additives has been evaluated over the years. As shown in Figure 6.4, these compounds can interact with a family of plants freezing their growth [60]. However, when the synthesis is completed, the additive removal is necessary to obtain a material with the least amount of impurities, which could change the catalytic performance of the sample.

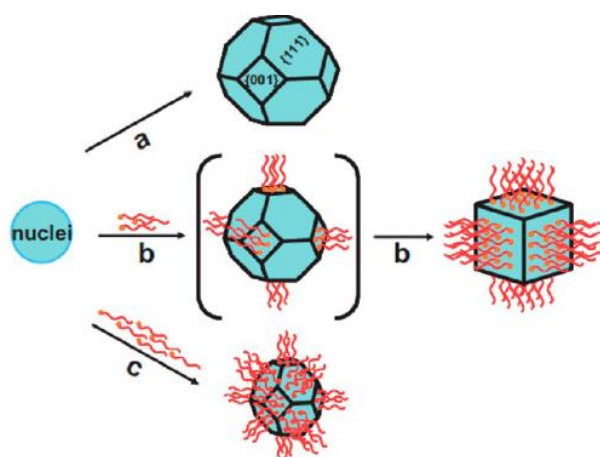


**Figure 6.4:** Shape control of ceria nanocrystals using the dodecanoic acid as an additive from ref. [64]

The hydrothermal synthesis is one of the most performing techniques to obtain nanostructured material without the use of additives. Generally, a cerium salt is dissolved in water in the presence of a base (NaOH, KOH or  $\text{NH}_3$ ). The obtained solution is placed in an autoclave for 20-50 hours at 100-200 °C: this period of time is called “the aging phase”. As mentioned in the rows above, during the aging several factors including temperature, pH, pressure and precursors features influence the synthesis of these catalysts [60]. Then, the catalyst is washed with water and ethanol and calcinated at high temperature.

Going more into details, the hydrothermal process is based on a dissolution/recrystallization mechanism. The mixing between  $\text{Ce}^{3+}$  ions coming from the cerium precursors and a NaOH solution allows the formation of anisotropic  $\text{Ce}(\text{OH})_3$  nuclei. The formation of nano-octahedra is favoured when the -OH concentration and the temperature are low. The high concentration of hydroxyl ions, on the contrary, intensifies the dissolution/recrystallization mechanism by promoting an anisotropic growth of  $\text{Ce}(\text{OH})_3$  nuclei. Therefore, the formation of ceria nanorods with preferentially (110) facets is achieved. These structures are converted into nanocubes by treating the system at high temperature [65]. The controlled synthesis of ceria nanoshapes is illustrated in Figure 6.5.

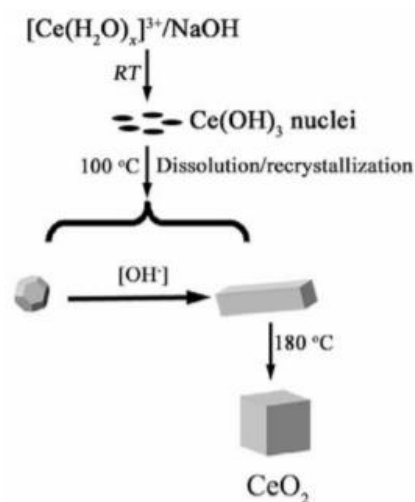


**Figure 6.5:** Controlled synthesis of ceria nanoshapes from ref. [65]

The nature of the precursor or the presence of foreign ions can affect the hydrothermal synthesis. In this regard, the presence of chlorine ions facilitates the formation of an elongated structure, whereas the  $\text{NO}_3^-$  ions promote the nanocubes production [60]. Concerning the last point, it is possible to study the effect of the sodium nitrate addition as a surface modifying agent (SMA) during the hydrothermal synthesis. As shown in Figure 6.6, it is possible to obtain smaller and smaller nanocubes with a size of about 10-15 nm by increasing the ratio between the  $\text{NaNO}_3$  and the cerium nitrate. This additive not only allows the formation of a preferential nanostructure, but it is also able to block the development of the others. Therefore, the sodium nitrate can bind to (100) facets destabilizing the formation of nanorods and octahedra [66].

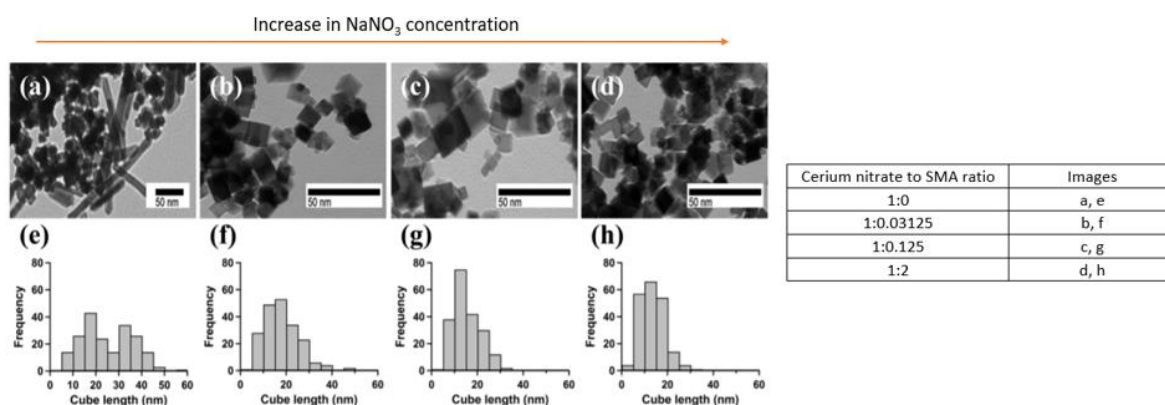


**Figure 6.6:** TEM images and size distribution of nanostructured ceria synthesized with a different ratio between cerium nitrate and SMA adapted from ref. [66]

Another method for the ceria nanoparticles production is the solution combustion synthesis (SCS). In this procedure, cerium precursor and a fuel are dissolved in a solvent and subsequently treated at high temperature. As demonstrated by Figure 6.7, catalysts synthesized via the SCS technique show a porous, foam-like structure due to the very fast combustion, which releases a large amount of gases. The use of various fuels, such as glycine or urea, and

various solvents, e.g. water, acetone and ethanol, allows the production of samples with different activity in the oxidation reactions [67].

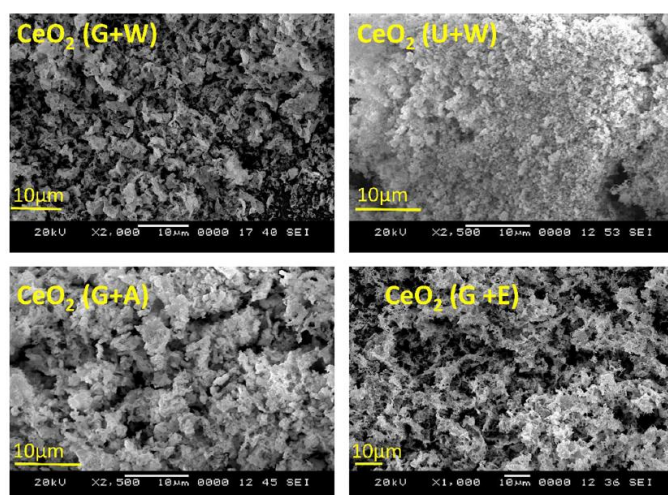


**Figure 6.7:** SEM images of CeO<sub>2</sub> samples prepared via the SCS method with different solvents and fuels from ref. [67]

## 6.2 Characterization of ceria catalysts

The properties obtained both from the physisorption of nitrogen at 77 K and the performed X-ray diffraction analysis of different ceria catalysts are presented in Table 6.1. In particular, the features of ceria nanoshapes synthesized through the hydrothermal method are compared with the sample prepared via the SCS method. The particles size is evaluated through the Scherrer's equation and falls into the range between 30 and 50 nm. The specific area of ceria nanocubes and nanorods is relatively small, whereas a higher value is observed for catalysts prepared via the SCS method. The presence of (111), (200), (220), (311), (222) and (400) planes shows the presence of the typical cubic fluorite structure [68], [69]. It is also possible to estimate the relative amount of (110), (100) and (111) planes from the XRD peaks intensity. In this regard, a larger amount of (100) and (110) planes is observed in ceria nanocubes and nanorods compared to the sample synthesized via the SCS method due to the high (200)/(111) and (220)/(111) ratios.

**Table 6.1:** Main properties of CeO<sub>2</sub> catalysts from N<sub>2</sub> physisorption at 77K and the XRD analysis adapted from ref. [69]

Catalyst	S <sub>BET</sub> (m <sup>2</sup> g <sup>-1</sup> )	Particle size (nm)	XRD peak intensity ratio (200)/(111)	XRD peak intensity ratio (220)/(111)
Ceria nanocubes	4	54	0.33	0.75
Ceria nanorods	4	43	0.32	0.71
Ceria via SCS method	69	35	0.27	0.49

The X-ray diffractograms of ceria nanorods, nanocubes and nano-octahedrons obtained through the hydrothermal method are shown in Figure 6.8.

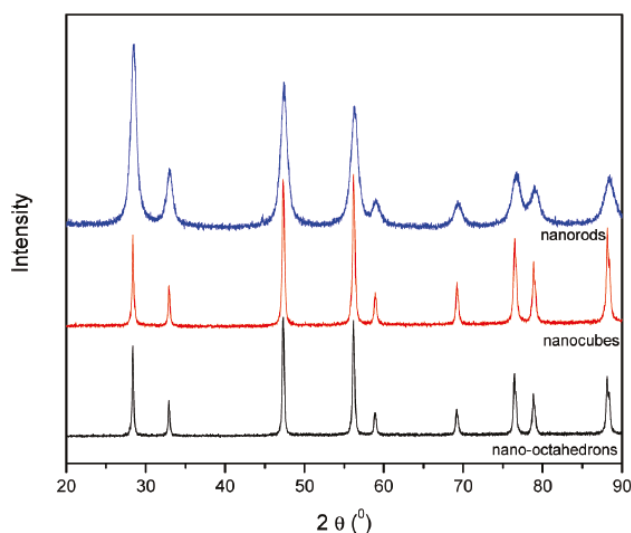


**Figure 6.8:** X-ray diffractograms of ceria nanorods, nanocubes and nano-octahedrons adapted from ref. [70]

Figure 6.9 shows the visible and the UV Raman spectra on ceria nanoshapes prepared through the hydrothermal synthesis. Regarding the visible Raman spectra, the intense band centred at  $462\text{ cm}^{-1}$  is due to the vibration mode of Ce-O bond of the cubic fluorite structure and is called  $F_{2g}$  mode. The nanorods exhibit a broader  $F_{2g}$  peak compared to the other samples due to a size-dependent effect. This can be proved considering that the linewidth of the peak increases with the decrease of the particles size. In the considered experiment, indeed, the nanorods exhibit a particle size of 11 nm which is smaller in comparison to 95 and 117 nm calculated for the nanocubes and octahedra, respectively [70], [71].

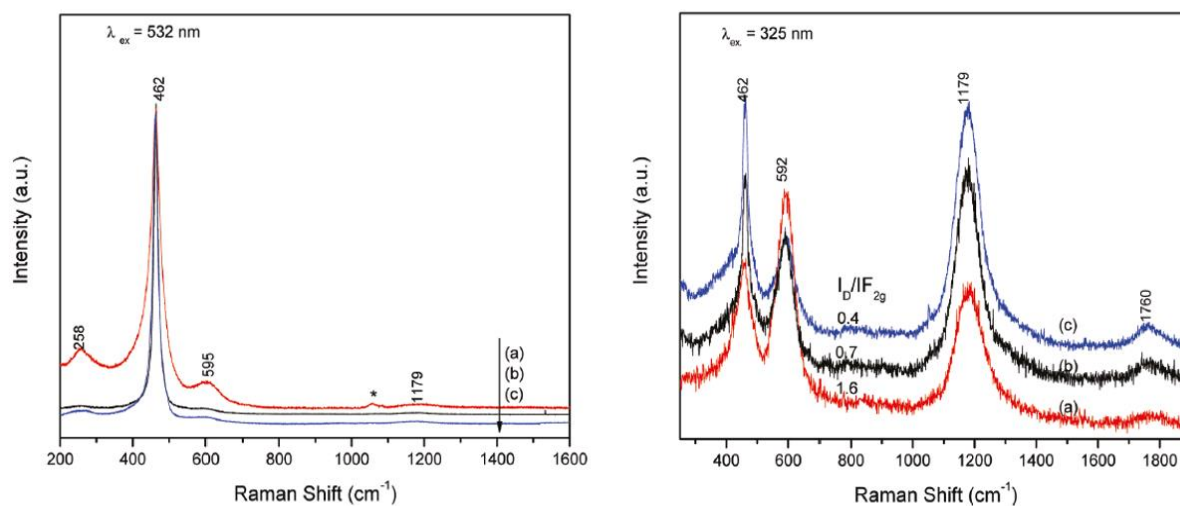


**Figure 6.9:** Visible and UV Raman spectra of nanorods (red lines), nanocubes (black lines) and nano-octahedra (blue lines) adapted from ref. [70]

The UV Raman spectra, instead, is more sensitive to the presence of defects in the lattice structure of ceria due to the enhancement of the D band at  $592\text{ cm}^{-1}$ . This latter is attributed to the Frenkel-type oxygen intrinsic defects present in the samples. In this context, the ratio between the D and the  $F_{2g}$  band intensities ( $I_D/I_{F_{2g}}$ ) is associated to the relative amount of intrinsic defects in the catalysts and, in particular, a high ratio is an indication of a high number of defect sites. Therefore, according to Figure 6.9, nanorods show more defects than nanocubes which, in turn, exhibit more defects than octahedra [70], [72].

The three ceria nanoshapes can differ in terms of catalytic properties, therefore IR spectroscopy is used to determine the different acidic and basic sites and their strength on the different samples prepared with the hydrothermal method. IR spectra in Figure 6.10 represent the interaction between nanocubes, nanorods and octahedra with the probe molecule pyridine. It should be noted that Brønsted acidic sites are not present due to the absence of the characteristic band around  $1540\text{ cm}^{-1}$ , conversely the presence of Lewis sites is evident according to the peaks at  $1600$  and  $1444\text{ cm}^{-1}$ . Furthermore, the blueshift to higher vibrational frequency compared to the peak at  $1582\text{ cm}^{-1}$  of the free pyridine is about the same for the three nanoshapes, therefore the acidic sites on nanocubes, nanorods and octahedra are characterized with no significant difference in terms of strength [62].

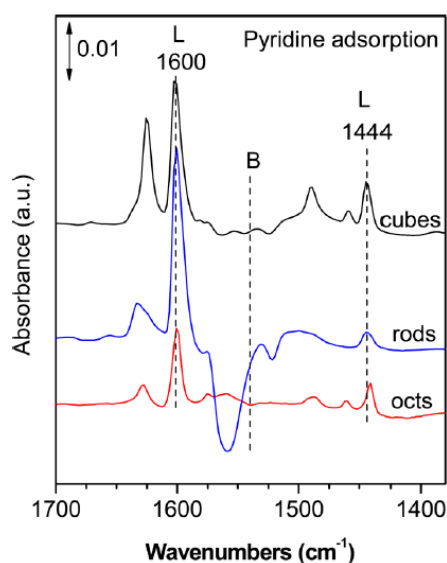


**Figure 6.10:** IR spectra of pyridine adsorption on ceria nanoshapes at room temperature from ref. [62]

Concerning the basic sites characterization, the  $\text{CO}_2$  is used as a probe molecule. The interaction between the ceria surface and the  $\text{CO}_2$  allows the distinction of two types of basic sites: basic hydroxyl groups and basic surface oxygen or Lewis bases. Figure 6.11 shows the IR spectra obtained after the  $\text{CO}_2$  adsorption on the three ceria nanoshapes. Several species are formed on the surfaces. Bicarbonates derive from the interaction between the carbon dioxide and the basic hydroxyl groups and they are present on all three ceria samples. The three negative bands at  $3712$ ,  $3687$  and  $3617\text{ cm}^{-1}$  are assigned to the consumption of surface  $-\text{OH}$  groups during the bicarbonate species formation. Furthermore, the interaction between the  $\text{CO}_2$  and the basic surface oxygen allows the formation of monodentate, bidentate and bridged carbonate species which are present on the three surfaces. Interestingly, bidentate groups dominate on ceria octahedra according to the bands centred at  $1580$  and  $1292\text{ cm}^{-1}$  [62].

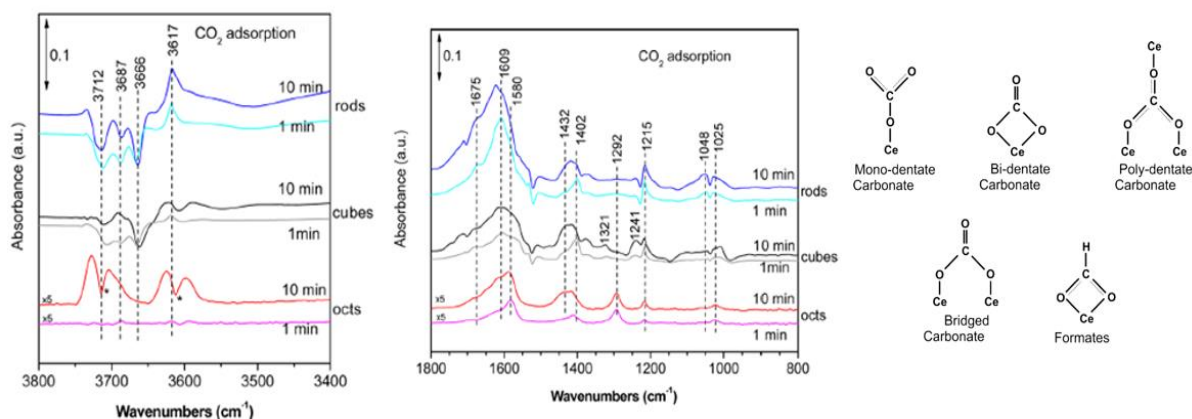


**Figure 6.11:** IR spectra of CO<sub>2</sub> adsorption on ceria nanoshapes at room temperature adapted from ref. [62], [73]

The stability of the different species formed on the ceria surfaces can be studied with a TPD test: a helium flux is sent to the three catalysts for 30 minutes at room temperature. The basic sites on ceria nanorods and nanocubes are more stable than those on the octahedra sample. The IR spectra of rods and cubes do not change during the TPD test, conversely the bands of octahedra spectrum decrease in intensity. Carbonates species disappear from octahedra and their IR intensity decreases in cubes and rods at 150°C. With further increasing temperature, bicarbonates disappear from the nanorods and nanocubes surfaces before the carbonate species; it means that the basicity of hydroxyl groups is weaker compared with that of the surface oxygen [62].

Surface defect sites of ceria nanoshapes, such as Frenkel-type intrinsic defects and the presence of Ce<sup>3+</sup> linked to oxygen vacancies, can be studied using methanol as a probe molecule. As described in Figure 6.12, the methanol adsorption at room temperature allows the formation of three different species on the ceria surface [74]:

- Type I methoxy detected for the C-O stretching around 1110 cm<sup>-1</sup> by IR spectroscopy
- Type II methoxy detected with bands around 1050 cm<sup>-1</sup> by IR spectroscopy
- Type III methoxy detected with bands around 1120 cm<sup>-1</sup> by IR spectroscopy

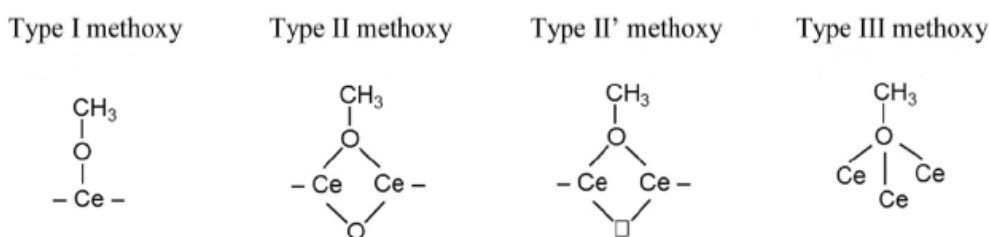


**Figure 6.12:** Different types of methoxy species formed after methanol adsorption at room temperature adapted from ref. [74]

According to the IR spectra in Figure 6.13, type I methoxy species are present on all three ceria surfaces. Conversely, bridging and three-coordinate methoxy groups are observed only on nanorods and nanocubes. As shown above, the Raman spectroscopy performed on the three nanoshapes shows the presence of a higher amount of defect sites in cubes and rods compared to the octahedra sample. Therefore, the absence of type I and II species on the ceria octahedra

after methanol adsorption can be related to the presence of a more compact catalyst, little inclined to form oxygen vacancies. Then, in summary, the distribution of methoxy species, obtained after room temperature  $\text{CH}_3\text{OH}$  adsorption, is dependent on the shape of the ceria nanocrystals as well as the number of defect sites [74].

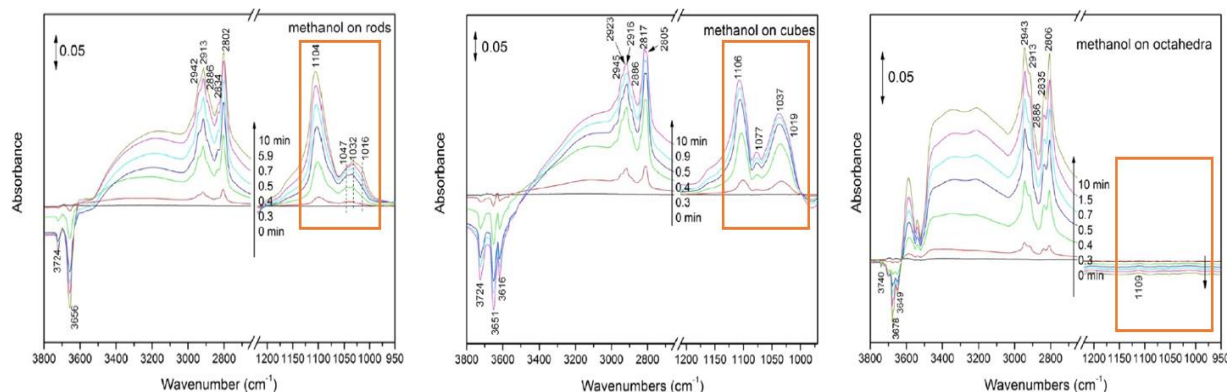


**Figure 6.13:** IR spectra of methanol adsorption on ceria nanoshapes at room temperature adapted from ref. [74]

### 6.3 Catalytic performance of ceria catalysts in oxidation reactions

#### Catalytic performance of ceria catalysts at nanoscale in oxidation reactions - CO oxidation

According to the literature, the ceria nanorods typically show more activity than the other nanoshapes in oxidation reactions due to the higher amount of defect sites in their structure [60], [75]. However, recent studies have proved the better performance of nanocubes for the CO oxidation. In this respect, through the hydrothermal synthesis, it is possible to obtain nanocubes with rounded corners characterized by the exposition of both (100) and (110) surfaces which are responsible for the high catalytic activity [69]. Therefore, according to the results of the TPO test shown in Figure 6.14, nanocubes exhibit a lower  $T_{90\%}$  value compared to nanorods and the samples prepared via SCS have provided poorer performance than the nanostructured catalysts.

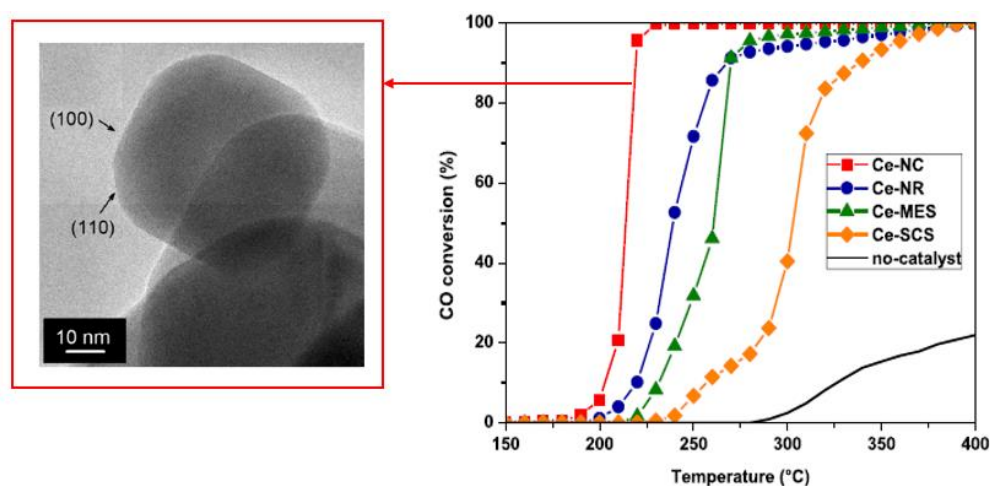


**Figure 6.14:** HRTEM image of ceria nanocubes (on the left) and CO conversion on ceria catalysts (on the right) adapted from ref. [69]

## Catalytic performance of ceria catalysts at nanoscale in oxidation reactions - Soot oxidation

As shown in Figure 6.15, the soot oxidation activity is evaluated with a TPO test using different catalysts prepared through both hydrothermal and SCS procedures. The catalytic performance is evaluated in “tight” and “loose” contact conditions, therefore, the experiments are performed with intimate and weak interactions between the catalysts and the soot. The best outcomes are observed for ceria nanocubes and, in particular, Ce-NC/ZSM-5 sample has proved the highest performance in terms of  $T_{\text{peak}}$  value, which is the required temperature to reach 100% soot conversion [76].

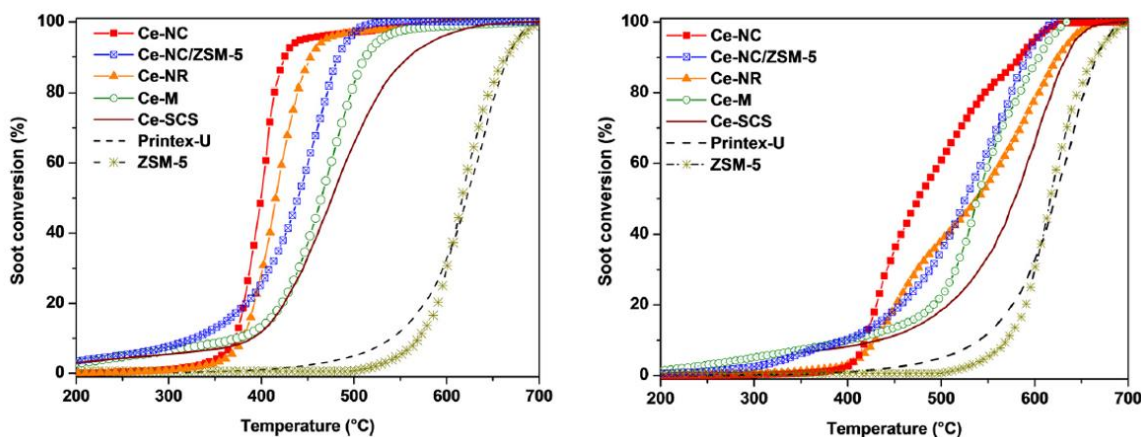


**Figure 6.15:** Soot conversion on ceria catalysts in “tight” (on the left) and “loose” contact conditions adapted from ref. [76]

Similar results have been observed in other studies. Interestingly, there is evidence that the calcination temperature of ceria nanocubes synthesized through hydrothermal synthesis can change their morphology. According to an HRTEM images analysis, nanocubes treated at low temperature show well-defined corners with (100)-type predominant planes. A more curved structure, instead, is formed by enhancing the thermal treatment. The formation of (110) planes also occurs, as they arise from the truncation of edges and corners of the cube-like structure, as illustrated in Figure 6.16. This modified cubic structure is the most active in the oxidation reactions due to the presence of different intrinsic active surfaces [77]. Therefore, it can be concluded that soot oxidation is a surface-dependent reaction.

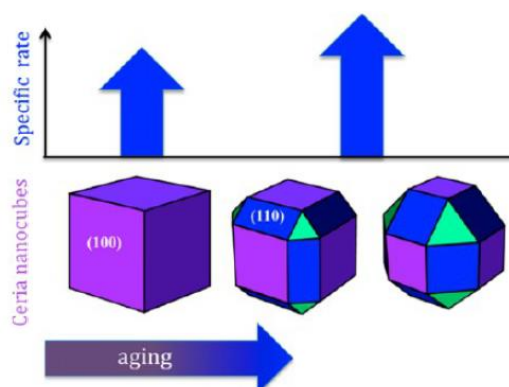


**Figure 6.16:** Morphological changes of ceria nanocubes increasing the calcination temperature adapted from ref. [77]

Considering instead the SCS procedure, the choice of different solvents and different fuels can contribute to the soot oxidation in a more or less meaningful way. In this regard, ceria nanoparticles prepared with glycine as a fuel and acetone as a solvent show the lowest  $T_{50\%}$  value for this oxidation reaction. The coupling of these substances, indeed, exhibits the higher (100)/(111) and (110)/(111) ratios compared to the other [67]. Therefore, the presence of these intrinsically active surfaces promotes the soot oxidation at a lower temperature. Furthermore, the activity of glycine-acetone catalysts prepared via the SCS method is maintained also in subsequent work cycles, as demonstrated in Figure 6.17.

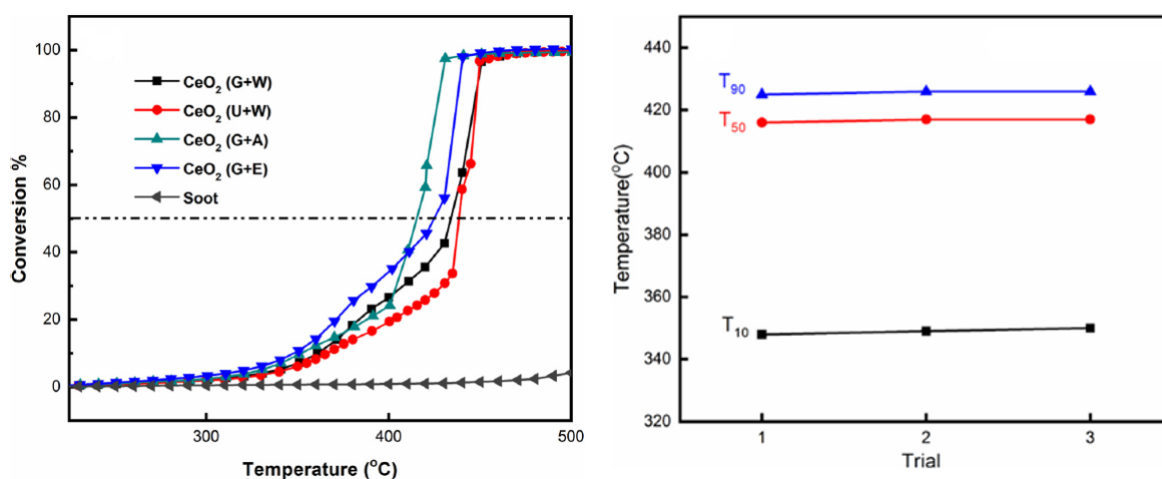


**Figure 6.17:** Soot oxidation on CeO<sub>2</sub> catalysts prepared via the SCS method using different fuels and solvents (on the left) and the results repeatability in subsequent cycles using glycine as a fuel and acetone as a solvent (on the right) adapted from ref. [67]

Catalytic performance of ceria catalysts at nanoscale in oxidation reactions - VOCs oxidation, total oxidation of polycyclic aromatic hydrocarbons

An important aspect of the oxidation of the volatile organic compounds is the reaction selectivity, which helps avoid the generation of toxic by-products. In this context, the catalytic oxidation of naphthalene is performed on ceria catalysts synthesized through the SCS procedure, using ethylene glycol as a fuel in different ratios with the ceria precursors. It has been observed that modifying the quantity of fuel, the activity and the selectivity of the reaction significantly change. At low temperature, both activity and selectivity increase with a high concentration of ethylene glycol, as shown in Figure 6.18.

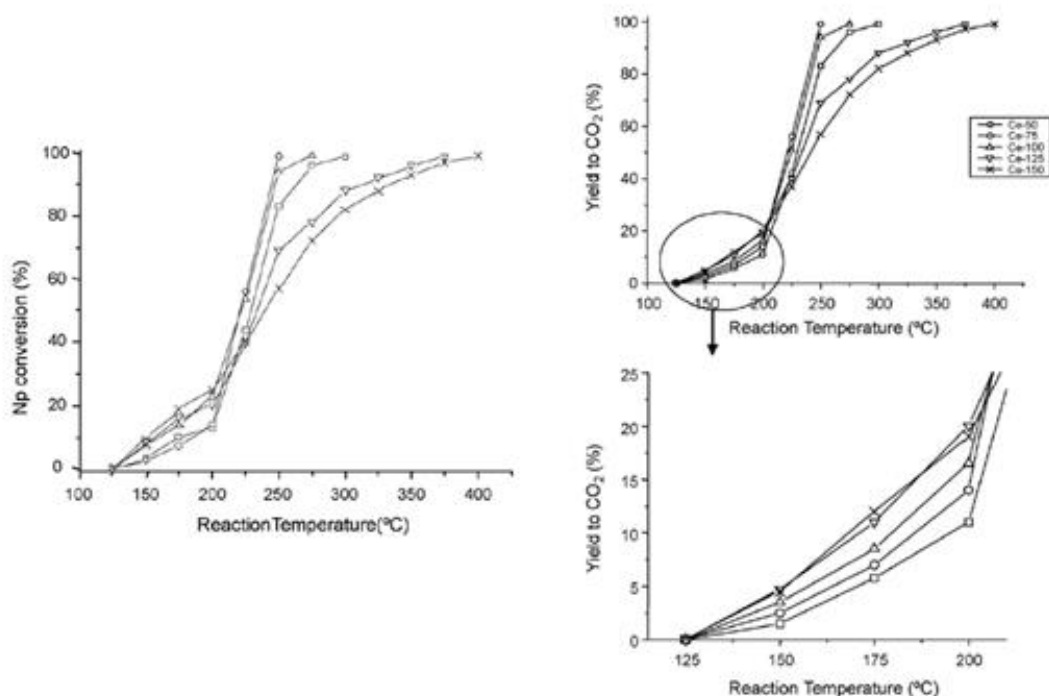


**Figure 6.18:** Naphthalene conversion on ceria catalysts and CO<sub>2</sub> production with different EG/Ce molar ratios adapted from ref. [78]

However, by increasing the temperature, the optimal performance in the naphthalene oxidation and the CO<sub>2</sub> production is detected with an EG/Ce molar ratio of 0.75 [78]. Therefore, the combination of high activity and high CO<sub>2</sub> selectivity makes ceria catalysts good systems for the naphthalene oxidation reaction.



## 7. Modified ceria catalysts

The incorporation of foreign metallic dopants into the lattice structure of ceria catalysts is one of the most powerful techniques to improve its catalytic properties. Mixed oxides have been achieved with rare earth elements, in particular using praseodymium and terbium; as for the transition metals, ceria allows the formation of solid solutions with  $ZrO_2$ ,  $CuO$ ,  $MnO_x$  and many other oxides. It is known that the modified ceria catalysts show different structural and energetic properties compared to pure ceria. Moreover, the ceria oxygen storage capacity is enhanced with the insertion of other elements due to the creation of defect sites, especially oxygen vacancies. In this context, praseodymium and terbium coexist in two different oxidation states ( $3+$  and  $4+$ ) both in their pure oxides and in the solid solution with ceria. Therefore, the use of these species significantly improves the oxygen mobility and the redox properties of the system. To sum up, the structural and redox modification of the ceria-based catalysts allows a better activity in different catalytic fields, with particular regard for the total oxidation reactions of soot, CO and VOCs [79].

### 7.1 Nanostructured ceria-praseodymia catalysts

#### Nanostructured Praseodymium Oxide - General properties and catalyst characterization

The praseodymium oxide has shown great importance among the rare-earth oxides. Several stoichiometrically defined oxides can be formed with different oxygen content.  $Pr_nO_{2n-2}$  with  $n=4, 7, 9, 10, 11, 12, \infty$  is their general formula and the limit cases are  $Pr_2O_3$  and  $PrO_2$ . In this context, the most stable praseodymium oxide at room temperature is  $Pr_6O_{11}$ . It can be seen as an oxygen-deficient modification of cubic fluorite-like  $PrO_2$  [80]. In its structure,  $Pr_6O_{11}$  contains cations with different valence states:  $Pr^{4+}$  and  $Pr^{3+}$ . The quick transition between these two oxidation states makes the praseodymia the catalyst with higher oxygen mobility among the lanthanide oxides [81].

The praseodymium oxide can be prepared with both traditional techniques and sophisticated procedures. The first include the calcination of the nitrate and the sol-gel method in which the gel formation occurs through the addition of propylene oxide. The advanced techniques, instead, include the Pechini approach - based on the use of ethylene glycol, citric acid and ethylenediamine - and the citrate method in which praseodymium nitrate is treated with different quantities of citric acid dissolved in ethanol. All these procedures lead to the formation of similar samples both from a chemical and a structure point of view [80], [82]. According to the TEM images of praseodymia samples in Figure 7.1, agglomerated structures are formed starting from small crystallites with size in the range between 20 and 70 nm.

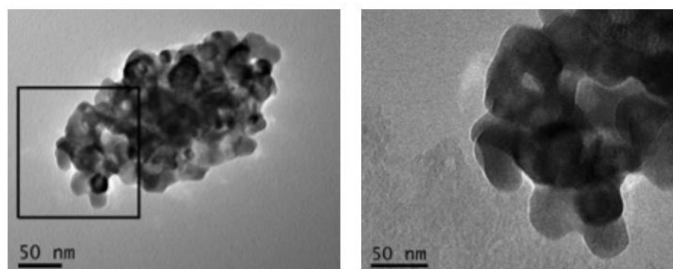


**Figure 7.1:** TEM images of praseodymia samples adapted from ref. [82]

In this context, the XRD analysis shows the obtainment of praseodymium oxide ( $\text{Pr}_6\text{O}_{11}$ ) with cubic fluorite-like structure, working with a calcination temperature between 300 and 540°C. The X-ray diffractograms of the different samples are illustrated in Figure 7.2. The surface area of the obtained samples is between 5 and 28  $\text{m}^2 \text{g}^{-1}$  [80].

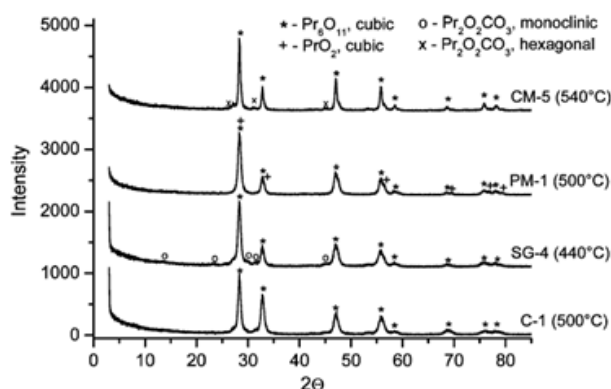


**Figure 7.2:** XDR pattern of samples obtained with Citrate Method (CM), Pechini Method (PM), So-Gel Method (SG) and calcination of the salt adapted from ref. [80]

The hydrothermal method is an alternative procedure to obtain the nanostructured praseodymium oxide [83]. In this regard, it is possible to obtain the precipitation of  $\text{Pr}(\text{OH})_3$  starting from the treatment of praseodymium precursors such as nitrates or chlorides, with a basic solution. The suspension is aged at 100-120°C for several hours and then calcinated at high temperature. The hydrothermal method allows the formation of praseodymium oxide in the  $\text{Pr}_6\text{O}_{11}$  form with a rod-like morphology.

Figure 7.3 shows the FT-IR spectra of  $\text{Pr}(\text{OH})_3$  as well as praseodymium oxides obtained with a temperature treatment at 550 and 900°C. The band at  $3607 \text{ cm}^{-1}$  is attributed to the stretching of the O-H group and the corresponding bending vibration falls to  $674 \text{ cm}^{-1}$ . These peaks decrease in intensity, treated the praseodymium hydroxide at high temperature. Furthermore, the bands at 1394 and  $1495 \text{ cm}^{-1}$  are assigned to the symmetric and asymmetric stretching of the  $\text{COO}^-$  species [83].

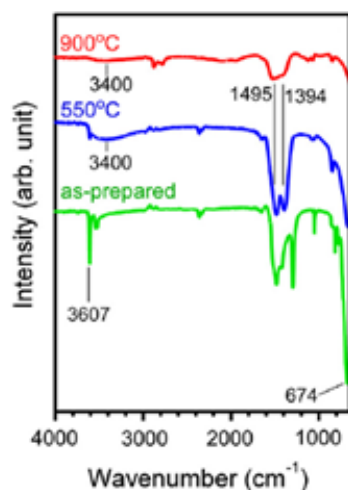


**Figure 7.3:** FT-IR spectra of  $\text{Pr}(\text{OH})_3$  and praseodymium oxides adapted from ref. [83]

Praseodymia nanoparticles can also be obtained throughout an innovative hydrothermal process which consists of three steps [84]. Firstly, the precipitation of  $\text{Pr}(\text{OH})_3$  is performed starting from a praseodymium salt dissolved in a basic solution, then the obtained mixture is repeatedly washed with deionized water, as in the normal technique. Finally, the suspension is aged at room temperature for three days and calcinated at  $600^\circ\text{C}$  for a few minutes. The modified-hydrothermal method allows the formation of praseodymia nanorods as in the common hydrothermal technique but using lighter operative conditions. Figure 7.4 reports the TEM images during the different procedure steps:

- a: washed  $\text{Pr}(\text{OH})_3$  consists of nanoparticles aggregates with an irregular shape
- b:  $\text{Pr}(\text{OH})_3$  is presented as crystalline nanorods after three days of aging
- c: praseodymium oxide ( $\text{Pr}_6\text{O}_{11}$ ) obtained after the calcination process is constituted by nanorods with size between 10 and 170 nm in length and 5- 25 nm in width

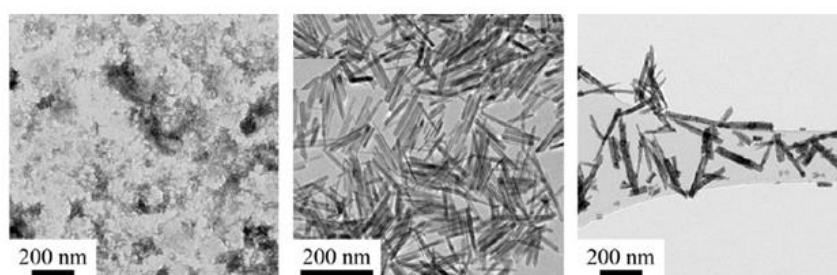


**Figure 7.4:** TEM images of fresh  $\text{Pr}(\text{OH})_3$ ,  $\text{Pr}(\text{OH})_3$  after three days of aging and praseodymium oxide  $\text{Pr}_6\text{O}_{11}$  adapted from ref. [84]

#### Nanostructured Praseodymium Oxide - Catalytic performance in CO and $\text{CH}_4$ oxidation

Figure 7.5 shows a temperature-programmed oxidation test (TPO) performed in a laboratory reactor in a continuous flow containing a mixture of CO and oxygen in argon[80]. Catalysts prepared with the citrate method (CM), the Pechini procedure (PM), the sol-gel technique (SG) and with the calcination of the salt (C) show approximately the same behaviour in the oxidation of CO. The carbon monoxide oxidation starts at  $300\text{-}350^\circ\text{C}$  and achieves 100% conversion by increasing the temperature up to  $600^\circ\text{C}$ .

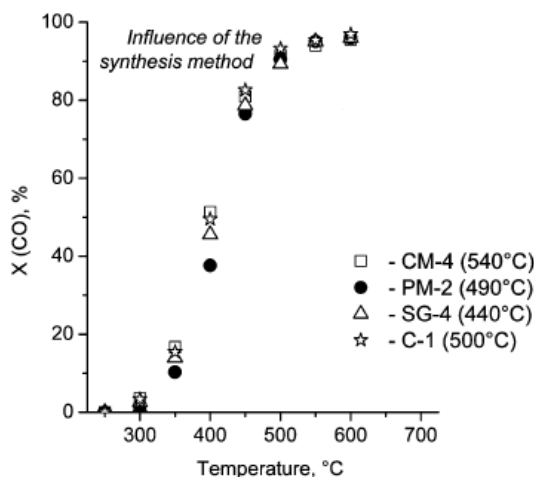


**Figure 7.5:** CO oxidation over praseodymia catalysts adapted from ref. [80]

Regarding instead the methane oxidation, a TPO test is performed in a continuous-flow laboratory reactor using the gaseous mixtures with the composition described in Table 3 [82].

**Table 7.1:** Gas mixture used during the catalytic tests adapted from ref. [82]

	CH <sub>4</sub> /O <sub>2</sub> ratio	CH <sub>4</sub> (vol.%)	CO (vol.%)	O <sub>2</sub> (vol.%)	Ar (vol.%)
CH <sub>4</sub> oxidation (□)	ca. 1:2	2.9	-	5.0	92.1
CH <sub>4</sub> oxidation (Δ)	ca. 2:1	4.6	-	2.3	93.1
CO oxidation	-	-	3.3	1.7	95.0

Taking into account that the oxidation of methane can occur according to Equations (7.1), (7.2), (7.3) and (7.4), the reaction is performed with a CH<sub>4</sub>/O<sub>2</sub> ratio equal to 1:2 and 2:1.



Only the formation of CO<sub>2</sub> has been detected at the reactor outlet, also performing a different experiment with a methane-to-oxygen ratio equal to 1:1 [82]. The praseodymium oxide is, therefore, a catalyst with good performance in the total oxidation of methane and not for partial oxidation reactions. However, the methane oxidation starts at about 400°C and a good conversion is only reached working at high temperature, as illustrated in Figure 7.6. Regarding the CO oxidation the results are in agreement with the previous analysis.

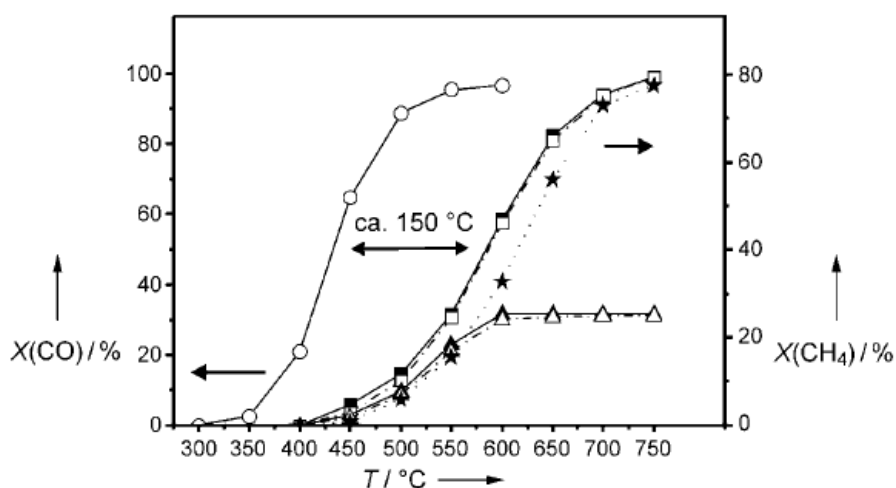


**Figure 7.6:** CO and CH<sub>4</sub> conversions on praseodymia catalysts using a CH<sub>4</sub> to O<sub>2</sub> ratio of 1:2 (□) and 2:1 (Δ) from ref. [82]

### 7.1.1 General properties and catalyst characterization of ceria-praseodymia catalysts

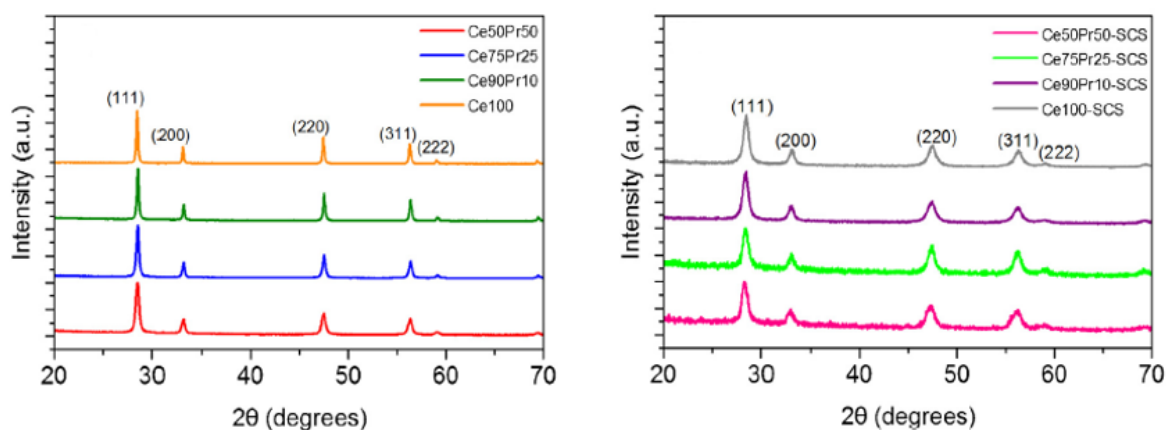
The incorporation of praseodymium in the ceria lattice has been widely studied in recent years due to its positive performance in soot and carbon monoxide oxidation reactions. The insertion of Pr dopants generates the formation of structural defects which enhance the catalytic properties of the ceria catalysts. First of all, the OSC capacity is improved because of the presence of the  $\text{Pr}^{3+}/\text{Pr}^{4+}$  and the  $\text{Ce}^{3+}/\text{Ce}^{4+}$  pairs which increase the oxygen mobility and therefore the overall amount of removable oxygen from both the surface and the bulk of the catalyst [85]. Last but not least, praseodymium is more reducible than cerium, allowing a formation of a higher number of oxygen vacancies compared to the ceria samples [86].

In this section the performance of nanostructured ceria-praseodymia synthesized through three different procedures has been studied. In this regard, hydrothermal, solution combustion synthesis (SCS) and co-precipitation methods allow the preparation of samples with a different composition according to the  $\text{Ce}_x\text{Pr}_{1-x}\text{O}_{2-\delta}$  formula. The compositions of the above-mentioned preparation systems are described in Table 7.2.

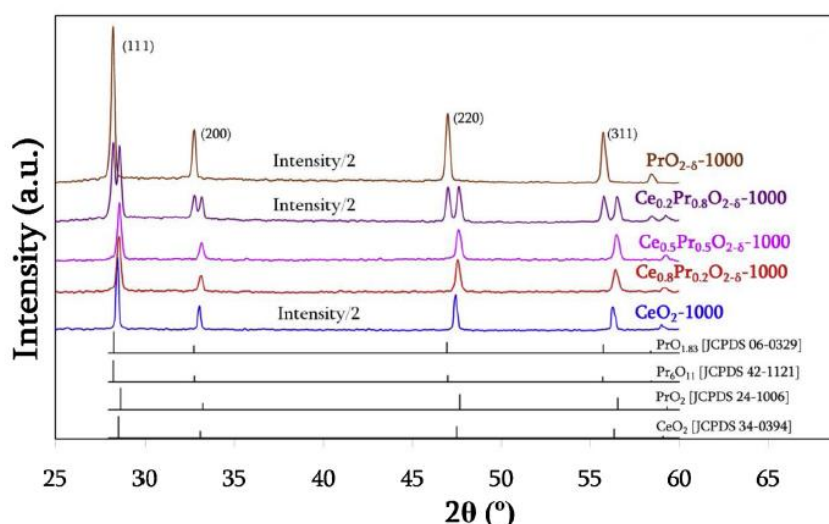
**Table 7.2:** Composition of the studied samples adapted from ref. [87], [88]

	Ce (%)	Pr (%)
Hydrothermal method - calcination temperature 550°C [87]	100	0
	90	10
	75	25
	50	50
Solution combustion synthesis (SCS) [87]	100	0
	90	10
	75	25
	50	50
Co-precipitation method - calcination temperature 1000°C[88]	100	0
	80	20
	50	50
	20	80
	0	100

The surface area ranges from 6 to 20  $\text{m}^2 \text{g}^{-1}$  and 14 to 43  $\text{m}^2 \text{g}^{-1}$  for the samples prepared via hydrothermal and SCS procedures, respectively [87]. The XRD analysis of the different samples is reported in Figure 7.7 and 7.8. As shown above, the presence of (111), (200), (311) and (222) planes confirms the fluorite structure of all the catalysts [68]. The catalysts synthesized by the hydrothermal and the SCS method allow the formation of a solid solution between cerium and praseodymium due to their very similar ionic radius. However, the solid solution formation does not occur if the praseodymium content is continuously increased, as demonstrated by the phase segregation in the  $\text{Ce}_{0.2}\text{Pr}_{0.8}\text{O}_{2-\delta}$  sample. As a matter of fact, the XRD analysis of the sample shows double peaks around 33, 47 and 56°.

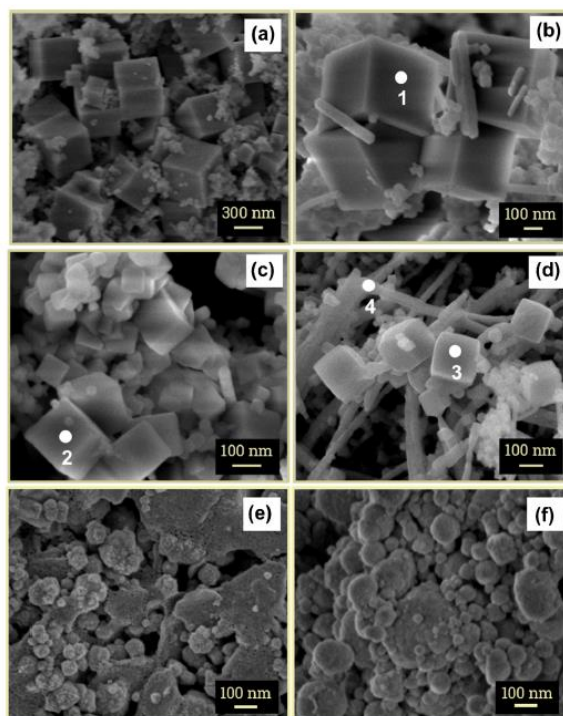


**Figure 7.7:** X-ray diffractograms of  $Ce_xPr_{1-x}O_{2-\delta}$  obtained via hydrothermal (left image) and SCS procedures (right image) adapted from ref. [87]



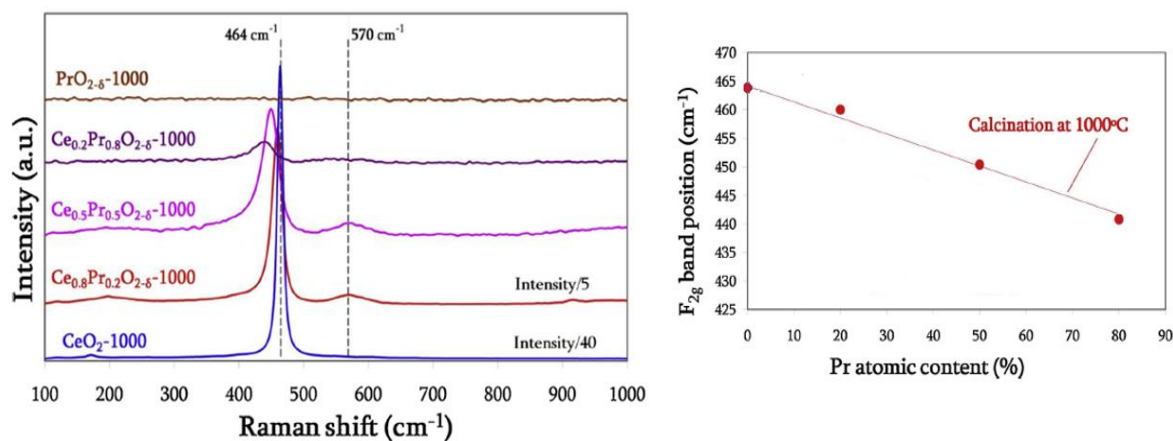
**Figure 7.8:** X-ray diffractograms of  $Ce_xPr_{1-x}O_{2-\delta}$  obtained via the co-precipitation procedure adapted from ref. [88]

Figure 7.9 shows the SEM images of the samples obtained via hydrothermal (a, b, c, d) and SCS procedures (e, f) [87]. In this regard, the pure ceria obtained through the hydrothermal synthesis is characterized by a nanocube morphology. Considering that this sample is obtained with an aging temperature of  $180^\circ\text{C}$ , this result is in accordance with the previous discussion on the preparation methods of ceria catalysts (paragraph 6.1.2). Nanorods begin to appear on the sides of nanocubes by increasing the praseodymium content and they dominate in the sample containing half praseodymium and half cerium, which is the catalyst with the highest Pr amount. Therefore, the crystal orientation of the Ce50-Pr50 is controlled by the praseodymium. This result is consistent with the previous treatment, in which the nanostructured praseodymium oxide mostly presents the form of nanorods (paragraph 7.1.1). Conversely, the catalysts prepared via SCS exhibit a porous sponge-like structure due to the release of a high quantity of gases in a short time during the preparation method.



**Figure 7.9:** FE-SEM images of Ce100 (a), Ce90Pr10 (b), Ce75Pr25 (c), Ce50Pr50 (d) obtained via the hydrothermal method and Ce50Pr50 (e) and Ce90Pr10 (f) synthesized through SCS procedure from ref. [87]

The Raman spectra of catalysts prepared via the co-precipitation method are shown in Figure 7.10. Interestingly, the  $F_{2g}$  band at  $464\text{ cm}^{-1}$  decreases its intensity, becomes wider and wider and exhibits a shift to low wavenumbers by increasing the praseodymium content. The intensity decrease of the  $F_{2g}$  bands is attributed to the loss of structure symmetry due to the introduction of praseodymium cations into the ceria lattice. Furthermore,  $\text{Pr}^{4+}$  ions are more reducible compared to  $\text{Ce}^{4+}$ , therefore the peaks shift to lower wavenumbers is attributed to the high amount of  $\text{Pr}^{3+}$  species. In this regard, the M-O bond in the ceria-praseodymia structure is longer than in the pure ceria because the  $\text{Pr}^{3+}$  ionic radius is lower than that of  $\text{Ce}^{3+}$ . The system requires, in this way, less energy to vibrate [88].



**Figure 7.10:** Raman spectra of the ceria-praseodymia catalyst obtained via the co-precipitation method adapted from ref. [88]

## 7.1.2 Catalytic performance of ceria-praseodymia catalysts in oxidation reactions

### Catalytic performance of ceria-praseodymia catalysts in oxidation reactions – NO oxidation

Figure 7.11 shows temperature-programmed NO oxidation performed in a fixed-bed reactor using 500 ppm of NO in a nitrogen atmosphere in the presence of oxygen [88], [89]. The NO<sub>2</sub> production rises with increasing the praseodymium content and, simultaneously, it is possible to notice a curves shift to low temperature. It is quite clear that the praseodymium oxide is more active compared to the cerium one in the catalytic oxidation of NO.

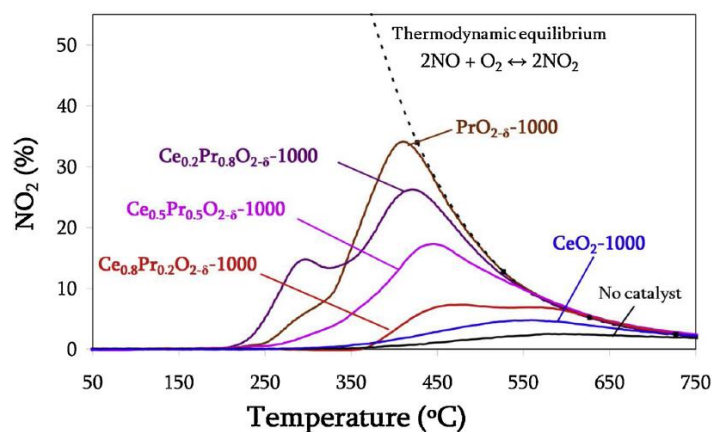


**Figure 7.11:** NO oxidation on Ce<sub>x</sub>Pr<sub>1-x</sub>O<sub>2-δ</sub> samples prepared via the co-precipitation method adapted from ref. [88]

### Catalytic performance of ceria-praseodymia catalysts in oxidation reactions – Soot oxidation

A TPO analysis is performed on the samples synthesized through both hydrothermal and SCS procedures in “tight” conditions - to test the intrinsic catalytic properties of the samples - and in “loose” interactions - to study the real performance of the catalysts in a diesel particulate filter. The samples with “tight” contact show higher activity than the other due to the strong interaction between the catalyst and the soot. As a matter of fact, the oxidation reaction under “tight” conditions starts at 300-350 °C and the soot conversion rapidly rises by increasing the temperature, as shown in Figure 7.12. The catalyst with formula Pr<sub>0.5</sub>Ce<sub>0.5</sub>O<sub>2-δ</sub> prepared via hydrothermal synthesis is the most performing sample in the soot oxidation [87]. Generally, the catalysts obtained by hydrothermal synthesis are more active in the soot oxidation reaction than that prepared via the SCS method due to their well-defined nanostructure with the exposition of (100) and (110) active surfaces.

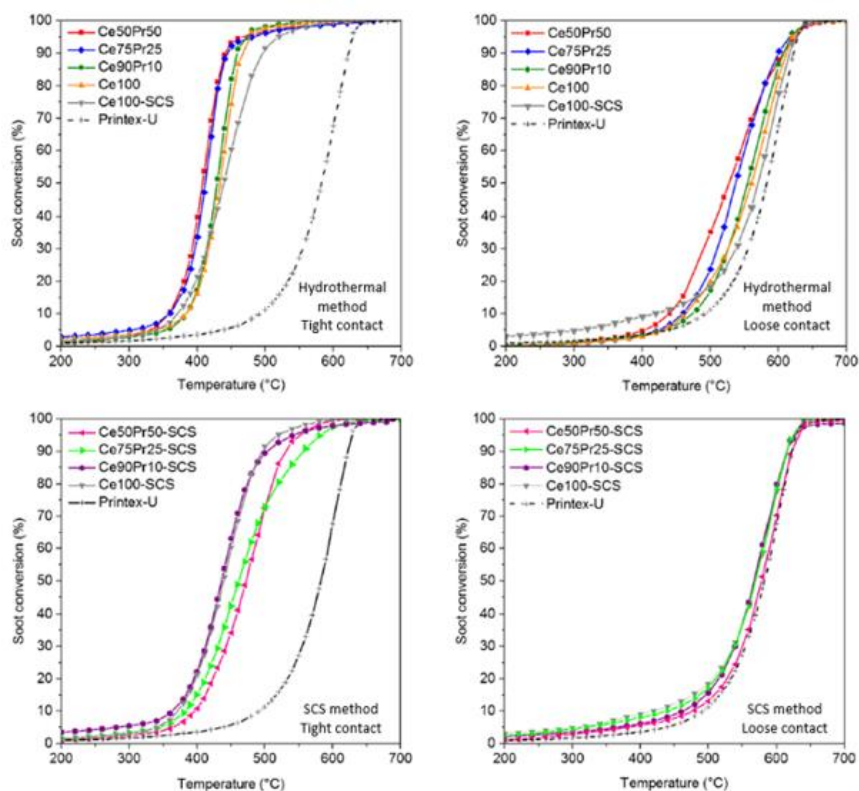


**Figure 7.12:** Soot oxidation on  $Ce_xPr_{1-x}O_{2-\delta}$  samples prepared via hydrothermal and SCS methods under “tight” and “loose” contact adapted from ref. [87]

The equimolar ceria-praseodymia catalyst has been proved to have good catalytic activity in CO, ethylene, propylene and soot oxidations also in low-oxygen conditions. The catalyst, indeed, can easily release the lattice oxygen during the reactions maintaining a stable fluorite structure. Furthermore, a good  $CO_2$  selectivity in the reaction products has been observed [90].

It should be considered that in the exhaust gas of diesel engines a quantity between 100 and 700 ppm of NO is always present and it can be partially converted into  $NO_2$  in the DOC system. Considering that, as explained above, the  $NO_2$  is a more performing oxidizing agent than the oxygen, it can be used as an active species in the soot oxidation. Figure 7.13 shows the conversion curves of soot with and without the presence of  $NO_x$  molecules on the catalysts prepared via co-precipitation method in “loose” contact conditions [88]. The graphs are not that different probably for the weak interaction between the catalyst and the soot. In any case, the sample with a higher amount of cerium in the structure exhibits a lower catalytic activity in the oxidation reaction than the others. This can be explained by keeping in mind that the particulate is oxidized by  $NO_2$  with the formation of carbon dioxide and NO. Once formed, the latter can be easily and quickly converted into  $NO_2$  due to the presence of praseodymium, which has shown good activity in NO oxidation (Figure 7.11). Therefore, compared to the pure ceria, the catalysts with a high amount of praseodymium in the lattice structure show greater catalytic activity in the soot oxidation in presence of  $NO_x$  molecules.

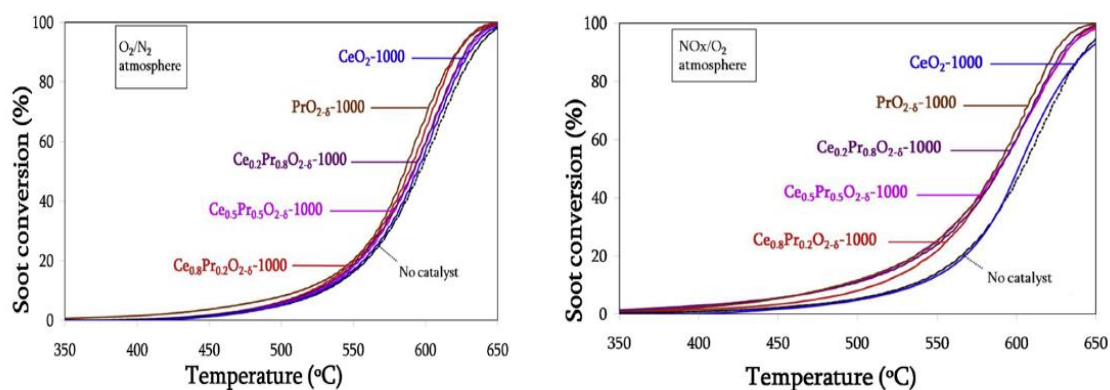


**Figure 7.13:** Soot oxidation on  $Ce_xPr_{1-x}O_{2-\delta}$  samples prepared via the co-precipitation method under  $NO_x/O_2$  and  $O_2/N_2$  atmospheres in “loose” conditions adapted from ref. [88]

Other studies have shown consistent results with the previous explanations. In particular, it has been demonstrated that the presence of the praseodymium in the lattice structure allows the NO conversion to  $NO_2$  and, simultaneously, increases the  $NO_2$  adsorption on the catalytic surface [91]. In this regard, Table 7.3 below shows the temperature necessary to reach 10%, 50% and 90% of soot conversion on ceria and equimolar ceria-praseodymia catalysts prepared though the hydrothermal procedure, with and without  $NO_x$  species.

**Table 7.3:**  $T_{10\%}$ ,  $T_{50\%}$  and  $T_{90\%}$  for the soot oxidation reaction in the presence and the absence of  $NO_x$  adapted from ref. [91]

Sample	$T_{10\%}$ (°C)	$T_{50\%}$ (°C)	$T_{90\%}$ (°C)
Soot oxidation in the absence of $NO_x$			
Ceria nanoparticles	494	579	637
Ce50Pr50 nanoparticles	441	527	609
Soot oxidation in the presence of $NO_x$			
Ceria nanoparticles	446	531	580
Ce50Pr50 nanoparticles	391	463	516

### Catalytic performance of ceria-praseodymia catalysts in oxidation reactions – CO and VOCs oxidation

$Ce_xPr_{1-x}O_{2-\delta}$  catalysts prepared with a different method than those described above have been tested for VOCs and CO oxidation [92]. In this regard, the sample are synthesized using the sol-gel method and, as illustrated in Figure 7.14, the  $T_{90\%}$  value for the CO,  $CH_3OH$  and  $CH_4$  is plotted as a function of the Ce/(Ce+Pr) mole ratio obtaining the following results:

- The minimum  $T_{90\%}$  value for the CO oxidation is obtained with a Ce/(Ce+Pr) ratio equal to 0.9
- The minimum  $T_{90\%}$  value for the  $CH_3OH$  oxidation is obtained with a Ce/(Ce+Pr) ratio equal to 0.9

- The  $T_{90\%}$  value for methane is higher than that of CO and CH<sub>3</sub>OH oxidations. In particular, the minimum temperature value to reach the 90% of conversion is 600°C with a Ce/(Ce+Pr) equal to 0.5

The presence of overlapping diffraction peaks in XRD analysis when the x value is between 0.3 and 0.7 should be considered. Both CeO<sub>2</sub> and Pr<sub>6</sub>O<sub>11</sub> phases coexist in the Ce<sub>x</sub>Pr<sub>1-x</sub>O<sub>2-δ</sub> samples causing a decrease in their catalytic activity. A solid solution system is observed only with an x value greater than 0.8. In this context, the CO and CH<sub>3</sub>OH oxidation is inhibited due to the formation of the two phases. As for the methane oxidation, the molecule is difficult to oxidize due to its high stability. Moreover, the formation of water can poison the oxygen vacancies slowing down the oxygen mobility property of the catalyst.

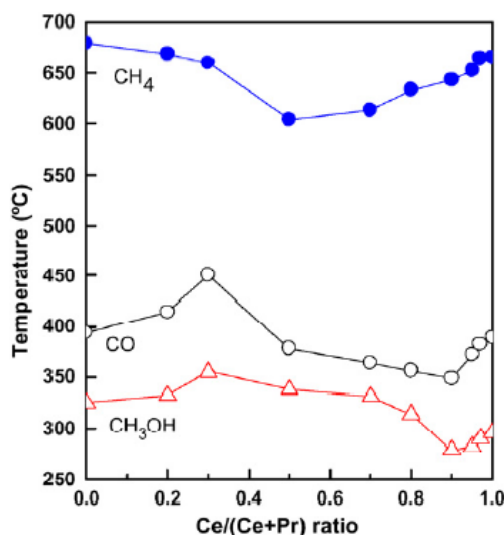
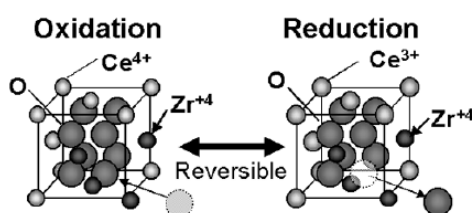


**Figure 7.14:** Relationship between  $T_{90\%}$  and the Ce/(Ce+Pr) ratio for CH<sub>4</sub>, CO and CH<sub>3</sub>OH oxidation from ref. [92]

## 7.2 Nanostructured ceria-praseodymia-zirconia catalysts

### 7.2.1 General properties and catalyst characterization of ceria-praseodymia-zirconia catalysts

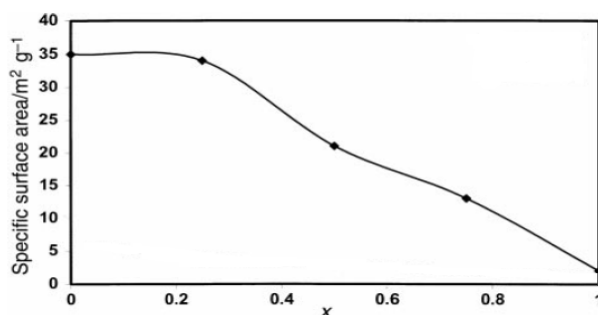
Other modified ceria systems have been tested in recent years. Ceria-zirconia catalysts, in particular, have begun to be studied by several research groups for the carbon monoxide, soot and VOCs oxidation. In this regard, the insertion of non-reducible zirconium cations into the lattice structure of ceria improves its catalytic proprieties due to the formation of defect sites, especially oxygen vacancies. Furthermore, the system appears much more stable from a thermal standpoint [93]. The ceria-zirconia catalysts have also shown better structural stability compared to the ceria samples, as demonstrated in Figure 7.15. During the oxygen release, indeed, the volume of the system increases due to the change of cerium oxidation state from  $\text{Ce}^{4+}$  to  $\text{Ce}^{3+}$ . The presence of zirconium ions in the catalyst lattice allows the reduction of the structural stress caused by the redox transformation, considering that the  $\text{Zr}^{4+}$  ions are smaller compared to the  $\text{Ce}^{4+}$  and  $\text{Ce}^{3+}$  species.



**Figure 7.15:**  $\text{Ce}^{4+}/\text{Ce}^{3+}$  redox transformation in the presence of zirconium ions from ref. [58]

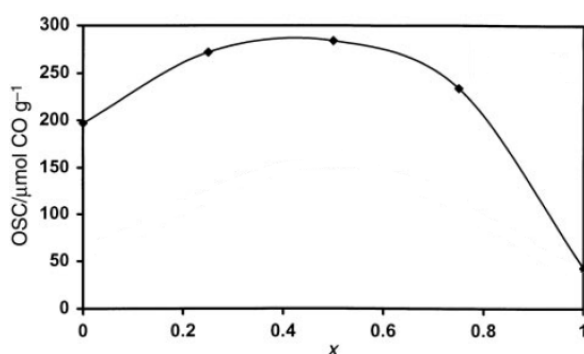
The combination of the good redox properties of the praseodymium and the thermal and mechanical stability features of the zirconium in the ceria samples allows the formation of a high-performance catalyst for the oxidation reactions.

The features of  $\text{Zr}_{0.1}(\text{Ce}_{1-x}\text{Pr}_x)_{0.9}\text{O}_2$  mixed oxides, synthesized by sol-gel procedure, are used to study the effects of the praseodymium and zirconium incorporation into the ceria lattice. In this regard, the sol-gel method allows the obtainment of more structurally homogeneous materials with a controlled composition compared to the co-precipitation procedure. The X-Ray diffraction analysis has shown that a solid solution is achievable only for  $x$  values ranging from 0 to 0.75. Moreover, the introduction of the praseodymium cations causes a lattice contraction due to its smaller ionic radius. The BET surface area of the different catalysts, instead, is shown in Figure 7.16 [94]. The specific surface area decreases by increasing the praseodymium content. A particularly net reduction is observed for  $x$  values greater than 0.75 probably due to the presence of  $\text{Pr}_6\text{O}_{11}$  domains segregated into the structure.



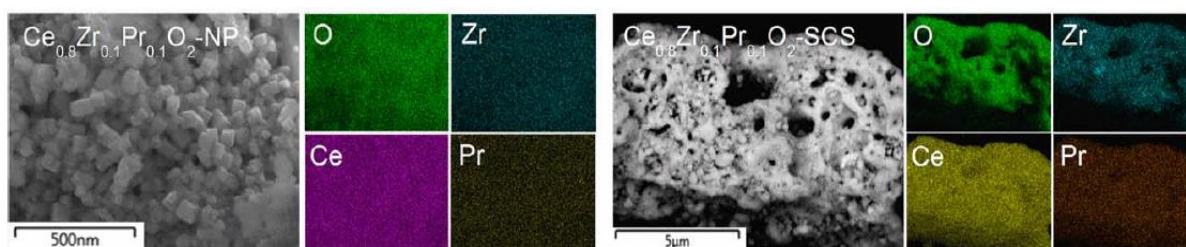
**Figure 7.16:** Specific surface area of  $\text{Zr}_{0.1}(\text{Ce}_{1-x}\text{Pr}_x)_{0.90}\text{O}_2$  mixed oxides adapted from ref. [94]

The oxygen storage capacity has been evaluated measuring the CO consumption in alternate O<sub>2</sub> and CO pulses to simulate the “lean” and “rich” conditions present in an Otto engine. The experiment has been performed at atmospheric pressure with a working temperature of 400°C. Therefore, more specifically, in absence of oxygen, the oxidation process occurs due to the reaction between the CO and the lattice oxygen with the formation of carbon dioxide and oxygen vacancies, in agreement with the Mars van Krevelen mechanism. In the second part of the experiment, the oxygen uptake to obtain a complete re-oxidation of the catalyst is a good estimation of the OSC capacity. In this regard, as shown in Figure 7.17, the maximum value of the oxygen storage capacity has been achieved testing the Zr<sub>0.1</sub>(Ce<sub>0.5</sub>Pr<sub>0.5</sub>)<sub>0.9</sub>O<sub>2</sub> sample [94]. This could explain the higher catalytic activity of equimolar ceria-praseodymia catalysts in CO and soot oxidation compared to the other compositions (see section 7.1.3).



**Figure 7.17:** OSC capacity of Zr<sub>0.1</sub>(Ce<sub>1-x</sub>Pr<sub>x</sub>)<sub>0.90</sub>O<sub>2</sub> mixed oxides adapted from ref. [94]

Ceria-zirconia-praseodymia catalysts can also be obtained through hydrothermal and solid combustion synthesis procedures. In this context, the Ce<sub>0.8</sub>Zr<sub>0.1</sub>Pr<sub>0.1</sub>O<sub>2</sub> sample has been characterized to obtain an even more efficient system for soot and CO oxidation reactions. Firstly, the XRD analysis does not show additional peaks due to the presence of segregated praseodymium and zirconium oxides, therefore, the formation of a solid solution occurs. Then, according to the FESEM images, the sample synthesized via the hydrothermal method exhibits a well-defined nanostructure predominantly constituted by nanocubes, whereas the sample obtained through the SCS method is characterized by the typical spongy porous structure. The specific surface areas are small, in particular, 2-9 m<sup>2</sup> g<sup>-1</sup> for nanostructured catalysts and 20-43 m<sup>2</sup> g<sup>-1</sup> for SCS-based samples. Finally, as presented in Figure 7.18, EDS mapping demonstrates the good distribution of praseodymium and zirconium species [95].



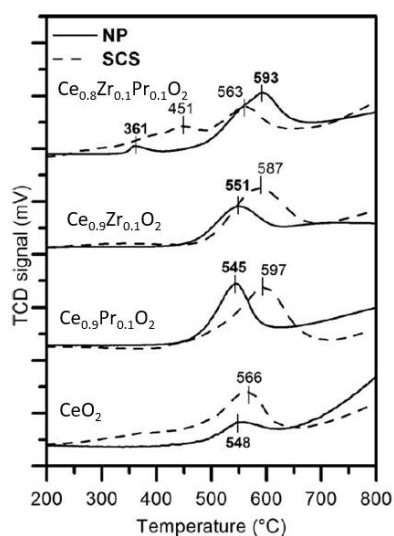
**Figure 7.18:** EDS mapping of Ce<sub>0.8</sub>Zr<sub>0.1</sub>Pr<sub>0.1</sub>O<sub>2</sub> samples obtained via hydrothermal and SCS procedures from ref. [95]

Table 7.4 shows the results of the XPS analysis [95]. The samples obtained through the hydrothermal procedure show a higher quantity of surface oxygen compared to those prepared with the SCS method. This active oxygen or  $\alpha$ -oxygen species can reach (spillover phenomenon) and react with absorbed molecules to guarantee better performance in the oxidation process. The  $\beta$ -oxygen, instead, is the lattice oxygen which contributes to the oxidation reactions in a much more limited way than the previous one. The release of these species is slow and in need of high temperature.

**Table 7.4:** Atomic percentage of oxygen and reduced cerium cations from the XPS analysis adapted from [95]

Sample	$O_{\beta}$ species		$O_{\alpha}$ species		$Ce^{3+}$ % of atoms ( $u_1+v_1$ )
	Binding Energy (eV)	% of atoms	Binding Energy (eV)	% of atoms	
$Ce_{0.8}Zr_{0.1}Pr_{0.1}O_2$ - NP	527.6	54	530.1	46	22
$Ce_{0.8}Zr_{0.1}Pr_{0.1}O_2$ - SCS	529.6	68	531.5	32	21
$CeO_2$ - NP	528.0	58	530.1	42	13
$CeO_2$ - SCS	529.3	66	531.6	34	16

The quantity of  $Ce^{3+}$  species in the Ce-Pr-Zr mixed oxides is higher than that present into the ceria samples. This result is also confirmed by the  $H_2$ -TPR test which is shown in Figure 7.19 [95]. The main reduction peaks have been observed in the temperature range between 530 and 600°C, although the ceria-praseodymia-zirconia sample exhibits two bands at a lower temperature. The bands are assigned to the presence of oxygen species weakly linked to the catalyst surface ( $\alpha$ -oxygen). Therefore, the  $Ce_{0.8}Zr_{0.1}Pr_{0.1}O_2$  catalyst is more reducible compared to the other oxides and the favourite creation of  $Ce^{3+}$  species is than reflected in the oxidation performance.



**Figure 7.19:**  $H_2$ -TPR curves of  $Ce_{0.8}Zr_{0.1}Pr_{0.1}O_2$ ,  $Ce_{0.9}Zr_{0.1}O_2$ ,  $Ce_{0.9}Pr_{0.1}O_2$  and  $CeO_2$  samples adapted from ref. [95]

Although batch systems are widely used to produce ceria-based catalysts, they show some disadvantages such as the production of agglomerates, medium-high working temperature and unsuitable control on the particle size [96]. In this context, microfluidic devices represent a new, advantage apparatus to produce modified ceria catalysts. The objective is to use low-cost reagents by operating at room temperature with better control of the size of nanoparticles compared to the previous procedures. Furthermore, the continuous production of the ceria-based catalysts with reproducible features is a glimpse at the future of the catalyst production systems. Different devices have been studied by varying the size of the mixing chamber, the number of inlets and the diameter of the input and output channels. In this regard, a  $\text{Ce}_{0.8}\text{Zr}_{0.1}\text{Pr}_{0.1}\text{O}_2$  catalyst is synthesized using a multi-inlet vortex reactor (MIVR) [97]. First, two solutions are prepared: one containing the metal precursors and the other composed of sodium hydroxide in water. Then, they are fed into the reactor with different flow rates (2 and  $20 \text{ ml min}^{-1}$ ) in order to obtain two different fluid dynamic conditions inside the mixing chamber to perform a laminar and turbulent mixing. The outgoing solution which contains the catalyst nanoparticles is washed and centrifuged several times and finally calcinated at  $650^\circ\text{C}$ . The multi-inlet vortex reactor is shown in Figure 7.20.

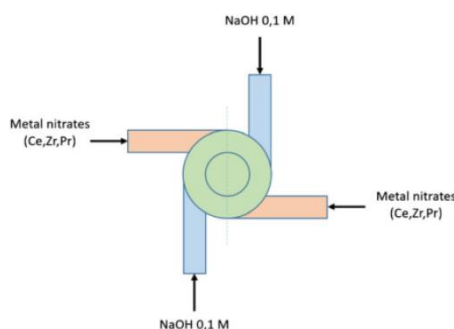


**Figure 7.20:** Multi-inlet vortex reactor representation adapted from [97]

The obtained catalysts are in a solid solution form and the sample synthesized in laminar conditions shows larger particles compared to the other [97]. The specific surface areas are not very high:  $37$  and  $77 \text{ m}^2 \text{ g}^{-1}$  working with flow rates equal to  $2$  and  $20 \text{ ml min}^{-1}$ , respectively. Furthermore, as shown in Figure 7.21, the size distribution coming from the turbulent mixing includes a greater number of equal-dimension particles than the laminar one. Therefore, the fast mixing improves the rate of nucleation with the formation of a high number of primary particles having little time to grow.

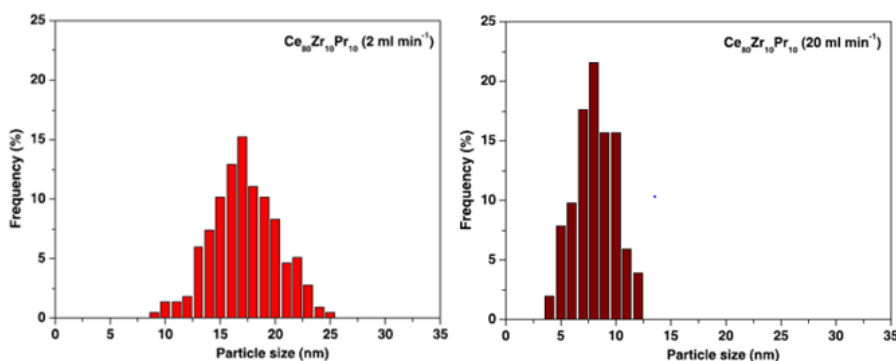


**Figure 7.21:** FESEM analysis of  $\text{Ce}_{0.8}\text{Zr}_{0.1}\text{Pr}_{0.1}\text{O}_2$  catalysts adapted from ref. [97]

## 7.2.2 Catalytic performance of ceria-praseodymia-zirconia catalysts in oxidation reactions

### Catalytic performance of ceria-praseodymia-zirconia catalysts in oxidation reactions – CO oxidation

In this section, several ceria-based systems are compared in order to find the best catalyst for the CO oxidation reaction. The most active sample is the nanostructured ceria obtained via the hydrothermal method with a  $T_{90\%}$  value of 272°C, as illustrated in Figure 7.22. A good performance is also obtained with the  $\text{Ce}_{0.8}\text{Zr}_{0.1}\text{Pr}_{0.1}\text{O}_2$  catalyst synthesized through the SCS method. The latter, indeed, has shown a temperature of 295°C to obtain 90% of CO conversion.

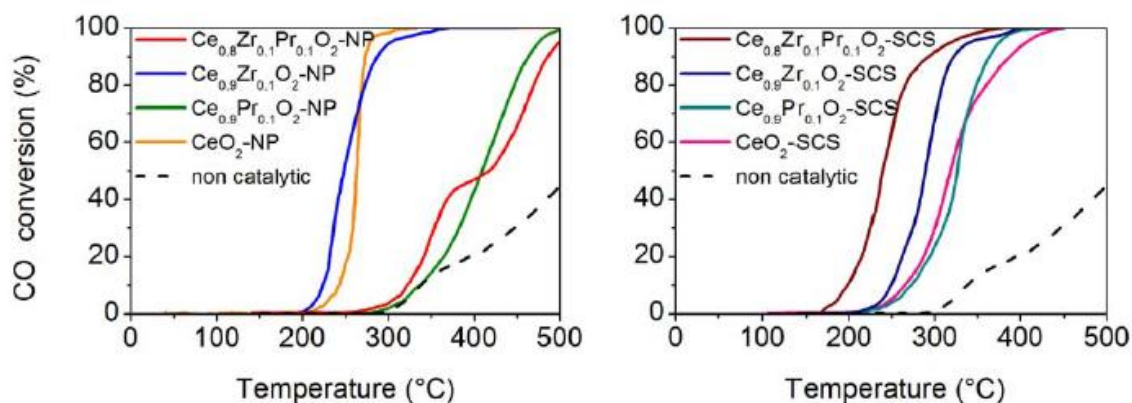


**Figure 7.22:** CO conversion on ceria-based catalysts prepared via hydrothermal (on the left) and SCS (on the right) procedures adapted from ref. [95]

These catalysts show a higher performance compared to the samples prepared through the multi-inlet vortex reactor (MIVR). Concerning these latter systems, a good catalytic activity is achieved using a flow rate of  $20 \text{ ml min}^{-1}$  reaching a  $T_{90\%}$  value of 344°C with the  $\text{Ce}_{0.8}\text{Pr}_{0.2}\text{O}_2$  catalyst, as reported in Figure 7.23. Therefore, using the MIVR reactors, the ceria-praseodymia-zirconia samples are not best-performing systems for the CO oxidation.

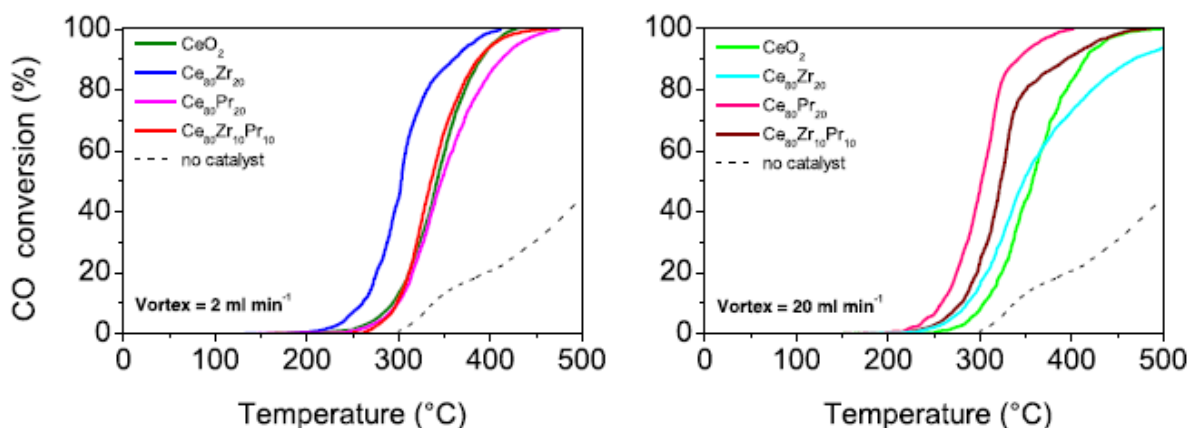


**Figure 7.23:** CO conversion on ceria-based catalysts prepared with a multi-inlet vortex reactor adapted from ref. [97]

## Catalytic performance of ceria-praseodymia-zirconia catalysts in oxidation reactions – Soot oxidation

All the experiments are performed in a “tight” contact between the samples and the soot. Similar behaviour is observed using  $\text{Ce}_{0.8}\text{Zr}_{0.1}\text{Pr}_{0.1}\text{O}_2$  synthesized through both hydrothermal and SCS procedures with  $T_{90\%}$  value equal to 453 and 503°C, respectively. All the other catalysts show less activity compared to the previous ones, as shown in Figure 7.24. In any case, the higher  $\text{CO}_2$  selectivity is detected using nanostructured materials due to their high intrinsic activity. The higher quantity of  $\text{CO}_2$  is obtained using the ceria-praseodymia sample. As a matter of fact, the incorporation of the zirconium ions into the ceria lattice does not show a positive effect on the soot oxidation reaction because some redox-active sites are replaced with non-reducible Zr species [95], [56]. However, the ceria-zirconia-praseodymia system exhibits higher thermal and mechanical stability [58], [93].

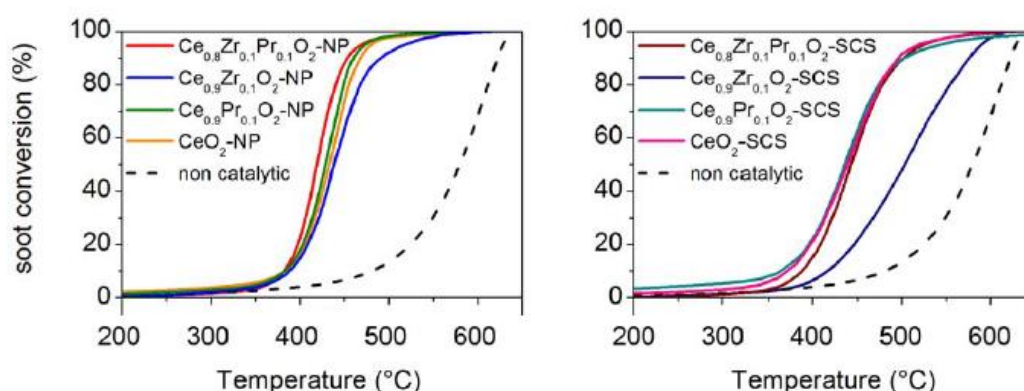


**Figure 7.24:** Soot conversion on ceria-based catalysts prepared via hydrothermal (on the left) and SCS (on the right) procedures adapted from ref. [95]

Among all the studied systems the  $\text{CeO}_2$  sample prepared through the multi-inlet vortex reactor using an inlet flow rate of  $20 \text{ ml min}^{-1}$  has shown the best catalytic activity for the soot oxidation reaction (Figure 7.25). Indeed, the temperature to reach 90% of conversion is  $422^\circ\text{C}$  with obtaining products having good  $\text{CO}_2$  selectivity. Generally, the presence of praseodymium and zirconium species incorporated into the ceria lattice does not promote the oxidation reactions using these “unstructured” ceria-based catalysts [97].

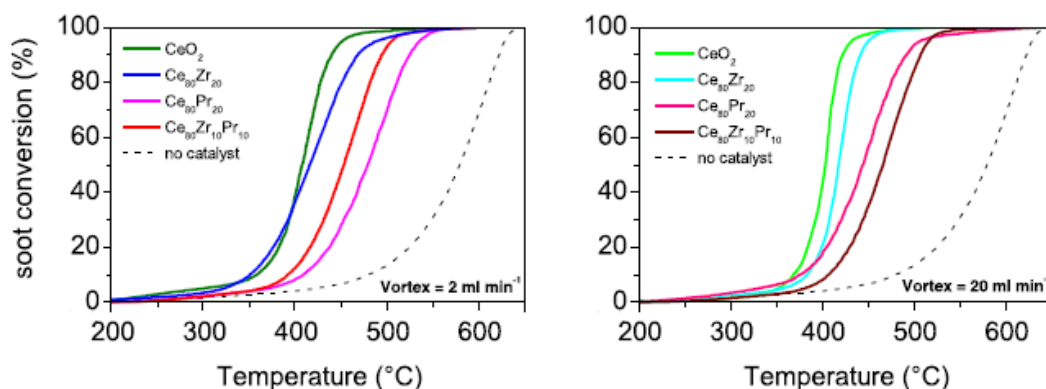


**Figure 7.25:** Soot conversion on ceria-based catalysts prepared with a multi-inlet vortex reactor adapted from ref. [97]

### 7.3 Nanostructured copper-ceria catalysts

#### 7.3.1 General properties and catalyst characterization of copper-ceria catalysts

In recent years, the binary systems based on CuO and CeO<sub>2</sub> have drawn the attention of several researchers due to their high catalytic activity in the oxidation reactions. It has been noted the presence of two combined redox cycles (Ce<sup>3+</sup>/Ce<sup>4+</sup> and Cu<sup>2+</sup>/Cu<sup>+</sup>) as a result of the synergic effect between CuO and CeO<sub>2</sub>, which enhances the Mars van Krevelen mechanism, typical of the oxidation reactions [98], [99]. The representation of the Ce-Cu-O redox cycle is illustrated in Figure 7.26.

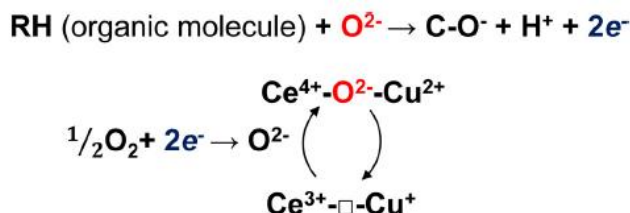


**Figure 7.26:** Representation of the redox cycle in the Ce-Cu-O systems from ref. [98]

In this context, in the second half of the 1900s, it was introduced the concept of ‘‘phase cooperation’’. More specifically, a phase carries out the real catalytic activity, while the other provides an additional function to the system improving its global properties [98], [100]. Moreover, the copper introduction into the ceria lattice leads to the formation of a high number of defect sites, in particular oxygen vacancies, enhancing the dynamic oxygen storage capacity [56]. As shown for the other modified-ceria systems, these catalysts can be synthesized according to different methods, but the most common techniques are the SCS and the hydrothermal procedures. The properties of Ce-Cu mixed oxides with different Ce/Cu ratio prepared through the SCS procedure, are summarized in Table 7.5 [98].

**Table 7.5:** Properties of Ce-Cu mixed oxides synthesized through the SCS method adapted from ref. [98]

Sample	S <sub>BET</sub> (m <sup>2</sup> g <sup>-1</sup> )	Crystallite size (nm) Scherrer equation
CeO <sub>2</sub>	21	28.6
Ce <sub>0.95</sub> Cu <sub>0.05</sub>	25	14.3
Ce <sub>0.85</sub> Cu <sub>0.15</sub>	24	9.7
Ce <sub>0.60</sub> Cu <sub>0.40</sub>	31	9.1
Ce <sub>0.40</sub> Cu <sub>0.60</sub>	25	7.1
Ce <sub>0.15</sub> Cu <sub>0.85</sub>	16	6.9
Ce <sub>0.05</sub> Cu <sub>0.95</sub>	4	-
CuO	3	-

The crystallites dimension becomes smaller and smaller by increasing the copper amount due to the lower  $\text{Cu}^{2+}$  ionic radius compared to the two ceria cations. Furthermore, when the Cu/Ce ratio is quite high, the samples begin to take on a lamellar structure and their dimension is not estimable with the Scherrer equation [98]. Figure 7.27 shows, instead, the X-ray diffractograms of the catalysts. Starting from the pure ceria, the copper introduction does not change the peaks ascribed to the  $\text{CeO}_2$  cubic fluorite structure and obviously, the presence of the CuO phase grows by increasing the Cu content.

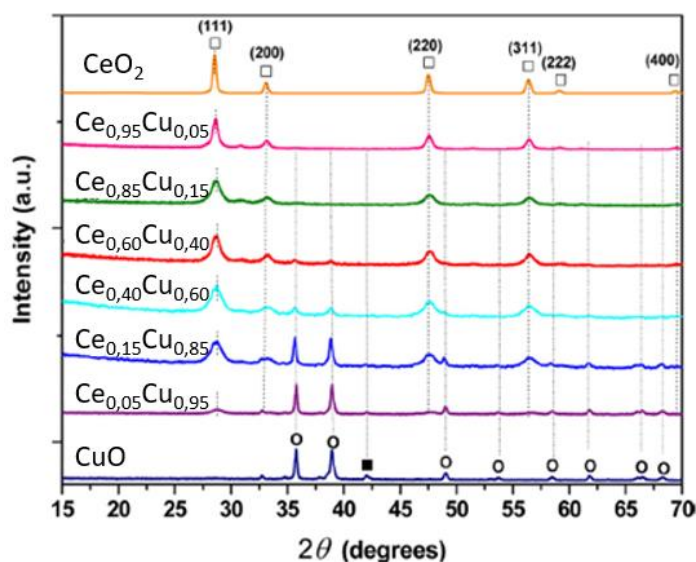


**Figure 7.27:** X-Ray diffractograms of the SCS samples ( $\square=\text{CeO}_2$ ;  $\circ=\text{CuO}$ ;  $\blacksquare=\text{Cu}_2\text{O}$ ) adapted from ref. [98]

The results of the  $\text{H}_2$ -TPR test are illustrated in Figure 7.28.

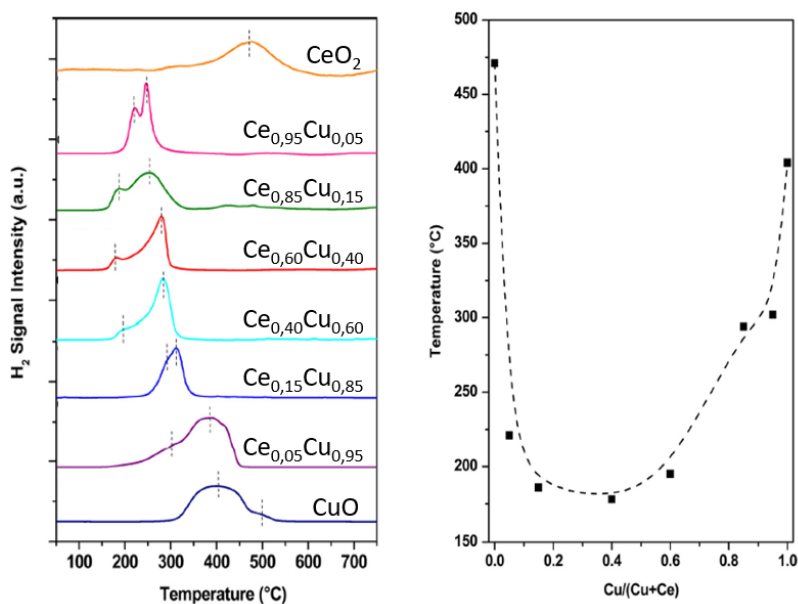


**Figure 7.28:**  $\text{H}_2$ -TPR test on  $\text{Ce}_x\text{Cu}_{1-x}$  samples synthesized through the SCS method adapted from ref. [98]

The mixed oxide peaks appear at a lower temperature compared to the pure CeO<sub>2</sub> and CuO samples. Therefore, the presence of the two phases promotes the catalyst reducibility and, in particular, the Ce<sub>0.6</sub>Cu<sub>0.4</sub> system exhibits the lowest reduction temperature. The latter consists of two peaks; the first at low temperature (150-199 °C) is due to the reduction of relatively small CuO species interacting with the CeO<sub>2</sub>, while the second (200-400°C) corresponds to the reduction of larger CuO domains characterized by weak interaction with the ceria phase [98], [101].

As already seen, the hydrothermal process allows the formation of nanostructured samples with the preferential exposition of different crystalline planes. The HRTEM image illustrated in Figure 7.29 reveals the presence of structural perturbations along the edges and the corners of the ceria nanorods even conserving their global framework [101].

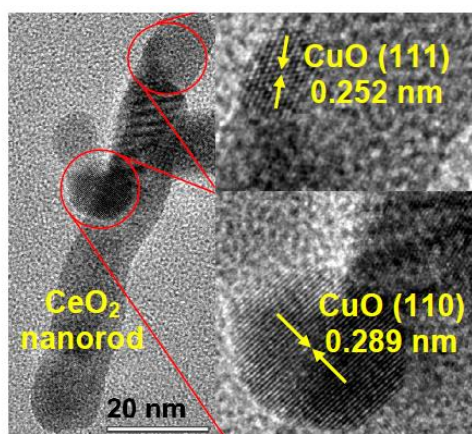
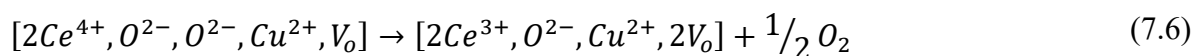


**Figure 7.29:** HRTEM image of copper-ceria nanorods synthesized through hydrothermal synthesis adapted from ref. [101]

The Raman spectra of the copper-ceria catalysts in a nanorods-like structure are shown in Figure 7.30. In this context, the intense band at 462 cm<sup>-1</sup> is attributed to the F<sub>2g</sub> band of the fluorite ceria, while the peaks centred at 292 and 341 cm<sup>-1</sup> are due to the presence of the CuO phase. The copper-ceria framework is compared to the iron-ceria system in order to study the different amount of defect sites in the two structures. More specifically, bands at 606 and 1154 cm<sup>-1</sup> related to the oxygen vacancies formation can be found in the Cu/CeO<sub>2</sub> spectrum but, on the contrary, iron-ceria rods exhibit only a weak peak at 604 cm<sup>-1</sup>. Therefore, the copper-ceria catalysts allow the formation of a greater number of oxygen vacancies than the iron-ceria samples. The replacement of a Ce<sup>4+</sup> cation with a Cu<sup>2+</sup> ion, indeed, consists in the formation of an oxygen vacancy. The [Cu<sup>2+</sup>, Vo] system in combination with the Ce<sup>4+</sup> sites additionally promotes the formation of another oxygen vacancy and Ce<sup>3+</sup> species, according to Equations (7.5) and (7.6) [101].



Furthermore, the Ce-O vibration frequency changes due to the incorporation of the Cu<sup>2+</sup> and Fe<sup>3+</sup> ions into the ceria structure, resulting in a F<sub>2g</sub> peak shift.

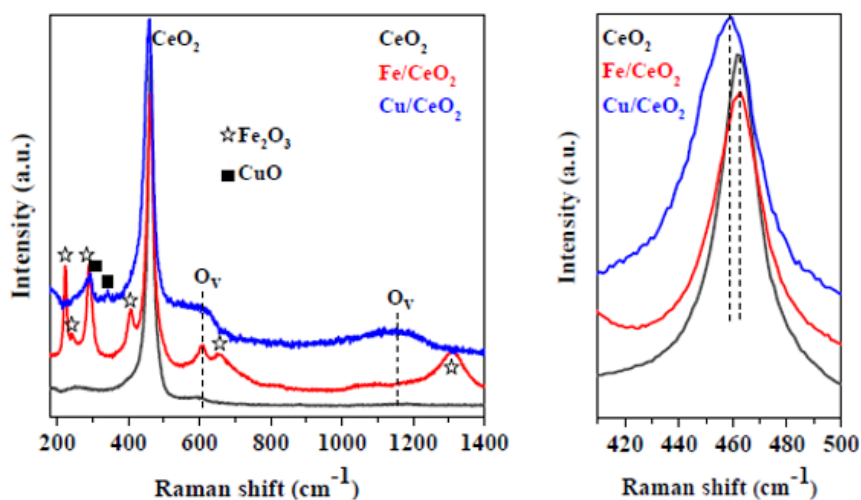


**Figure 7.30:** Raman spectra of ceria, copper-ceria and iron-ceria nanorods adapted from ref. [101]

In conclusion, an IR analysis carried out through the interaction between the pyridine as a probe molecule and the catalyst has proved that the copper-ceria samples contain both strong Lewis and Brønsted acidic sites [101].

The preparation of copper nanoparticles stabilized through an organometallic compound and, subsequently, stored in the CuO form on different ceria samples is another interesting procedure for the production of copper-ceria mixed oxides. These additional species avoid the formation of larger aggregates maintaining small copper oxide domains. In this context, the TEM images have demonstrated that using the ceria-SCS samples as the support, it is possible to obtain a good distribution of the CuO phase characterized by an average particles size less than 10 nm. On the contrary, it is not possible to arrange all the CuO domains on the ceria nanostructures synthesized through the hydrothermal procedure because of their low surface area. For this reason, some CuO species have been detected outside the ceria nanostructures [99].

### 7.3.2 Catalytic performance of copper-ceria catalysts in oxidation reactions

#### Catalytic performance of copper-ceria catalysts in oxidation reactions – NO oxidation

The catalysts prepared through the introduction of Cu nanoparticles stabilized by n-octylsilane and deposited in the form of CuO on different ceria morphologies have been studied for the NO oxidation reaction. As per Figure 7.31, the samples synthesised through the SCS method has shown a considerably higher catalytic activity compared to the Cu/CeO<sub>2</sub> nanostructures. Using the SCS technique, the 5%Cu/CeO<sub>2</sub> has proved to be the most active sample for the NO oxidation exhibiting even greater performance than 1% of the platinum stored on the same ceria structure. The catalytic activity of these catalysts is enhanced by increasing the copper content; consequently, the Cu species play a beneficial role in this oxidation reaction. On the contrary, copper impregnated ceria-based catalysts, which are obtained via hydrothermal procedure, have shown poor catalytic performance in the NO conversion and surprisingly, the addition of copper does not seem to improve their activity. This is most likely caused by the formation of segregated CuO aggregates not directly interacting with the ceria nanoshapes due to the low surface area [99].

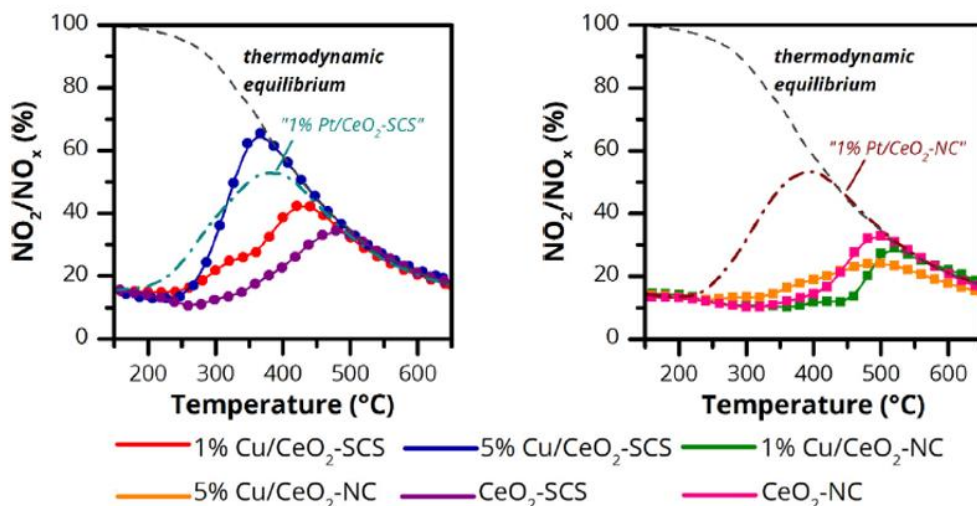


**Figure 7.31:** NO conversion on ceria catalysts synthesised on copper-ceria catalysts through the SCS (on the left) and hydrothermal (on the right) techniques adapted from ref. [99]

Catalytic performance of copper-ceria catalysts in oxidation reactions – CO oxidation

Figure 7.32 shows the TPO-test results performed on CuO-CeO<sub>2</sub> catalysts prepared through the impregnation of Cu nanoparticles on ceria samples. The Cu-impregnated ceria nanostructures exhibit a lower catalytic activity in the CO oxidation compared to the SCS-oxides. This is probably due to the higher surface area of the spongy-like samples which allows a more effective interaction between the copper and the cerium domains and promotes a good oxygen mobility thanks to the high number of oxygen vacancies [99]. In contrast to the nanoshapes, the catalytic activity of the SCS-catalysts is improved by increasing the copper content.

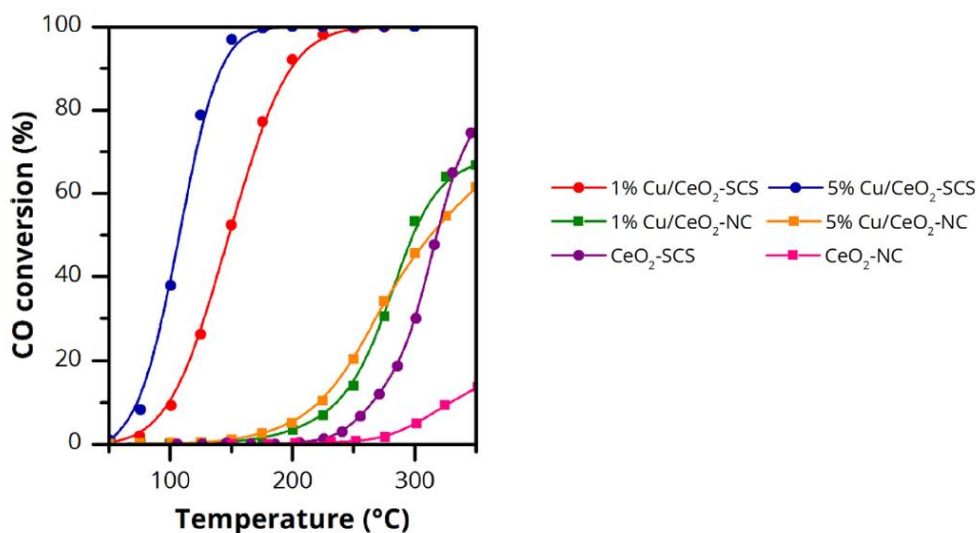


**Figure 7.32:** CO conversion on copper ceria catalysts prepared via SCS and hydrothermal methods from ref. [99]

The CO conversion to carbon dioxide has also been tested on copper-ceria catalysts characterized by different compositions ( $Ce_xCu_{1-x}$ ) and synthesised through the SCS method, starting from cerium and copper nitrates as precursors. The highest catalytic performance has been obtained with the  $Ce_{0.6}Cu_{0.4}$  sample with a  $T_{90\%}$  value of 117°C. This intermediate

composition gives a glimpse of the beneficial role of the coexistence between the  $\text{CeO}_x$  and  $\text{CuO}_x$  domains in the catalyst structure [98].

There are still other experiments in the literature. In particular, the  $\text{CuO}$  phase can be deposited on ceria nanostructures, prepared through the hydrothermal synthesis, according to the deposition-precipitation method. This technique enables to obtain mono- or bi-layers of copper oxide on the ceria nanoshapes surface. In this regard, the catalysts in the form of nanorods and nano-octahedra have shown a higher catalytic activity compared to the nanocubes in the CO oxidation. This fact could be due to the very small surface area of ceria nanocubes obtained in the treated experiment (about three times and a half lower than the other samples) that does not allow a good deposition of the  $\text{CuO}$  phase. Additionally, considering that the carbon monoxide is adsorbed on the  $\text{Cu}^+$  active sites and then oxidized by the active oxygen as a consequence of the interaction between the gaseous  $\text{O}_2$  and the oxygen vacancies, the greater presence of  $\text{Cu}^+$  species observed on the ceria nanorods and nano-octahedra certainly promote the CO conversion [102].

#### Catalytic performance of copper-ceria catalysts in oxidation reactions – Soot oxidation

Concerning the cerium-copper oxide catalysts synthesised through the SCS method by varying the Ce/Cu ratio, the  $\text{Ce}_{0.95}\text{Cu}_{0.05}$  sample has shown the highest catalytic activity in the soot oxidation reaction performing the TPO test in the presence of oxygen and under catalyst-soot “tight” conditions. A 90% particulate conversion is obtained with a temperature of  $434^\circ\text{C}$ . Therefore, it seems that the catalytic performance decreases by increasing the copper content in the structure of the catalysts. This is mainly due to the reduction of the  $\text{Ce}^{3+}/\text{Ce}^{4+}$  redox active sites [98].

Furthermore, the catalytic activity of the soot oxidation reaction has been studied through a TPO test performed on ceria-based catalysts containing copper domains in the  $\text{CuO}$  form, prepared through Cu nanoparticles stabilized with n-octylsilane. The analysis has been carried out with and without the presence of  $\text{NO}_x$  species, as illustrated in Figure 7.33. As for the soot conversion in the absence of  $\text{NO}_x$  molecules, it has been noted, as a general rule, that the nanostructured samples exhibit a higher catalytic activity compared to the other. The presence of copper improves the catalytic performance, but the reaction is independent of the  $\text{CuO}$  quantity. More specifically, a  $T_{90\%}$  value of  $617$  and  $615^\circ\text{C}$  has been achieved using 1 and 5% of copper, respectively. In the presence of  $\text{NO}_x$  species, instead, the best overall catalytic activity has been observed in the nanostructured 1%  $\text{Cu}/\text{CeO}_2$ . However, at low temperature, the SCS-samples enable a higher soot oxidation performance than the nanoshapes due to the large  $\text{NO}_2$  production. The soot oxidation reaction is indeed controlled by the presence of  $\text{NO}_2$  molecules in the temperature range between  $250$  and  $400^\circ\text{C}$ , as previously investigated. Conversely, at high temperature, the formation of oxygen active species on ceria nanostructures becomes predominant in the soot conversion [99].

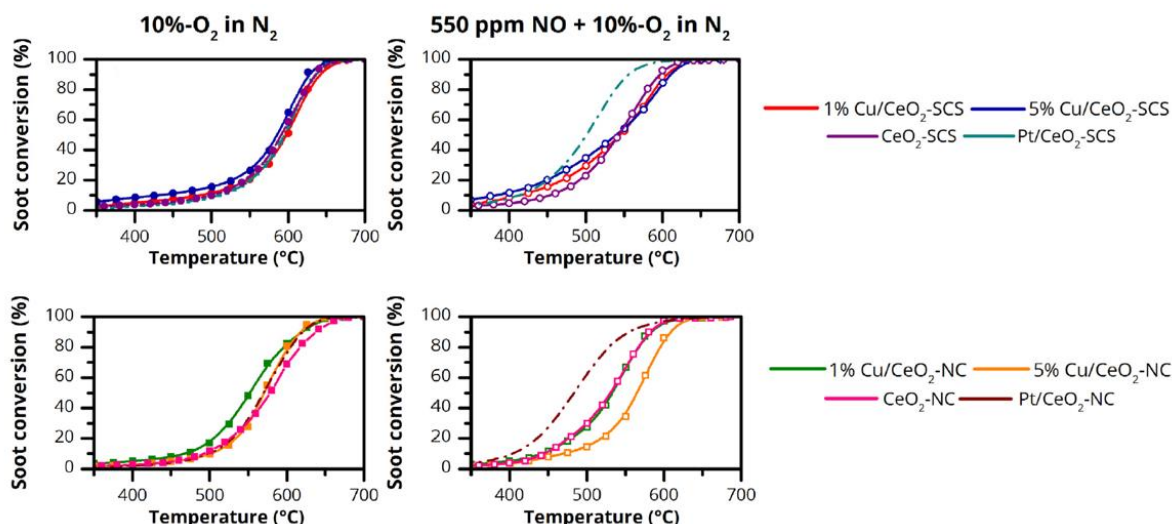


**Figure 7.33:** Soot conversion on copper-ceria catalysts with and without the presence of NO<sub>x</sub> species adapted from ref. [99]

Different stability tests have also been performed on the catalysts of this experiment. It has been noted that the soot oxidation conversion decreases by increasing the number of catalytic cycles and the phenomenon is emphasised in the samples with the highest copper content. A marked reduction of the NO conversion in different subsequent reaction routes has been observed, as illustrated in Figure 7.34. Considering that 5%Cu/CeO<sub>2</sub> is the most active catalyst for the NO oxidation to NO<sub>2</sub> and it is also the catalyst which loses more catalytic performance during the test repetitions, it can be assumed that a sintering phenomenon of the copper active sites exists. A particles migration and a coalescence effect have been proved by performing an EDX element mapping, remarking the formation of segregated CuO domains [99].

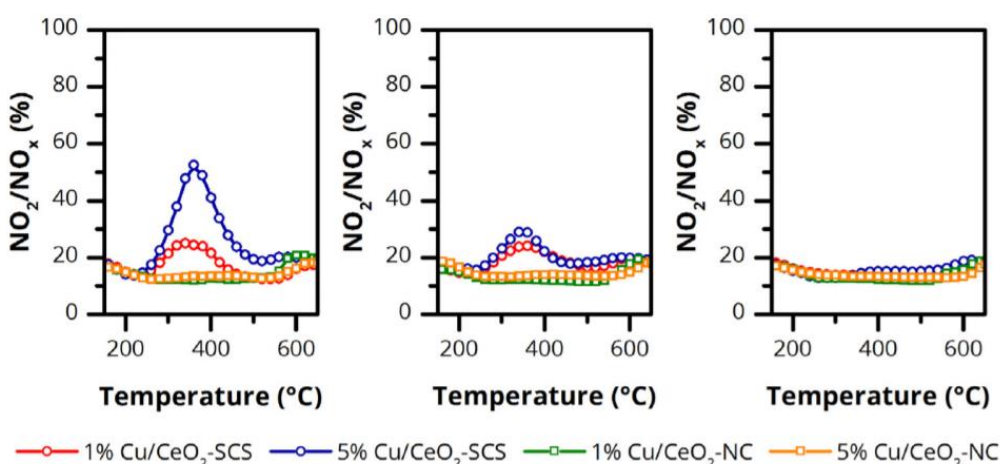


**Figure 7.34:** NO<sub>2</sub> concentration in subsequent catalytic tests adapted from ref. [99]

Other experiments have been carried out in both “loose” and “tight” contacts between the catalyst and the soot by comparing the activity of the copper and the iron species in the soot oxidation reaction. The CuO presence has proved to be more efficient than the Fe<sub>2</sub>O<sub>3</sub> domains

in the particulate conversion due to a high cooperation mechanism between the redox and the acidic sites in the structure [101].

### Catalytic performance of copper-ceria catalysts in oxidation reactions – VOCs oxidation

Ethene has been investigated as the representative molecule of the volatile organic compounds for the total oxidation reaction on copper-ceria catalysts. Different copper-ceria compositions, synthesised through the SCS method, have been tested to determine the most active sample for the reaction. The  $\text{Ce}_{0.6}\text{Cu}_{0.4}$ , as expected from its good textural properties and its lowest reduction temperature, has proved to be the best material in the ethene oxidation, as demonstrated in Figure 7.35. The CuO domains can optimally interact with the ceria enhancing the redox properties of the system. It has been noted a substantial increase of defect sites, in particular oxygen vacancies, responsible for the high catalytic activity [98].

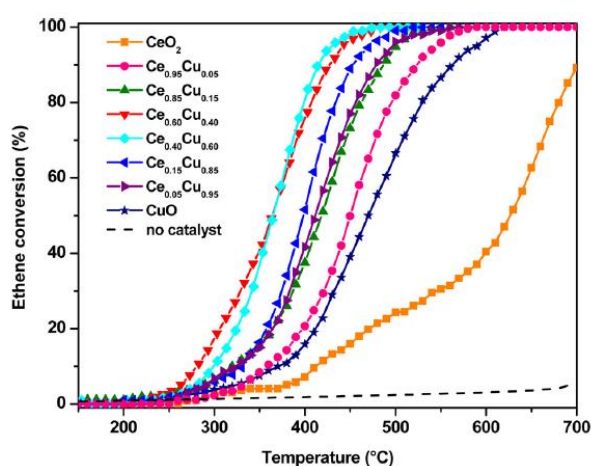


**Figure 7.35:** Ethene conversion on copper-ceria catalysts synthesised through the SCS technique adapted from ref. [98]



## 8. Noble metals supported on ceria catalysts

Currently, it is known that noble metals are the most active catalysts for the oxidation reactions although, especially in recent years, research groups have been constantly looking for new samples with comparable features. The main problem of platinum, palladium and rhodium is the higher cost compared to the other catalysts. Therefore, whenever possible, they are replaced by metal oxides otherwise it is attempted to optimize the synthesis procedures by minimizing the amount of required noble metals. In any case, noble metal samples are not usually synthesized as bulk catalysts, but they are dispersed in the form of a nanometric cluster on porous supports, which are called carriers. In this regard, as seen in this work, ceria samples show unique and fundamental properties compared to the other materials, playing an increasing important role in the oxidation reactions. It has also been proved that the ceria functionalities are improved when it is used as a support for noble metals [103]. A fundamental parameter for these catalysts is the dispersion of the noble metals on the carrier. The definition of this notion is reported in Equation (8.1).

$$\text{Dispersion} = \frac{\text{Number of accessible atoms}}{\text{Number of total atoms}} \quad (8.1)$$

Therefore, the dispersion must be as high as possible to take advantage of the maximum possible amount of noble metals.

### 8.1 General properties and catalyst characterization of NM/ceria catalysts

#### 8.1.1 Platinum supported on ceria catalysts

Platinum is commonly deposited on the ceria catalysts with the traditional impregnation techniques. Regarding the materials characterization, the XRD analysis on the Pt/CeO<sub>2</sub> samples does not show additional peaks due to the presence of Pt or PtO<sub>x</sub> phases using a quantity of platinum less than 1%. The mean diameter of the platinum particles can be estimated from TEM and HRTEM images according to the formula shown in Equation (8.2) [104].

$$\text{Mean diameter } d \approx \frac{\sum_i n_i d_i}{\sum_i n_i} \quad (8.2)$$

The dimension of these particles varies from experiment to experiment but, in general, it is between 1 and 4 nm [104], [105]. Figure 8.1 shows the TEM images of platinum deposited on ceria catalysts.

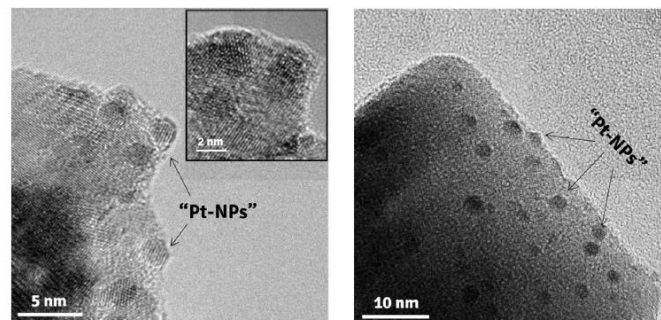


**Figure 8.1:** Platinum supported on SCS-ceria (on the left) and ceria nanocubes (on the right) adapted from ref. [105]

It is possible to obtain well-deposited spherical platinum particles on both ceria-SCS and ceria nanoshapes samples.

The X-ray photoelectron spectroscopy has proved that the most abundant cerium oxidation state present in the Pt/CeO<sub>2</sub> samples is the 4+. Furthermore, the quantity of Ce<sup>3+</sup> species is slightly higher in the SCS-catalysts than in the nanostructured ones and the platinum addition does not change the percentage of the reduced cerium cations. The percentage of active oxygen is another interesting aspect; the samples synthesized via the SCS method show a greater percentage of O- $\alpha$  than the other before the noble metal impregnation. The addition of platinum causes a change in trend, making the nanostructured catalysts richer in active low-bound oxygen species. In all the samples, the most available platinum oxidation state is the 2+ due to the oxidation of the zero-valent noble metal into Pt(II) during the calcination process. More specifically, the SCS-catalysts mainly contain Pt(II) species and a little amount of Pt(IV). The ceria nanoshapes, instead, are constituted by Pt(II) particles, a substantial quantity of Pt(IV) and surprisingly a small number of Pt<sup>0</sup> species [105]. Other studies have found that greater amounts of Ce<sup>3+</sup> and Pt<sup>0</sup> are present when platinum is supported on ceria nanorods rather than on other nanoshapes [104].

Figure 8.2 shows the UV Raman spectra of the ceria nanoshapes prepared through hydrothermal synthesis with and without the presence of platinum. The peak centred at 458 cm<sup>-1</sup> is assigned to the characteristic F<sub>2g</sub> band of the cubic fluorite ceria. In the light of the above mentioned studies, the nanorods I<sub>D</sub>/I<sub>F<sub>2g</sub></sub> ratio is greater than the nanocubes and the nano-octahedra one. Interestingly, for all the nanostructures, the addition of platinum increases this ratio and, consequently, the number of intrinsic defect sites, thus obtaining more active catalysts. These observations can also demonstrate the higher OSC property of Pt/ceria nanorods compared to the other samples [104].

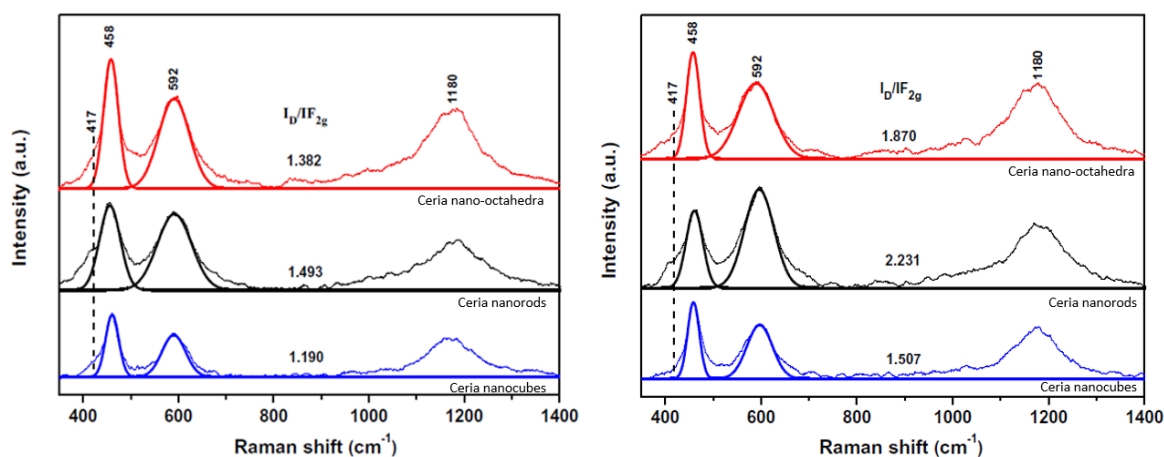


**Figure 8.2:** Raman spectra of CeO<sub>2</sub> (on the left) and Pt/CeO<sub>2</sub> (on the right) nanoshapes adapted from ref. [104]

### 8.1.2 Palladium supported on ceria catalysts

The carbon dioxide emissions can vary considerably depending on the fossil fuels used in the combustion process. According to the Intergovernmental Panel on Climate Change (IPCC), the coal is the most polluting compound with a CO<sub>2</sub> emission of 403.2 kg per megawatt-hour of energy produced. Taking into account that the production of carbon dioxide decreases by reducing the number of carbon atoms in the used fossil fuel, the natural gas turns out to be the most environmentally friendly category for the energy production, owing an emission factor lower than 1.3 and 1.2 compared to Diesel and gasoline engines, respectively [106]. In the context of the CO<sub>2</sub> reduction, the use of natural gas is increased significantly in the last few years, although it has been found that methane is a dangerous greenhouse gas. The development of a catalytic system capable of performing the oxidation of the unburned methane coming from both the natural gas vehicles and the industrial plants has become one of the greatest challenges of the environmental catalytic field [107].

Palladium-based catalysts are the most active and effective samples for the unburned methane abatement, even though, in the literature, some points remain open. In particular, many studies have been performed to determine the active phase of the reaction during the typical operating conditions. In this context, the Pd-catalysts can change their thermodynamically stable phase by varying the oxygen partial pressure and the temperature [108]. Some studies show that the palladium oxide appears to be the active phase in the methane oxidation, being unstable at high temperature; in fact, the PdO decomposition to Pd occurs at about 1000 K with an oxygen partial pressure of 20 mbar. The PdO/Pd transition gives a negative contribution to the system due to a decrease in its catalytic activity [109]. The work of several research groups has proved that the catalytic activity of the system at a high temperature can be recovered according to a re-oxidation process of the palladium metal. In these operative conditions, the most effective way to promote the PdO formation and to reduce the thermal hysteresis of PdO decomposition and reformation is the addition of ceria to the catalytic washcoat. As presented in Figure 8.3, the interaction between the gaseous oxygen and the cerium oxide allows the formation of active oxygen species which play an interesting role in the Pd oxidation [109], [110].

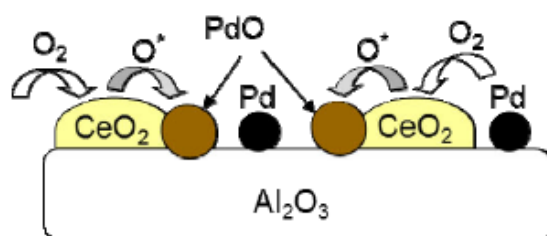


**Figure 8.3:** Pd oxidation to PdO on a ceria-alumina support from ref. [110]

Other studies, obtained combining density functional theory (DFT) calculations and X-ray diffraction analyses, have proved instead that it is possible to obtain a high methane conversion performing the reaction on under-coordinated Pd-sites present on the PdO species or palladium in the metal form. Therefore, it seems that the most active phase in methane oxidation is a mixture of metallic Pd and PdO compounds. More specifically, the metallic Pd and the under-coordinated sites of PdO (101) are able to polarize the CH<sub>4</sub> molecules by facilitating the break of the C-H bonds. The observed polarization on PdO (100) is instead negligible. The breakage of the hydrogen-carbon bond is fundamental for the dissociative

adsorption of methane, which is considered the rate-determining step of this oxidation process due to the high stability of the molecule [111], [112].

It has been observed that, by comparing different materials such as  $\text{Al}_2\text{O}_3$ ,  $\text{SiO}_2$  and  $\text{MgO}$ , the role of the support is negligible in the methane oxidation reaction. Indeed, the latter only depends on the intrinsic activity of the Pd species [113]. On the contrary, the use of the ceria both as a promoter in the catalyst preparation and support has a beneficial effect in the  $\text{CH}_4$  oxidation. The combined use of palladium and ceria enhances a mutual increase in the redox properties of the two species. A low reduction temperature of the cerium oxide has been observed in the presence of the noble metal. As previously seen, the ceria promotes the re-oxidation process of the metallic Pd allowing the formation of PdO, which is considered the most active phase of the reaction at high temperature. Conversely, the role of the  $\text{CeO}_2$  at low temperature is still a discussed topic. The active phase of the reaction in these operative conditions has not been established yet. Some papers in the literature conclude that the palladium in different oxidation states such as  $\text{Pd}^0$ ,  $\text{Pd}^{2+}$ ,  $\text{Pd}^{4+}$  and sub-stoichiometric  $\text{PdO}_x$  species is more active compared to the PdO. Additionally, the support shows less activity than the important role played at high temperature [109], [110].

The synthesis procedure and the exposition of different ceria planes can certainly change the catalytic activity of the system regarding the methane oxidation reaction. In this respect, ceria microspheres and nanotubes have been prepared through the hydrothermal method and the palladium introduction has been carried out according to the impregnation technique [114]. The obtained samples have a palladium content of 0.5wt% and their SEM images are visible in Figure 8.4.

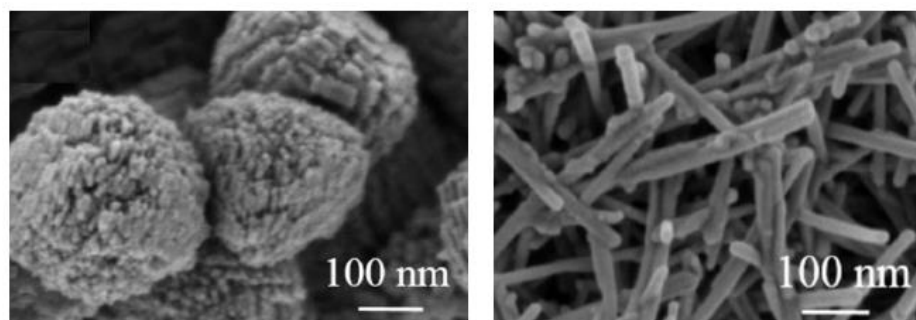


**Figure 8.4:** SEM images of Pd/ceria microspheres and nanotubes adapted from ref. [114]

The  $\text{N}_2$  adsorption-desorption isotherms indicate that the ceria microspheres are characterized by a mesoporous structure, whereas the type III curve observed for the nanotubes samples suggests their predominant macroporous organization. Moreover, both TEM and HRTEM images have shown a good PdO dispersion on the two ceria morphologies [114].

Lamellar octahedra ceria (LOC), synthesised through the hydrothermal procedure, has also been studied to obtain a surface-stepped structure (Figure 8.5) characterized by a higher exposition of (110) planes compared to the classical octahedra nanoshapes. Metal-doped LOC has also been tested (LOC-M, where M: Zr, Ni, Co). These species have been introduced in the catalytic structure through the wet impregnation method starting from an aqueous solution of zirconium, nickel and cobalt nitrates. The Zr addition is certainly a good subject for research, whereas the Ni and the Co incorporation has lower practical applicability due to the toxicity of

these elements. Palladium has been deposited on all the samples via the wet impregnation procedure by varying its content from 0.5 to 1.5 wt% [115].

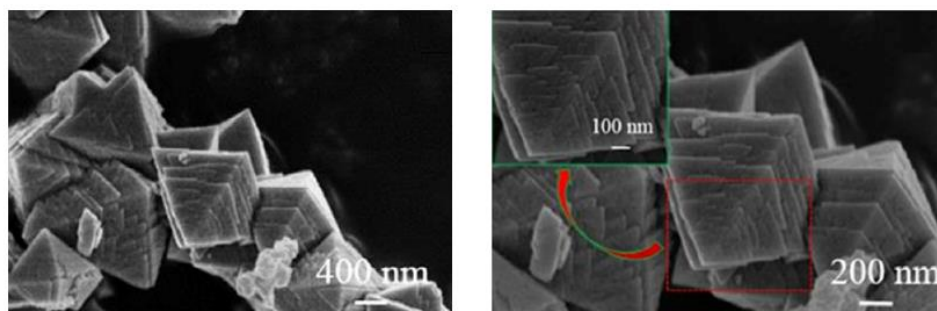


**Figure 8.5:** SEM images of the octahedral ceria characterized by a surface-stepped structure adapted from ref. [115]

The XRD analysis results show the typical peaks of the cubic fluorite structure of ceria. Conversely, the diffraction peaks of Pd and PdO species have not been observed in the XRD pattern of the samples due to the low-palladium content and its high dispersion. The latter point has also been demonstrated by the HRTEM images [115].

The SCS technique has been widely studied in recent years due to the low complexity of the synthesis procedure and the obtainment of good catalytic performance. In this respect, palladium-based catalysts have been prepared using different Pd content and a fixed quantity of ceria on alumina. The samples are synthesised starting from palladium, cerium and aluminium nitrates. The high-resolution TEM image and its fast Fourier transformation (FFT) mode of the Pd-CeO<sub>2</sub>-Al<sub>2</sub>O<sub>3</sub> samples are illustrated in Figure 8.6. The palladium and the cerium oxides constitute double-domain aggregates in which the Pd-nanoparticles are surrounded by the ceria ones reproducing a core-shell structure. The latter can significantly increase both the activity and the stability of the system during the methane oxidation reaction.

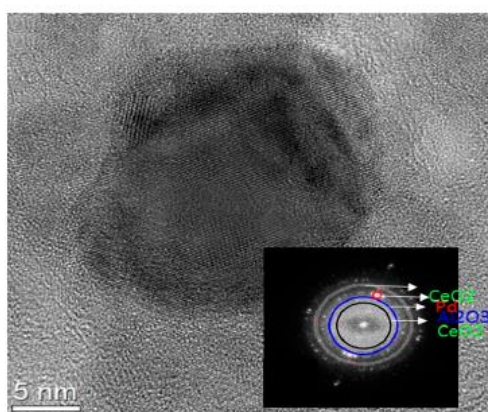


**Figure 8.6:** HRTEM image and its fast Fourier transformation (FFT) mode of the Pd-CeO<sub>2</sub>-Al<sub>2</sub>O<sub>3</sub> samples adapted from ref. [116]

The surface composition of the different catalysts prepared via the SCS procedure has been investigated through the XPS analysis. The surface species of these samples are also

compared with those of a material synthesised by soaking the alumina support with palladium and cerium oxide. The palladium is mainly present in the Pd<sup>0</sup> and PdO forms on the catalytic surface of the sample obtained through the wet impregnation method. On the contrary, the catalysts prepared via the SCS synthesis show a smaller amount of PdO compared to the previous ones. They are also characterized by a little quantity of palladium in the Pd<sup>0</sup> form. The most interesting thing concerning the SCS-samples is the direct incorporation of Pd ions in the lattice ceria with the formation of a Pd-O-Ce solid solution. As described in Figure 8.7, the latter is linked to a high catalytic activity due to the formation of oxygen vacancies with simultaneous generation of Ce<sup>3+</sup> ions [116].

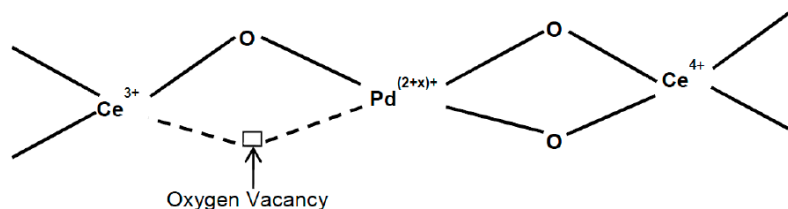


**Figure 8.7:** Palladium-ceria solid solution obtained through the SCS procedure from ref. [116]

Another engineered process for the preparation of this type of catalysts involves the use of one-step dry milling aimed at the production of high-performance samples. Avoiding the use of palladium nitrate or chloride precursor, the procedure is characterized by the generation of less chemical waste compared to the other methods. In this respect, Pd nanoparticles have been mixed with the cerium oxide in a ball mill and aged at 900°C, meanwhile, a second sample has been prepared using the same method but starting from PdO nanoparticles. These catalysts have been further compared to other samples obtained through the wet impregnation and the SCS synthesis procedures. All these materials are characterized by a platinum weight percentage of 1% and their surface area is less than 10 m<sup>2</sup> g<sup>-1</sup>. According to the HRTEM images in Figure 8.8, the catalysts obtained using the advanced ball-milling method consist of ceria crystallites surrounded by an amorphous layer with a thickness ranging from 2 and 5 nm. The latter, based on the EDX analysis, is composed of a mixed palladium-ceria phase. Additionally, palladium particles with size no greater than 5 nm have been observed in the amorphous layer. This peculiar morphology has not been detected on the catalysts obtained from PdO nanoparticles and on the SCS and wet impregnation samples [117].

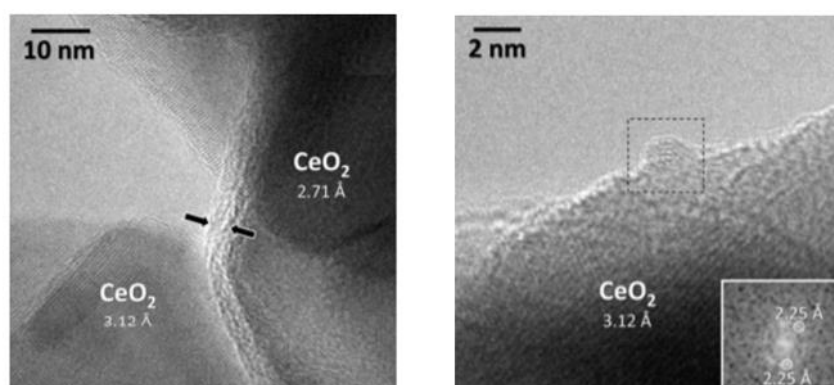


**Figure 8.8:** HRTEM images of palladium-ceria catalysts obtained using the ball-milling method adapted from ref. [117]

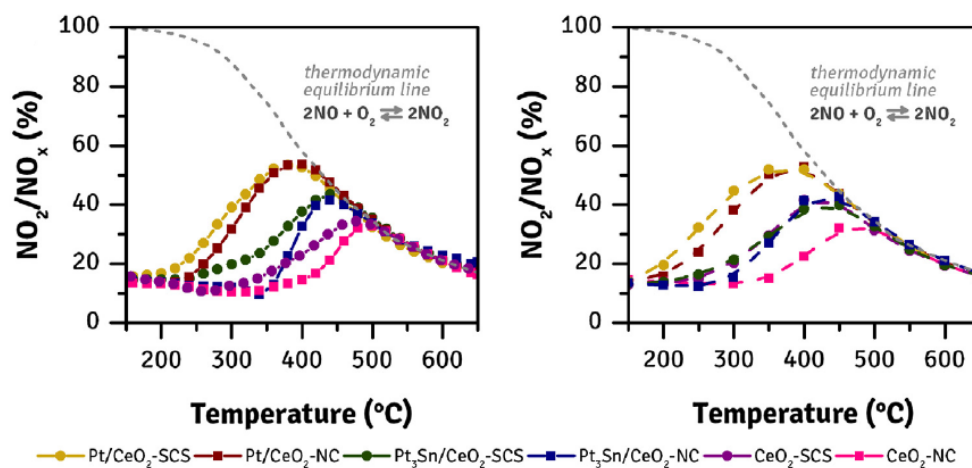
Finally, the XPS analyses show that the sample obtained from Pd-nanoparticles consists of a higher  $Ce^{3+}/Ce^{4+}$  ratio compared to the other. This fact gives a glimpse of the strong interaction between the platinum and the cerium in the lattice structure. Furthermore, the  $Pd^0$  species have not been observed either in the ball-milling sample or in the wet impregnation catalyst. The latter is characterized by a lower amount of  $Pd^{2+}$  ions than that obtained through the milling method, but it presents a higher quantity of  $Pd^{4+}$ . This trend is, on the contrary, inverted after many reaction cycles [117].

## 8.2 Catalytic performance of NM/ceria catalysts in oxidation reactions

### 8.2.1 Catalytic performance of platinum supported on ceria catalysts

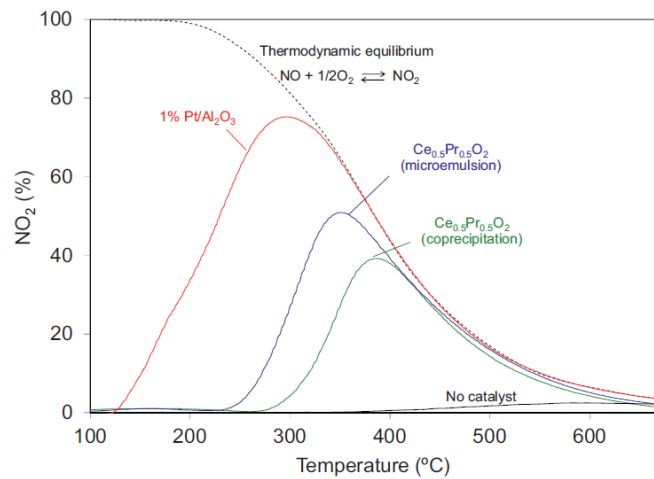
#### Catalytic performance of Pt/ceria-based catalysts in oxidation reactions – NO oxidation

Figure 8.9 shows the NO oxidation reaction performed by heating the system with a ramp of  $5^{\circ}C\ min^{-1}$  and a different step of  $5^{\circ}C$ , followed by an isothermal treatment. In both cases, the temperature has been increased from 50 to  $650^{\circ}C$ . Compared to the first method, the second process bringing the reaction as close as possible to its thermodynamic equilibrium obtaining more correct outcomes in terms of catalytic activity [105]. In any case, the two procedures have provided comparable results. In comparison to the pure ceria, the presence of platinum increases the production of  $NO_2$  and shifts the peak of the curves to a lower temperature.  $Pt/CeO_2$  synthesized via both hydrothermal and SCS methods have shown similar performance with a maximum  $NO_2$  production at about  $400^{\circ}C$ , equivalent to 53% of the NO conversion.



**Figure 8.9:** NO conversion on  $Pt/CeO_2$  and  $Pt_3Sn/CeO_2$  samples in ramping (on the left) and stepwise isothermal (on the right) procedures adapted from ref. [105]

The previous experiment has been performed using a mixture of  $100\ ml\ min^{-1}$  containing 500 ppmv of NO and 10%-v of  $O_2$  in nitrogen. However, it is interesting to note the result of another catalytic test shown in Figure 8.10; it has been carried out with 500 ppm of NO in 5% of  $O_2/N_2$  and a flow rate of  $500\ ml\ min^{-1}$ . In this case, the same performance obtained by using  $Pt/CeO_2$  samples is achieved using the equimolar ceria-praseodymia mixed oxide synthesized through the microemulsion procedure [118].



**Figure 8.10:** NO conversion on different catalysts obtained with different synthesis procedures from ref. [118]

A further test performed in the same conditions of the first experiment has confirmed that the addition of platinum to the equimolar ceria-praseodymia sample, synthesized through the hydrothermal method, does not change its catalytic activity [91], as illustrated in Figure 8.11.

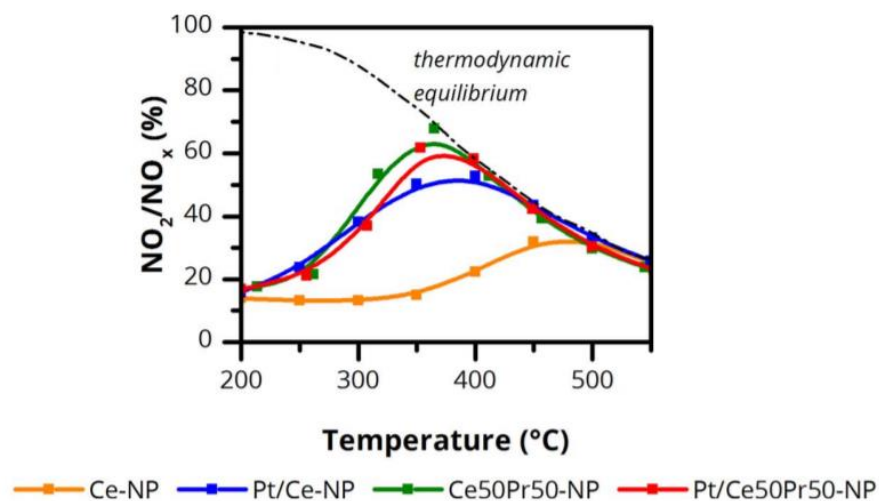


**Figure 8.11:** NO oxidation on ceria-based catalysts with and without the presence of platinum from ref. [91]

Ultimately, it has been proved that the use of a mixed oxide allows obtaining a catalytic activity comparable to that of platinum but at lower costs.

### Catalytic performance of Pt/ceria-based catalysts in oxidation reactions – CO oxidation

Concerning the CO oxidation, pure ceria synthesized through both SCS and hydrothermal procedures is inactive at 50°C; a reaction rate equal to zero has been observed. Pt/CeO<sub>2</sub> prepared via the SCS method has proved to be the most active catalyst as the complete CO conversion has been reached at 80°C, as shown in Figure 8.12. This same result has also been obtained for the Pt/CeO<sub>2</sub> with a nanocubes structure, although the nanostructured catalysts have shown lower activity at low temperature. Given that the platinum content in the two samples is the same, this discrepancy could be due to the higher surface area of the SCS catalyst which is about four times greater than that of nanocubes (28 and 8 m<sup>2</sup> g<sup>-1</sup>, respectively) [105].

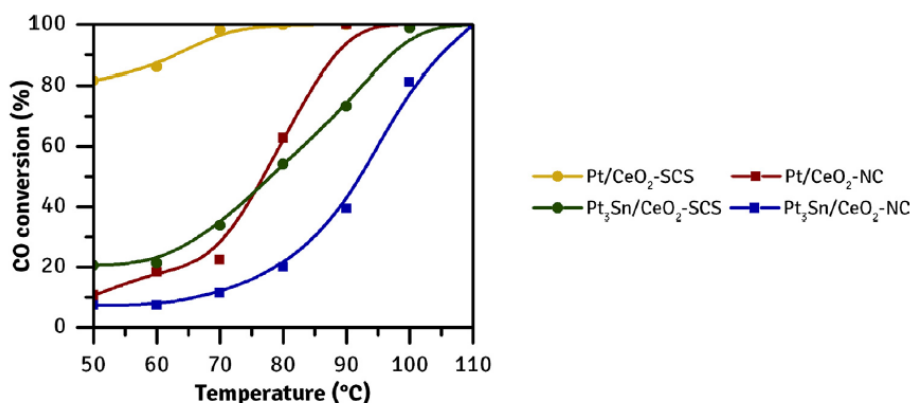


Figure 8.12: CO conversion on Pt/CeO<sub>2</sub> and Pt<sub>3</sub>Sn/CeO<sub>2</sub> samples adapted from ref. [105]

### Catalytic performance of Pt/ceria-based catalysts in oxidation reactions – Soot oxidation

As explained above, the most active catalyst for the soot oxidation is the equimolar ceria-praseodymia synthesized through the hydrothermal method. The objective of this section is to study the role played by the addition of platinum. As shown in Figure 8.13, the presence of the noble metal in the system does not provide additional positive effects to the particulate oxidation reaction in an environment containing or not containing NO. On the other hand, it has been noted that the highest CO<sub>2</sub> yield, and therefore the minimum CO production, is obtained performing the reaction in presence of platinum [91]. Consequently, even though the platinum impregnation does not substantially change the catalytic activity of the system, it increases the CO<sub>2</sub> selectivity of the reaction.

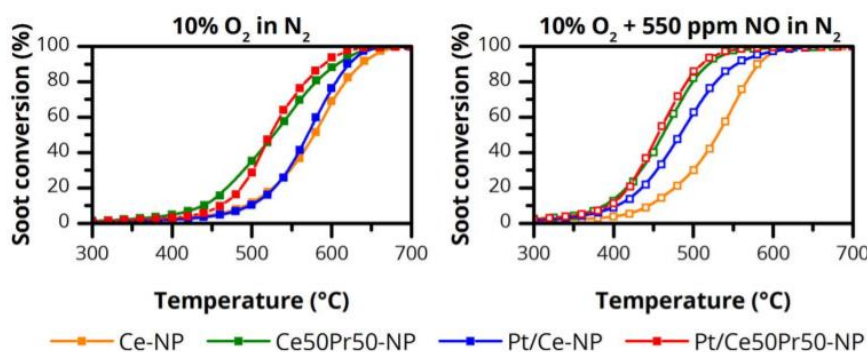


Figure 8.13: Soot oxidation on ceria and Pt/ceria based catalysts with and without the presence of NO adapted from ref. [91]

The addition of platinum has also been investigated on other ceria-based systems. More specifically, a thermogravimetric analysis has been performed on a soot-Pt/Ce<sub>0.68</sub>Zr<sub>0.32</sub>O<sub>2</sub> mixture both in the presence and in the absence of NO to determine the kinetic parameters of the oxidation reaction. Two types of soot have been taken into account: the first is the material with all its components and the second is a particulate matter devoid of the SOF fraction due to its contact with the noble metal within the DOC system. As expected, in presence of the platinum, the activation energy is lower and the pre-exponential factor is greater compared to the system without the catalyst. Furthermore, the kinetic parameters improve if using a gaseous flux containing NO. The sample with the SOF segment, although hardly realistic in real applications, has shown better performance than the other due to a synergetic temperature increase caused by the SOF combustion at about 300-400°C [35].

Another studied system is the platinum incorporation into a cerium-lanthanum mixed oxide. The catalytic performance of this latter has been compared to that of pure ceria, ceria-lanthanum system and Pt/CeO<sub>2</sub>. It has been observed that the Pt-containing samples are more active than the others and the presence of La<sup>3+</sup> enhances the catalytic activity of the ceria. More to the point, platinum and lanthanum seem to operate in a cooperation mechanism aimed to decrease both the release and the incorporation temperature of oxygen. According to a temporal analysis of products (TAP), which is used to investigate the interaction between gaseous labelled oxygen (18O<sub>2</sub>) and the samples, platinum plays an important role in the O<sub>2</sub> capture [119].

#### Catalytic performance of Pt/ceria-based catalysts in oxidation reactions – VOCs oxidation

The conversion of toluene into carbon dioxide has been studied as an example of catalytic oxidation of volatile organic compounds. In particular, the toluene conversion has been evaluated on the three ceria nanostructures with and without the addition of platinum (0.2%) [104]. It has been noted that the presence of highly dispersed platinum nanoparticles increases the catalytic activity of the ceria samples. Furthermore, the high presence of defect sites and the high OSC have made the Pt/CeO<sub>2</sub> nanorods the most performant catalysts for the toluene oxidation. The catalytic conversion on this sample has shown the lower activation energy, as demonstrated in Figure 8.14, and turned out to be a structure-sensitive reaction since its activity has changed on the ceria nanoshapes. Finally, the Pt/CeO<sub>2</sub> nanorods sample has proved a CO<sub>2</sub> selectivity of 100%.

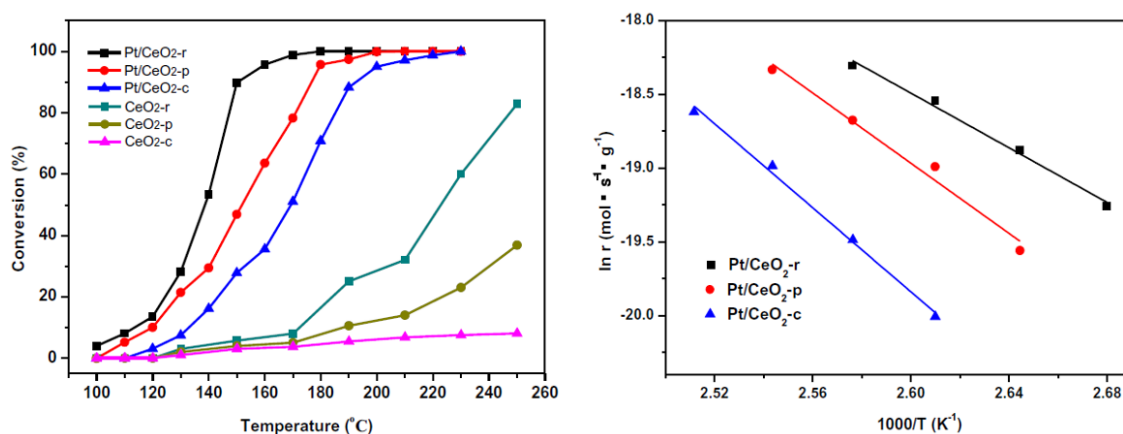
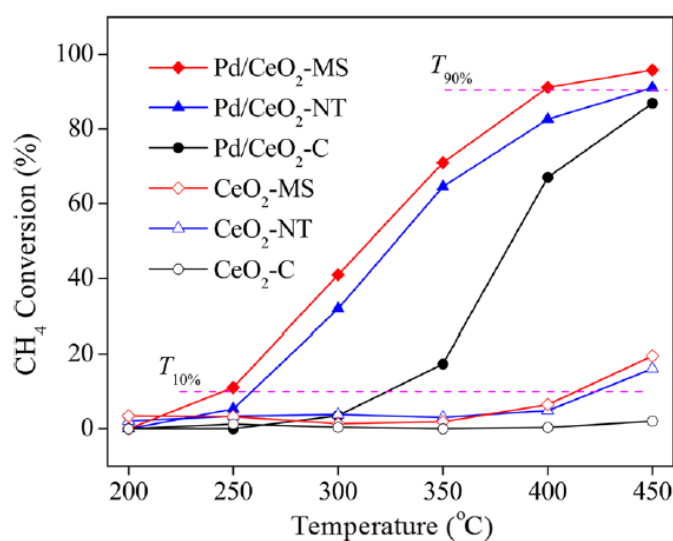


**Figure 8.14:** Toluene conversion on CeO<sub>2</sub> and Pt/CeO<sub>2</sub> nanoshapes (on the left) and the Arrhenius plots (on the right) adapted from ref. [104]

Other studies have also demonstrated that the toluene oxidation is a Pt-size dependent reaction. The average size of several platinum particles have been tested, proving that those particles with a size of 1.8 nm show the best catalytic activity due to a good combination between the amount of oxygen vacancies and the good noble metal dispersion [120].

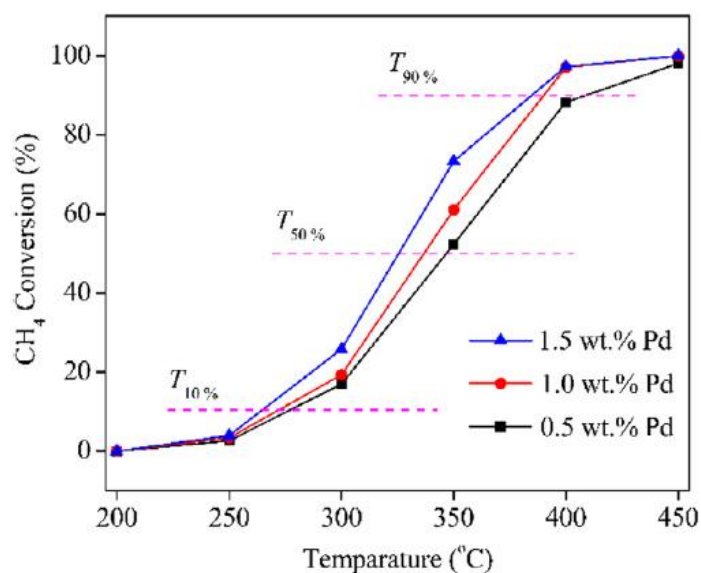
### 8.2.2 Catalytic performance of palladium supported on ceria catalysts

Figure 8.15 shows the methane conversion performed on ceria microstructures impregnated with 0.5 wt% of palladium. The pure ceria samples have shown a low catalytic activity in the temperature range between 200 and 450°C. Instead, the Pd/CeO<sub>2</sub>-microspheres system has demonstrated higher performance compared to the Pd/nanotubes obtaining a T<sub>90%</sub> value of 397°C. Accordingly, it is possible to understand that the ceria morphology can change the activity of the methane oxidation reaction. The highest activity of the microspheres-based system has been attributed to the greater palladium dispersion compared to the other samples. The beneficial role of the (100) planes exposition which characterizes this nanostructure is not less important. Lastly, Raman analyses have proved higher defect sites and oxygen vacancies content on the microspheres compared to the ceria nanotubes [114].



**Figure 8.15:** Methane conversion on different Pd/ceria structures from ref. [114]

Lamellar octahedra ceria (LOC) synthesised through the hydrothermal technique has proved good performance in the catalytic oxidation of methane due to its peculiar structure and the high exposition of (110) planes. As illustrated in Figure 8.16, the CH<sub>4</sub> conversion increases with increasing the palladium content in the samples. Nevertheless, the catalytic activity of 1 wt% becomes equal to that of the material containing 1.5 wt% at a temperature higher than 400°C. These catalysts have also demonstrated good stability over time [115].



**Figure 8.16:** Methane conversion on lamellar octahedra ceria characterized by different Pd contents from ref. [115]

The zirconium addition in the LOC structure can improve its catalytic features, especially those concerning the low-concentration methane emissions. A significant point to take into account is that the zirconium content shall be such as to improve the catalytic properties of the system, but its quantity should not be too high to avoid a weaker palladium-ceria interaction and a significant decrease of the redox-active sites useful for the oxidation reaction [115].

The palladium(5 wt%)-ceria(5 wt%)-alumina catalysts synthesised through the SCS technique have proved a superior activity concerning the methane oxidation compared to the samples obtained via the traditional impregnation method. The CH<sub>4</sub> decomposition rate of the SCS-materials, evaluated at 550°C, is about 18 times higher than that recorded for the impregnation samples. The palladium-alumina catalyst (5P-I in Figure 8.17) shows a decrease in activity at high temperature which could be attributed to the decomposition of the PdO active phase. It should be noted that the addition of ceria provides a positive effect on the system. On the other hand, the latter can improve the stability of the samples. Indeed, the palladium-ceria catalyst synthesised through the wet impregnation procedure (5P5C-I in Figure 8.17) does not exhibit an activity reduction at high temperature. Nevertheless, these samples are characterized by a very high light-off temperature. The palladium-ceria-alumina catalysts prepared via the SCS technique show much greater activity than the other and their T<sub>90%</sub> value is lower compared to the light-off temperature of the impregnation materials. This fact is due to the good interaction between the Pd and the Ce species with the formation of the Pd-O-Ce solid solution which facilitates the creation of oxygen vacancies. Additionally, the core-shell type structure avoids the catalyst deactivation [116].

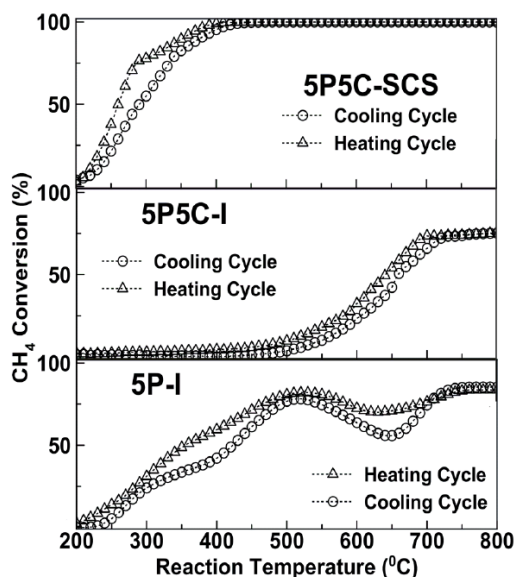


**Figure 8.17:** Methane conversion on Pd-Al<sub>2</sub>O<sub>3</sub> (5P-I) and Pd-CeO<sub>2</sub>-Al<sub>2</sub>O<sub>3</sub> (5P5C-I) obtained through the impregnation method and Pd-CeO<sub>2</sub>-Al<sub>2</sub>O<sub>3</sub> (5P5C-SCS) prepared via the SCS technique adapted from ref. [116]

The catalyst synthesised through the sophisticated ball-milling methods provides excellent features in the methane oxidation when starting from palladium nanoparticles. Instead, using PdO-NPs, the catalytic activity appears lower, as illustrated in Figure 8.18. Despite this, the milling procedure enables to obtain a high-performance catalyst for the methane oxidation characterized by higher activity than that prepared via the SCS and the wet impregnation methods. The reaction rate of the catalyst is indeed 6 and 2 times greater than that obtained through the wet impregnation and SCS procedures, respectively. The successful results may be due to the formation of the amorphous solid solution around the ceria particles. The latter, as proved by experimental analyses, increases the number of vacancies and the chemical disorder which are fundamental in the catalysis field. In addition, the strong interaction between the palladium and the ceria domains allows the formation of a solid solution between these two species improving the catalytic performance of the system. Lastly, even the milling parameters play an important role in the reaction: the catalytic activity decreases by increasing the mixing intensity [117].

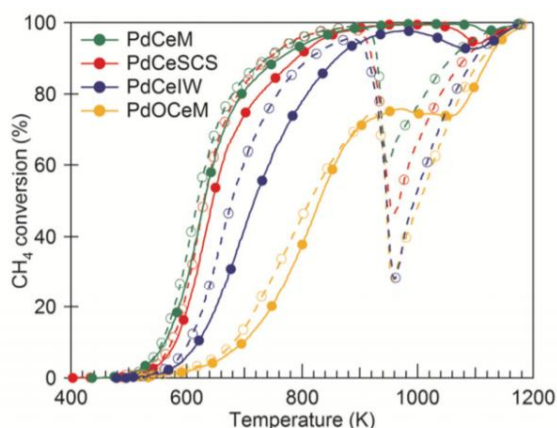


**Figure 8.18:** Methane conversion on ball-milling, wet impregnation and SCS palladium-ceria catalysts from ref. [117]

The presence of water, especially at low temperature, can inhibit the methane conversion on Pd-based catalysts. The water and the methane molecules chemisorb on PdO active sites through a competitive mechanism and the interaction between H<sub>2</sub>O and the palladium active sites lead to the formation of Pd(OH)<sub>2</sub> groups on the catalyst surface [121]. FTIR analyses have shown that the surface coverage caused by the adsorption of hydroxyl groups also depends on the type of supports at a temperature lower than 450°C. The accumulation of these species reduces the oxygen mobility in the catalytic structure and decreases the number of active sites available to the methane molecules causing a drop in the catalytic activity [122].

The inhibition effect and the reduction of the catalytic performance are very pronounced performing the oxidation of methane on samples prepared through the palladium impregnation on different supports, including the ceria. However, this negative impact appears to be limited when using advanced synthesis techniques which allow the production of catalysts with a strong interaction between the palladium species and the cerium oxide [110]. In this respect, as referred to above, the core-shell structures have proved a greater catalytic activity and greater thermal stability compared to the other samples, avoiding the typical PdO-Pd transition at high temperature. In any case, it should be taken into account that, according to other researches, the methane oxidation on these structures also depends on the presence of water. The phenomenon turns out less pronounced at a temperature lower than 500°C. This temperature range is indeed characterized by the competitive adsorption of methane and water molecules on the active sites of the catalysts. On the contrary, at a higher temperature, the formation of hydroxyl groups causes a drop of the catalytic activity [121].

In conclusion, broadly speaking, the presence of water progressively decreases the catalytic performance of the different systems, including the most advanced ones.

## 9. Reaction mechanisms

### 9.1 CO oxidation

#### 9.1.1 Reaction mechanism of CO oxidation on praseodymium oxides

In-situ IR spectroscopy measurements in a heatable reaction cell allow the identification of the different species formed on the samples providing all the information necessary to understand the oxidation reaction mechanism of CO. In the carbon monoxide oxidation, CO does not interact with the praseodymium cations but directly with the lattice oxygen allowing the formation of bidentate carbonates on the surface of the catalytic samples, as shown in Figure 9.1. These species are transformed into monodentate carbonates with the creation of simultaneous oxygen vacancies; therefore, the reaction follows a Mars van Krevelen mechanism. Moreover, monodentate compounds have not been detected in IR spectra due to their quick conversion to carbon dioxide [80].

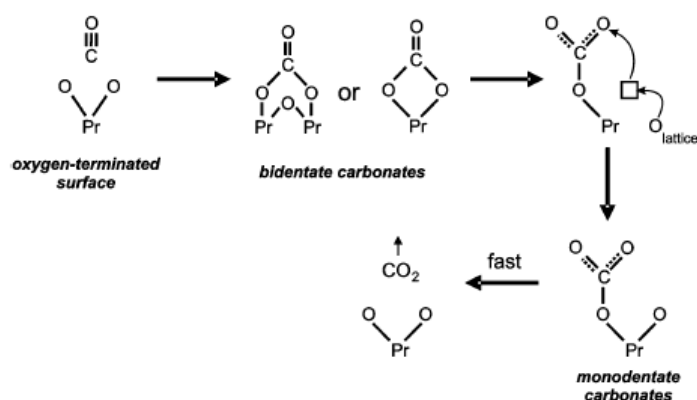


**Figure 9.1:** CO oxidation mechanism on praseodymium oxides from ref. [80]

#### 9.1.2 Reaction mechanism of CO oxidation on ceria catalysts

The CO-TPR analysis combined with the Raman and IR spectroscopy enables the study of the CO oxidation reaction mechanism on the three ceria nanoshapes. In this regard, it has been observed that the conversion of CO into carbon dioxide can follow different competitive pathways [123]. In particular, one of these is the reaction between the CO and the surface -OH groups according to the water-gas shift type reactions described in Equations (9.1) and (9.2).



This reaction mechanism is confirmed by monitoring the H<sub>2</sub> production during the CO-TPR test (Figure 85). The hydrogen formation is detected on all the three nanoshapes in a temperature range between 377 and 577°C. The interaction between the -OH surface groups and the CO is also proved by the IR spectroscopy. Figure 9.2 shows indeed the presence of the characteristic bands at 2965, 2932 and 2842 cm<sup>-1</sup> assigned to the presence of formate species [123].

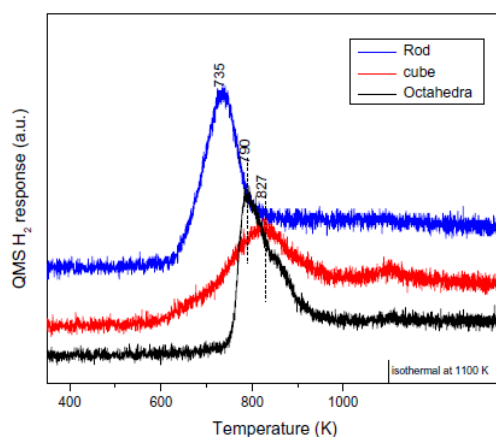


**Figure 9.2:** H<sub>2</sub> evolution during the CO-TPR test adapted from ref. [123]

The second investigated reaction mechanism concerns the interplay between the CO and the surface lattice oxygens through the Mars van Krevelen mechanism explained in Equation (9.3).



This mechanism is confirmed by the IR spectra in Figure 9.3. First of all, the bands at medium and high temperature in the region of 2500 and 2000 cm<sup>-1</sup> are due to the presence of Ce<sup>3+</sup> species on the ceria surface. The latter are an indication of the oxygen vacancies formation due to the loss of surface oxygens combined with the Ce<sup>4+</sup>/Ce<sup>3+</sup> transition. Accentuate peaks are also observed in the carbonate region between 2000 and 800 cm<sup>-1</sup> with the development of different surface-bound compounds [123]:

- Bridget carbonates (peaks around 1030, 1122, 1270 and 1690 cm<sup>-1</sup>)
- Bidentate carbonates (peaks around 1024, 1280 and 1650 cm<sup>-1</sup>)
- Unidentate carbonates (peaks around 1400 and 1580 cm<sup>-1</sup>)

In any case, the nano-octahedra spectrum is much flatter than that of nanocubes and nanorods which instead exhibit very similar formed species.

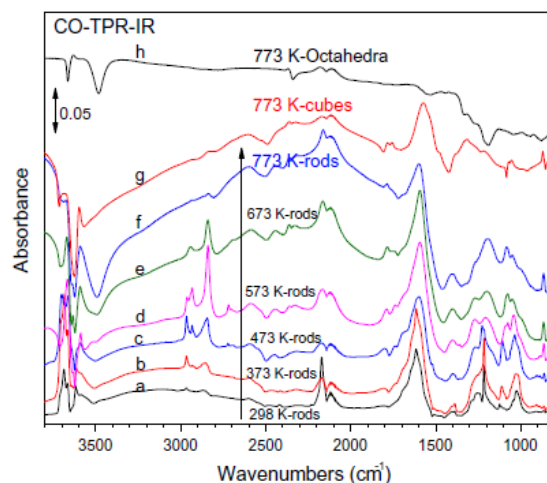


**Figure 9.3:** IR spectra performed during the CO-TPR on ceria nanoshapes at different temperature from ref. [123]

As seen above, the IR spectra of ceria nanocubes and nanorods are very similar, therefore, the same result is expected to be observed in the Raman spectroscopy analysis (Figure 9.4). However, during the CO-TPR test, the nanorods spectrum exhibits two bands centred at 1350 and 1600  $\text{cm}^{-1}$  which are not present on the other samples [123]. Consequently, treating this sample with helium and oxygen in helium, it is possible to prove the presence of a new different reaction mechanism which takes place only on ceria nanorods; it has to do with the CO disproportionation or Boudouard reaction described in Equation (9.4).



More specifically, considering that the carbonates species are characterized by equal stability in helium and oxygen, the disappearance of the two pronounced bands in the region between 1300 and 1600  $\text{cm}^{-1}$  is an indication of the formation of carbonaceous species, as shown in Equation (9.4).

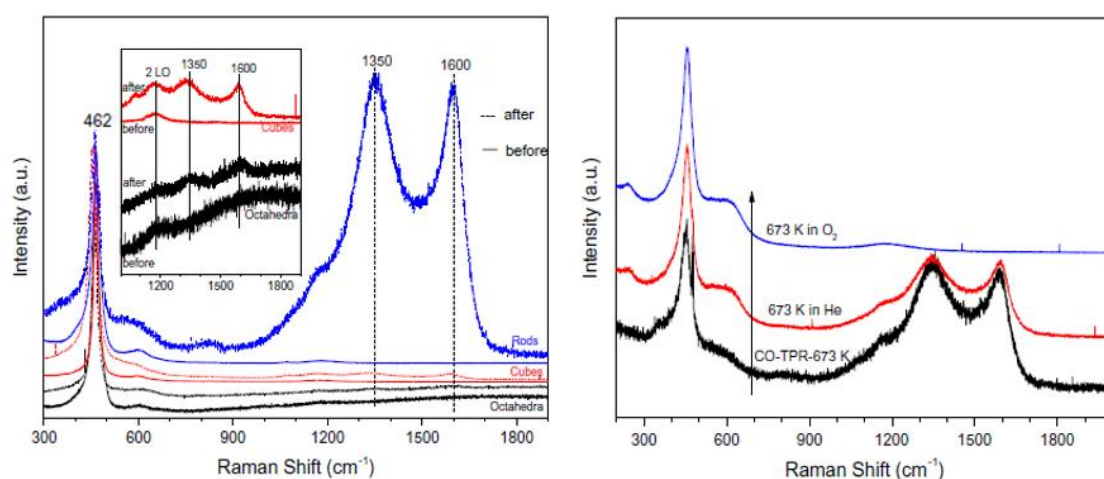


**Figure 9.4:** Raman spectra performed during the CO-TPR at 400°C on the three nanoshapes (on the left) and after a flux of helium and O<sub>2</sub> in helium at 400°C on rods (on the right) adapted from ref. [123]

## 9.2 Soot oxidation

### 9.2.1 Reaction mechanism of soot oxidation on ceria catalysts

It is now clear that the particulate matter is a complex matrix which mainly consists of carbon, hydrogen, nitrogen, ash and a small amount of sulfur. Therefore, before outlining the soot reaction mechanism on ceria catalysts, it is important to better characterize this compound. Figure 9.5 illustrates the FTIR spectrum of the soot studied in a KBr pressed disk.

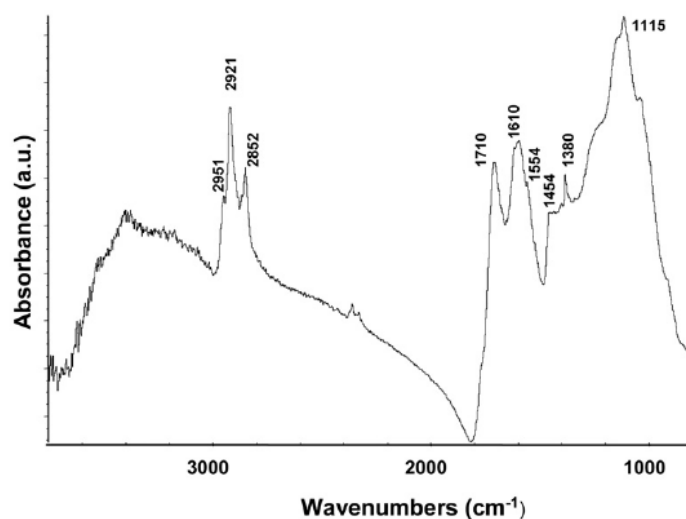


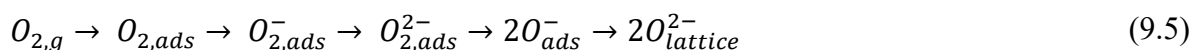
**Figure 9.5:** FTIR spectrum of soot[124]

Interestingly, no bands are detected between 3000 and 3100  $\text{cm}^{-1}$ , and consequently, soot does not contain aromatic compounds due to their probable breaking into the combustion chamber. Moreover, the large band centred at 3400  $\text{cm}^{-1}$  is associated with the stretching of the O-H group. For the sake of brevity, Table 9.1 shows the most important bands observed in the IR spectrum [124].

**Table 9.1:** Most important bands observed in the IR spectrum adapted from ref. [124]

IR band $\text{cm}^{-1}$	Assignment of peaks
2921	C-H asymmetric stretching in methylene groups
2951 and 2852	C-H asymmetric and symmetric stretching in methyl groups
1710	C=O stretching
1115	C-O/C-C stretching
1610	H-O-H bending
1554 and 1435	COO asymmetric and symmetric stretching
1454 and 1380	H-C-H asymmetric and symmetric bending

In summary, the particulate matter is constituted by hydrocarbons, carboxylic species, methylene and methyl groups. Thus, now it is possible to investigate the soot oxidation mechanism. In this regard, the catalytic combustion of soot on CeO<sub>2</sub> catalysts shows a Mars-van Krevelen type mechanism [60], [125]. Soot reacts directly with the surface lattice oxygens of the ceria producing CO<sub>2</sub> along with the formation of oxygen vacancies. Another phenomenon is observed: the formation of peroxide and superoxide surface species due to the reaction between the gaseous oxygen with the oxygen vacancies, according to the scheme illustrated in Equation (9.5) [60], [125], [126]. This active oxygen can reach (spillover phenomenon) and react with soot particles achieving a better performance in the oxidation process.



The scheme above is also the mechanism of the CeO<sub>2-x</sub> re-oxidation. Therefore, an excessive number of oxygen vacancies can easily form surface lattice oxygen instead of peroxide and superoxide species which are the most active players in the soot oxidation reaction [56].

Figure 9.6 summarizes the soot oxidation process on ceria catalysts in six fundamentals steps [125]:

- Interaction between the soot and the ceria surface
- Reaction between the soot and the surface oxygens with the formation of carbon dioxide and oxygen vacancies associate to the Ce<sup>4+</sup> to Ce<sup>3+</sup> redox transition according to the Mars van Krevelen mechanism
- Reaction between the gaseous oxygen and the oxygen vacancies
- Partial re-oxidation of the ceria surface with the formation of active peroxide and superoxide species
- Spillover phenomenon of the active species onto the soot particles
- Reaction between the soot and peroxide and superoxide active species combined with the formation of CO<sub>2</sub>

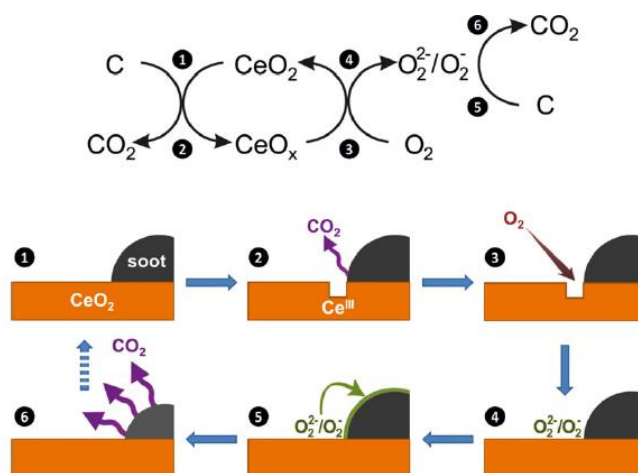


**Figure 9.6:** Soot oxidation mechanism on ceria catalysts from ref. [125]

Another important studied phenomenon concerning the particulate oxidation mechanism is the activation of soot particles into reactive radical cation intermediates, easily oxidized by oxygen species due to the presence of acid sites on the catalyst surface, as described in Figure 9.7. However, in literature, a complete explanation of this fact does not exist yet [101], [127].



**Figure 9.7:** Role of acid sites in the soot oxidation reaction on ceria catalysts from ref. [101]

### 9.2.2 Soot oxidation on ceria-praseodymia catalysts in the presence of $\text{NO}_x$ molecules

As seen in section 7.1, the equimolar ceria-praseodymia samples synthesized through the hydrothermal procedure are one of the most efficient catalysts for soot oxidation and the reaction becomes very interesting in the presence of  $\text{NO}_x$  molecules. In this regard, the catalytic combustion of the particulate matter on equimolar Ce-Pr catalysts starts with the oxidation of NO to  $\text{NO}_2$  probably through a Langmuir-Hinshelwood reaction mechanism, as explained in Figure 9.8. The oxygen and the NO molecules are adsorbed on the material surface with the formation of nitrogen dioxide. Subsequently, the  $\text{NO}_2$  re-adsorption is promoted by the equimolar ceria-praseodymia sample with the formation of nitrate species. The latter, depending on the temperature, can leave the catalytic surface with the production of simultaneous reactive oxygen species [128]. To sum up, the soot oxidation can occur in four different ways:

- Interaction between the gaseous oxygen and the soot particles
- Interaction between the gaseous  $\text{NO}_2$  and the soot particles
- Interaction between the adsorbed  $\text{NO}_2$  in the form of nitrates and the soot particles
- Interaction between the reactive oxygen species present on the catalytic surface and the soot particles

These mechanisms are detected by performing the reaction under both “tight” and “loose” conditions, although in the latter situation they are less accentuated. Therefore, it is possible to demonstrate that the equimolar ceria-praseodymia is the highest-performance catalyst for soot oxidation and the  $\text{NO}_x$  molecules act not only as an efficient oxidizing agent, but also as a surface oxygen activator.

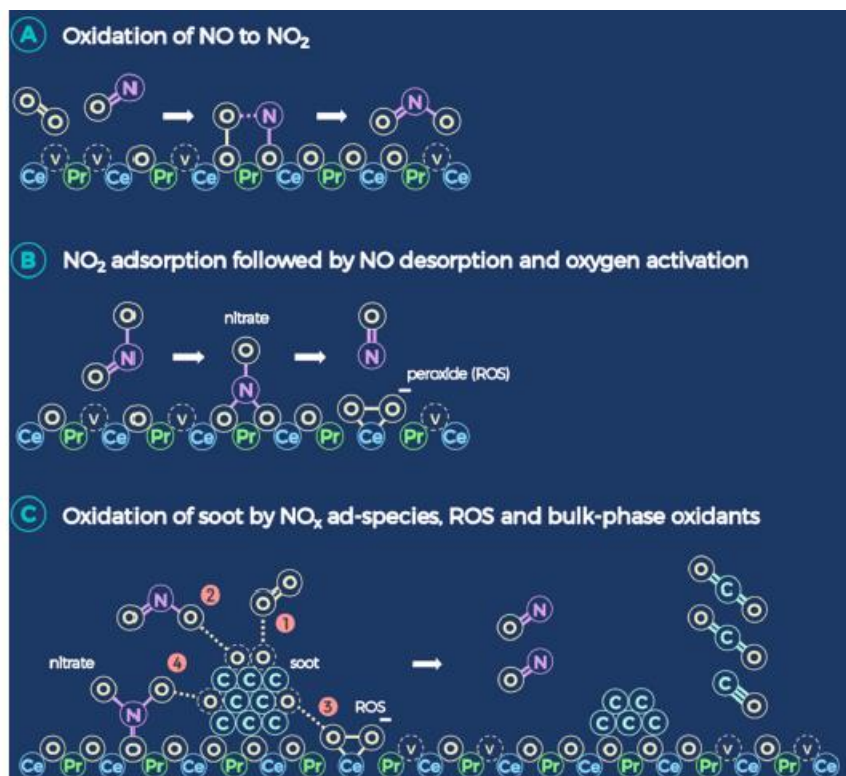


**Figure 9.8:** Soot oxidation mechanism on equimolar ceria praseodymia catalysts in the presence of NO<sub>x</sub> from ref. [128]

Besides enhancing the catalytic activity and the redox properties of the ceria samples, the role of praseodymium is to promote the NO conversion into NO<sub>2</sub>. The latter can be adsorbed on the material surface in the form of nitrates at a temperature lower than 400°C creating active species useful for the soot oxidation reaction. On the contrary, at a higher temperature, they are released in the gaseous phase [91]. Furthermore, as discussed in Section 8.1.2, the presence of platinum can further promote the oxidation of NO, although it does not allow the NO<sub>2</sub> adsorption on the catalyst. Last but not least, platinum substantially improves the CO<sub>2</sub> selectivity. More specifically, the noble metal can easily and quickly oxidize the CO molecules formed during the soot conversion.

In conclusion, Figure 9.9 shows a general overview of the soot oxidation reaction on equimolar ceria-praseodymia samples, in particular, its complexity and its dependency on different parameters such as the presence of noble metals, the interaction between the soot and the NO<sub>x</sub> species, the structure and the shape of the catalyst, as well as its preparation method.

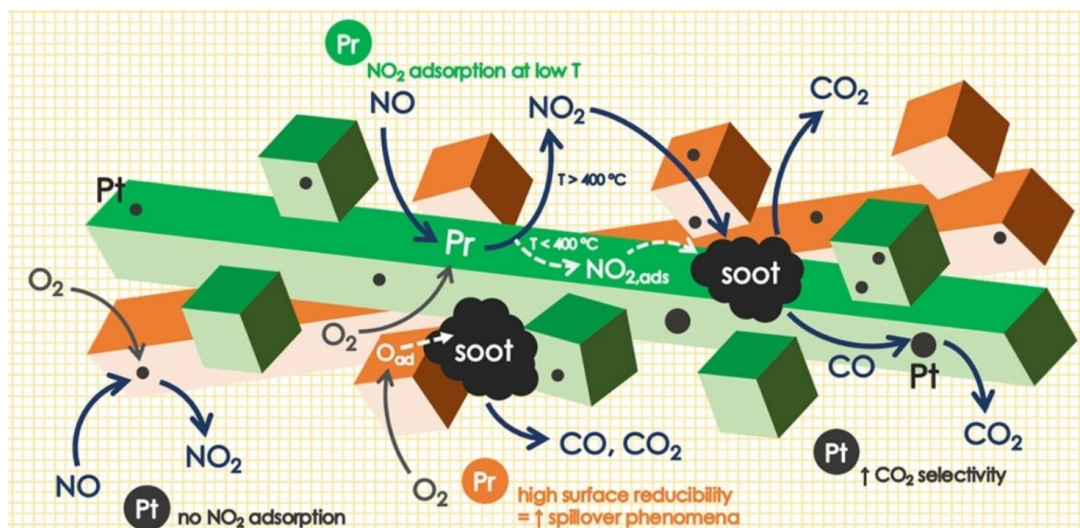


**Figure 9.9:** Complete scheme of the soot oxidation reaction mechanism on equimolar ceria-praseodymia catalysts from ref. [91]

### 9.3 VOCs oxidation

The term Volatile Organic Compounds (VOCs) encloses a large number of substances and generally, it is not possible to summarise their catalytic oxidation in only one way. Their conversion to CO<sub>2</sub> can follow three different routes [12]:

- The Mars van Krevelen mechanism
- The Langmuir-Hinshelwood mechanism
- The Eley-Rideal mechanism

In the first case, the VOCs are adsorbed on the catalyst surface and directly oxidised by the oxygen lattice of the catalytic material. In the second proposed method, both the VOCs and the oxygen adsorb on the active sites of the catalyst surface, whereas in the last case, the reaction takes place between the adsorbed oxygen and the pollutant molecule in the gaseous phase. To provide a broader vision about this topic, the section below discusses the reaction mechanisms relating to the catalytic oxidation of some VOCs.

#### 9.3.1 Toluene oxidation on ceria catalysts

The toluene oxidation follows the Mars van Krevelen mechanism, thus the pollutant reacts directly with the surface oxygens of the catalyst. This process can be supported by a different reaction path which leads to the formation of active oxygen species (peroxides and superoxides) with high oxidizing power [104]. This latter mechanism is described in Equations (9.6), (9.7) and (9.8).



More specifically, the toluene is adsorbed on the platinum nanoparticles with the formation of dehydrogenated intermediates. The reaction between these last and the active

oxygen species occurs at the metal-ceria interface obtaining  $\text{CO}_2$  as a product. As shown in Figure 9.10 the oxygen activation is considered the rate-determining step.

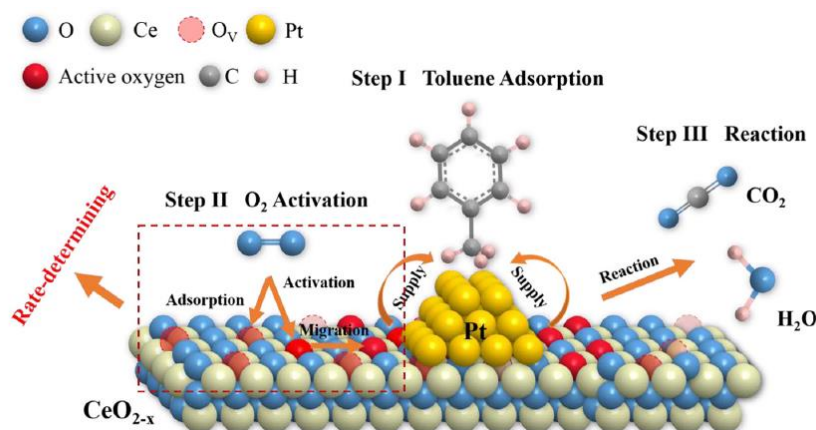


**Figure 9.10:** Toluene oxidation mechanism on Pt/CeO<sub>2</sub> catalysts from ref. [104]

### 9.3.2 CH<sub>4</sub> oxidation on palladium-based catalysts

The detailed description of all the reaction steps of the methane oxidation reaction is quite complicated. As a rule of thumb, several studies have observed that the dissociative adsorption of the methane molecules is the rate-determining step of the process [111], [112], [129]. As previously discussed, the IR spectroscopy is a powerful method to accurately describe the reaction mechanism, examining the stable intermediate species formed on the catalyst surface. This technique has been used to provide a reaction mechanism for the catalytic combustion of methane on palladium-based catalysts supported by  $\gamma\text{-Al}_2\text{O}_3$ . Figure 9.11 explains the reaction mechanism of the studied reaction and the species placed in the rectangles are directly observed in the IR spectra. In the underlying description the PdO has been considered as the active phase of the reaction, although recent research has suggested that the simultaneous presence of metallic Pd and PdO compounds is the most active form concerning the methane combustion [129].

The main steps of the reaction, illustrated in Figure 9.11, are listed below [129]:

- The reaction cycle starts with the palladium oxide indicated as [MeO]
- The oxygen is adsorbed in a dissociative way on the palladium site
- Gaseous methane interacts with the chemisorbed oxygen to produce methoxy and hydroxyl species
- CO and CO<sub>2</sub> can be classified as the products of the reaction by restoring the O\* species with simultaneous adsorption of the water molecules
- The produced CO can subsequently interact with hydroxyls alumina active groups with the formation of formates species
- The water desorption from the palladium site can occur in a simple way and the interaction between the CO and the active oxygen O\* allows the formation of carbon dioxide returning to the starting point of the catalytic cycle
- Monodentate, bidentate and free carbonate groups can be formed as the result of the interaction between the carbon dioxide molecules and the active oxygen O\*, whereas the bicarbonates species are due to the CO<sub>2</sub>-alumina interplay

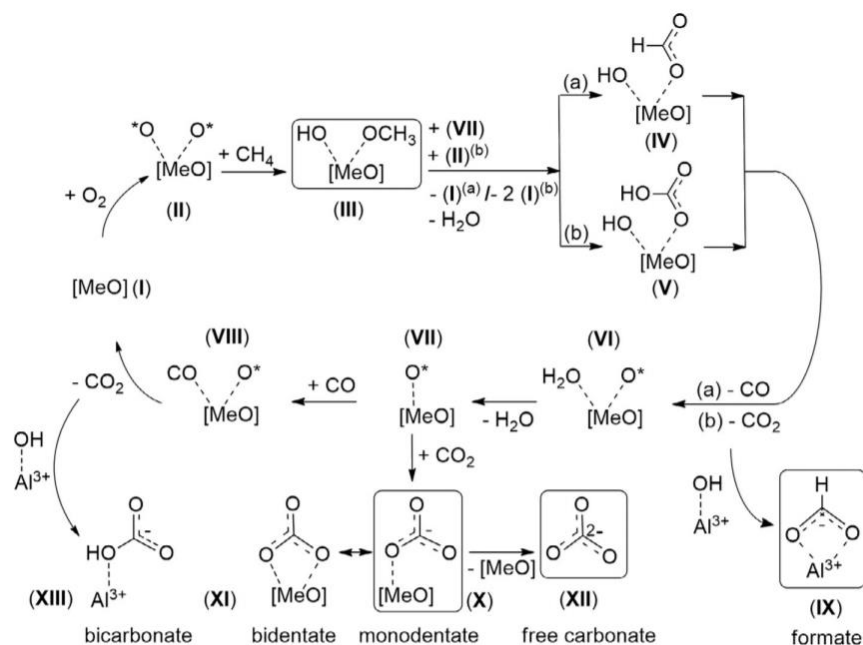


**Figure 9.11:** CH<sub>4</sub> oxidation over palladium-based catalysts from ref. [129]

In the catalytic cycle described above, only monodentate, free carbonate and formate compounds have been observed in the IR spectra. Thus, the IR analysis allows studying the different species formed on the catalyst surface interconnecting the theoretical approach with the experimental evidence.

### 9.3.3 CH<sub>4</sub> oxidation on praseodymium oxides

The interaction between methane and the praseodymium oxides is studied with the IR spectroscopy. Chemisorbed methane is observed on the praseodymia samples only at a temperature above 400°C. The most probable reaction mechanism for the methane oxidation on praseodymium oxides is described in Figure 9.12. In this regard, the interaction between gaseous methane and the surface oxygen allows the formation of methyl radicals in the gas phase and -OH groups on the catalyst. Then, the radical species react with the surface oxygen of the sample causing the formation of monodentate carbonates. Finally, the decomposition of these last allows the formation of carbon dioxide molecules. The abstraction of the hydrogen atom from the methane is considered the rate-determining step. The reaction follows the Mars van Krevelen mechanism, therefore the methyl radicals are oxidized directly by the lattice oxygens of the catalyst [82].

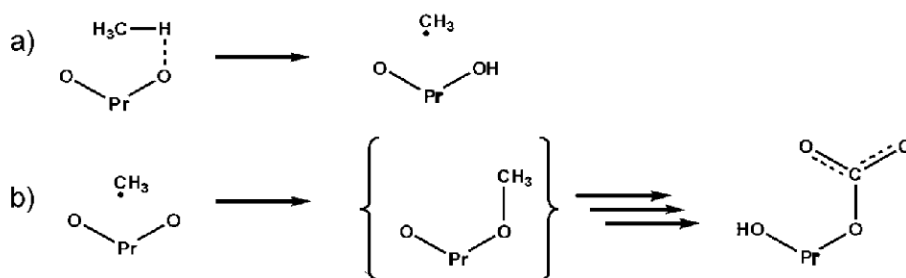


**Figure 9.12:** CH<sub>4</sub> oxidation mechanism on praseodymium oxides from ref. [82]

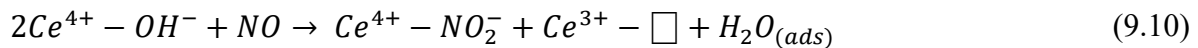
## 9.4 NO oxidation

### 9.4.1 NO oxidation on ceria catalysts

Cerium oxide is an important material for the NO and NO<sub>2</sub> storage. In this respect, IR analyses have shown that the interaction between the NO and the stoichiometric catalyst in the absence of oxygen leads to the NO disproportionation reaction forming symmetric nitrites and hyponitrites [55]. Therefore, according to Equation (9.9), NO seems to react preferentially on the Ce-O sites.



Further studies have proved a possible NO reaction with the surface hydroxides groups of the catalyst with the formation of nitrites and adsorbed water [130], as shown in Equation (9.10).



In the presence of oxygen, hyponitrite and nitrite species quickly disappear and bands due to the presence of ionic, monodentate, bidentate and bridged nitrates start to appear in the IR spectra [55], [130]. The structure and the formation mechanisms of these species are described in Figure 9.13 and Equation (9.11) and (9.12), respectively.

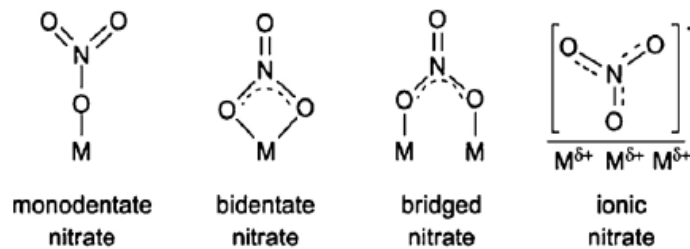
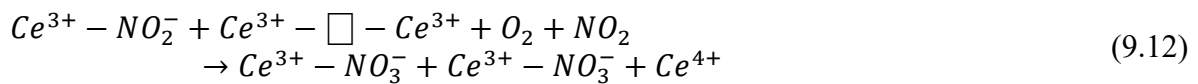
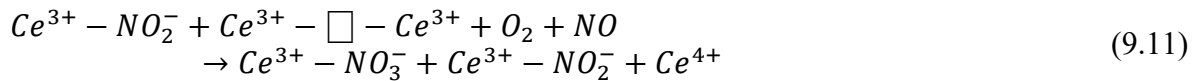


**Figure 9.13:** Illustration of the different nitrate species adapted from ref. [130]

As for the desorption process, nitrite species leave the material surface more easily than the nitrates due to their weak interaction with the catalyst.

The storage/release mechanism of NO<sub>x</sub> species concerning the ceria surface can be used for the NO oxidation reaction. In this context, the most active catalysts for the transformation of NO into NO<sub>2</sub> are the noble metals. The net reaction is described in Equation (9.13) and includes several elementary steps.



With a focus on platinum supported on ceria catalysts, ceria-zirconia samples containing platinum with an oxidation state higher than zero (Pt<sup>x+</sup>) have been studied in order to find the reaction mechanism of the NO oxidation [131]. As shown in Figure 9.14, the active site  $\square Pt^{x+} \square$  allows the dissociative adsorption of the gaseous oxygen on the catalyst forming the OPt<sup>x+</sup>O compound, which in turn can interact with a NO molecule to obtain the OPt<sup>x+</sup>O(NO) species. The decomposition of the latter provides the formation of gaseous NO<sub>2</sub> and a  $\square Pt^{x+} O$  site.

Finally, the renovation of the starting active site is achieved due to the interaction between the  $\square\text{Pt}^{x+}\text{O}$  site and a NO molecule with simultaneous formation of  $\text{NO}_2$ .

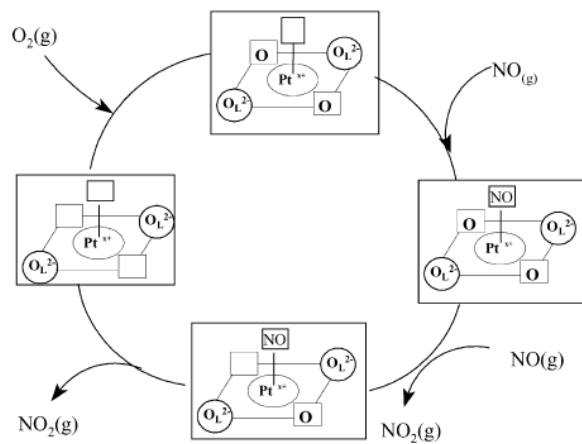


**Figure 9.14:** NO oxidation mechanism on platinum supported on ceria-based catalysts from ref. [131]

## 10. Final discussion and future prospects

Broadly speaking and as widely described in this thesis, ceria-based catalysts and ceria-modified catalysts play a fundamental role in the environmental catalytic field due to their unique and unusual features. Their redox properties and the oxygen storage capacity turn out to be exceptionally important for the Mars van Krevelen mechanism which is one of the most typical reaction mechanisms concerning the oxidation reactions. It has also been proved that the insertion of metallic dopants in the ceria lattice structure improves its characteristics allowing higher oxygen mobility and, consequently, a higher catalytic activity.

Unlike the CO molecule, for which efficient active catalytic systems have been found to promote its oxidation at low temperature, the soot oxidation is still today a great challenge. Despite the considerable efforts carried out by the automotive companies to comply with the stricter and stricter emission limits, a catalyst able to perform the soot oxidation reaction at the diesel exhaust gas temperature has not been synthesised yet. Nowadays, the most active catalyst concerning the particulate abatement is the equimolar ceria-praseodymia prepared through the hydrothermal synthesis. The latter has indeed allowed the obtainment of nanostructured catalysts characterized by peculiar active planes. The soot abatement becomes particularly successful with the exposition of (100) and (110) facets. Unfortunately, the use of noble metals does not seem to improve the catalytic performance of the system. A way to further improve both the activity and the stability of the studied catalysts is to synthesise ceria-praseodymia-zirconia samples with different compositions. In this context, the  $Zr_{0.1}(Ce_{0.5}Pr_{0.5})_{0.9}O_2$  could be the most interesting configuration to obtain a good material. It is also possible to disperse the platinum on the sample and to perform the catalytic test in the presence of  $NO_x$  to achieve the maximum possible conversion. In the search for an active catalyst at the temperature of exhaust gases coming from diesel engines, the equimolar ceria-praseodymia sample could be analysed through a detailed spectroscopic study by combining the advanced Raman and FTIR technologies. In this way, it is possible to examine the defect sites of the catalyst and the amount of the acidic and the basic sites on its surface. Once understood the role of these properties, a new active catalyst could be prepared thanks to their optimal combination. As seen in this work, the presence of praseodymium in the catalytic systems has proved to be a key component for the NO oxidation to  $NO_2$ , which is a particularly active agent for the soot abatement. The role of the praseodymium oxide could be further investigated through an IR analysis to search the effective role of the superficial active species of the sample in the NO oxidation performing the interaction with specific probe molecules.

Given that the term Volatile Organic Compounds (VOCs) encloses a large number of compounds, as a general rule, it is difficult to provide indications for the choice of the best performing catalyst. The case-by-case study of the various systems is essential to find the optimum material for the different oxidation reactions. As presented in this work, the cerium oxide is particularly active for the naphthalene abatement, while the ceria-praseodymia catalysts allow a good methanol conversion at low temperature. Again, the copper-ceria mixed oxides play a fundamental role in the ethene oxidation. On the other side, noble metals own an important role in VOCs removal due to their high intrinsic activity. In this context, the use of noble metals is somewhat inevitable, despite their high cost. Case by case and therefore, molecule by molecule, it is necessary to study the most active support and the best synthesis method to obtain high catalytic performance by using a lower amount of noble metal. In the context of methane oxidation reaction, Pd/ $CeO_2$ -based systems have shown high activity compared to the other materials. Palladium-ceria catalysts synthesised through standard and established techniques have demonstrated lower catalytic performance than the sophisticated,

innovative samples prepared via modern approaches. These latter allow obtaining high-performance material able to maximize both the Ce-Pd interactions and the structure stability. One need only look at the great features described for the core-shell structures and the formation of the peculiar Pd-Ce amorphous phase around the ceria particles in the ball-milling samples. As a general rule, on the one hand it is important to enhance the performance of these techniques but, on the other hand, it would be useful to study new advanced catalytic configurations to further improve CH<sub>4</sub> conversion. In this respect, another key aspect is to determine the real active phase of the reaction at low temperature and then to maximize its presence in the synthesised catalyst. This crucial point could be solved through accurate FTIR analyses trying to fix the different stable reaction intermediates together with the different catalytic active sites on the sample surface obtained by the interaction with specific probe molecules. The last point to consider for the methane oxidation is the high cost of the palladium, especially in the last few years. Eradicating the use of this noble metal is particularly challenging due to its very high activity. In any way, the study of a good-performance system that allows the use of a lower amount of palladium might be an effective choice. According to the various papers read so far, the role of the palladium deposition on ceria-praseodymia samples could be an interesting point to study. The insertion of metallic dopants in the lattice structure of ceria could improve the unique and optimal ceria properties. A good solution could be to study the best technique to prepare these samples and, subsequently, understand the most appropriate composition to obtain the maximum possible conversion at the lowest possible temperature.

## 11. Symbol list

A	Pre-exponential factor ( $s^{-1}$ )
$A_m$	Area occupied by a molecule ( $m^2 \text{ molecule}^{-1}$ )
$A_{IR}$	IR absorption intensity (area in $cm^{-1}$ )
b	Peak width at mid-height (rad)
$C_w$	Acid/base sites concentration ( $mol \text{ kg}^{-1}$ )
d	Lattice spacing (nm)
$E_a$	Activation energy ( $kJ \text{ mol}^{-1}$ )
$E_b$	Binding energy (J)
$E_k$	Kinetic energy (J)
h	Planck constant (J s)
k	Rate coefficient (-)
m	Weight (kg)
n	Order of diffraction (-)
$N_A$	Avogadro number ( $molecule \text{ mol}^{-1}$ )
$n_m$	Monolayer capacity ( $mol \text{ g}^{-1}$ )
p	Reaction order (-)
R	Universal constant of gases ( $kJ \text{ mol}^{-1} \text{ K}^{-1}$ )
S	Disk area ( $cm^2$ )
$S_{BET}$	Specific surface area ( $m^2 \text{ g}^{-1}$ )
T	Temperature (K)
$V_o$	Oxygen vacancy (-)
$\varepsilon$	Molar extinction coefficient ( $cm \text{ mol}^{-1}$ )
$\lambda$	Wavelength of the beam (nm)
$\Theta$	Diffraction angle (rad)
$\nu$	Wave frequency ( $s^{-1}$ )



## 12. References

- [1] “Number of cars sold worldwide between 2010 and 2020 (in million units),” *Statista*. <https://www-statista-com.ezproxy.biblio.polito.it/statistics/200002/international-car-sales-since-1990/> (accessed Jul. 27, 2020).
- [2] E. Genty, C. Bustillo-Lecompte, J. Colina-Márquez, C. Barroo, and R. Cousin, “Editorial: Special issue ‘new concepts in oxidation processes,’” *Catalysts*, vol. 9, no. 11, pp. 5–6, 2019, doi: 10.3390/catal9110878.
- [3] H. Xu *et al.*, “The influence of molar ratios of Ce/Zr on the selective catalytic reduction of NO<sub>x</sub> with NH<sub>3</sub> over Fe<sub>2</sub>O<sub>3</sub>-WO<sub>3</sub>/Ce<sub>x</sub>Zr<sub>1-x</sub>O<sub>2</sub> (0 ≤ x ≤ 1) monolith catalyst,” *Chinese Sci. Bull.*, vol. 59, no. 31, pp. 3956–3965, 2014, doi: 10.1007/s11434-014-0393-4.
- [4] N. K. Soliman, “Factors affecting CO oxidation reaction over nanosized materials: A review,” *J. Mater. Res. Technol.*, vol. 8, no. 2, pp. 2395–2407, 2019, doi: 10.1016/j.jmrt.2018.12.012.
- [5] Ronald M. Heck; Robert J. Farrauto; Suresh T. Gulati, “Volatile Organic Compounds,” in *Catalytic Air Pollution Control: Commercial Technology*, 2016, pp. 377–402.
- [6] B. A. A. L. Van Setten, M. Makkee, and J. A. Moulijn, “Science and technology of catalytic diesel particulate filters,” *Catal. Rev. - Sci. Eng.*, vol. 43, no. 4, pp. 489–564, 2001, doi: 10.1081/CR-120001810.
- [7] R. Prasad and V. R. Bella, “A review on diesel soot emission, its effect and control,” *Bull. Chem. React. Eng. & Catal.*, vol. 5, no. 2, pp. 69–86, 2010, doi: 10.9767/bcrec.5.2.794.69-86.
- [8] O. Deutschmann and A. G. Konstandopoulos, *Catalytic Technology for Soot and Gaseous Pollution Control*, vol. 2, no. x. 2010.
- [9] C. Pisac, R. Calay, Y. Chen, and S. Ahmed, “Comparative study of NO<sub>x</sub> formation from biodiesel and diesel,” *Innov. Fuel Econ. Sustain. Road Transp.*, pp. 109–120, 2011, doi: 10.1533/9780857095879.
- [10] “Emission standards,” *DieselNet*. <https://dieselnet.com/standards/> (accessed Jul. 25, 2020).
- [11] “Council Directive 1999/13/EC of 11 March 1999 on the limitation of emissions of volatile organic compounds due to the use of organic solvents in certain activities and installations,” <https://eur-lex.europa.eu/legal-content/EN/ALL/?uri=CELEX:31999L0013> (accessed Aug. 06, 2020).
- [12] M. S. Kamal, S. A. Razzak, and M. M. Hossain, “Catalytic oxidation of volatile organic compounds (VOCs) - A review,” *Atmos. Environ.*, vol. 140, pp. 117–134, 2016, doi: 10.1016/j.atmosenv.2016.05.031.
- [13] S. Ojala *et al.*, “Catalysis in VOC abatement,” *Top. Catal.*, vol. 54, no. 16–18, pp. 1224–1256, 2011, doi: 10.1007/s11244-011-9747-1.
- [14] D. Fino, “Diesel emission control: Catalytic filters for particulate removal,” *Sci. Technol. Adv. Mater.*, vol. 8, no. 1–2, pp. 93–100, 2007, doi: 10.1016/j.stam.2006.11.012.
- [15] A. S. Ayodhya and K. G. Narayanappa, “An overview of after-treatment systems for diesel engines,” *Environ. Sci. Pollut. Res.*, vol. 25, no. 35, pp. 35034–35047, 2018, doi: 10.1007/s11356-018-3487-8.

- [16] J. O'Connor and M. Musculus, "Post injections for soot reduction in diesel engines: A review of current understanding," *SAE Int. J. Engines*, vol. 6, no. 1, pp. 400–421, 2013, doi: 10.4271/2013-01-0917.
- [17] H. Lakhiani, J. Barman, K. Rajput, and A. Goswami, "Experimental study of EGR mixture design and its influence on EGR distribution across the cylinder for NO<sub>x</sub> - PM tradeoff," *SAE Tech. Pap.*, vol. 12, 2013, doi: 10.4271/2013-01-2743.
- [18] W. Tang, D. Youngren, M. M. Santa, and S. Kumar, "On-engine investigation of SCR on filters (SCRoF) for HDD passive applications," *SAE Int. J. Engines*, vol. 6, no. 2, pp. 862–872, 2013, doi: 10.4271/2013-01-1066.
- [19] V. Vrabie, D. Scarpete, and O. Zbarcea, "The New Exhaust Aftertreatment System for Reducing NO<sub>x</sub> Emissions of Diesel Engines : Lean NO<sub>x</sub> Trap ( LNT ). a Study," *Sci. Proc. XXIV Int. Sci. Conf. "Trans MOTAUTO '16,"* vol. 1, no. 2, pp. 110–113, 2016.
- [20] A. Bueno-López, "Diesel soot combustion ceria catalysts," *Appl. Catal. B Environ.*, vol. 146, pp. 1–11, 2014, doi: 10.1016/j.apcatb.2013.02.033.
- [21] Z. Hong, Z. Wang, and X. Li, "Catalytic oxidation of nitric oxide (NO) over different catalysts: An overview," *Catal. Sci. Technol.*, vol. 7, no. 16, pp. 3440–3452, 2017, doi: 10.1039/c7cy00760d.
- [22] B. A. Tichenor and M. A. Palazzolo, "Destruction of volatile organic compounds via catalytic incineration," *Environ. Prog.*, vol. 6, no. 3, pp. 172–176, 1987, doi: 10.1002/ep.670060328.
- [23] L. F. Liotta, "Catalytic oxidation of volatile organic compounds on supported noble metals," *Appl. Catal. B Environ.*, vol. 100, no. 3–4, pp. 403–412, 2010, doi: 10.1016/j.apcatb.2010.08.023.
- [24] P. Marécot, A. Fakche, B. Kellali, G. Mabilon, P. Prigent, and J. Barbier, "Propane and propene oxidation over platinum and palladium on alumina: Effects of chloride and water," *Appl. Catal. B, Environ.*, vol. 3, no. 4, pp. 283–294, 1994, doi: 10.1016/0926-3373(94)00003-4.
- [25] M. Paulis, H. Peyrard, and M. Montes, "Influence of chlorine on the activity and stability of Pt/Al<sub>2</sub>O<sub>3</sub> catalysts in the complete oxidation of toluene," *J. Catal.*, vol. 199, no. 1, pp. 30–40, 2001, doi: 10.1006/jcat.2000.3146.
- [26] E. Finocchio *et al.*, "Study of the abatement of VOC over V<sub>2</sub>O<sub>5</sub>-WO<sub>3</sub>-TiO<sub>2</sub> and alternative SCR catalysts," *Catal. Today*, vol. 59, no. 3, pp. 261–268, 2000, doi: 10.1016/S0920-5861(00)00292-3.
- [27] S. C. Kim and W. G. Shim, "Catalytic combustion of VOCs over a series of manganese oxide catalysts," *Appl. Catal. B Environ.*, vol. 98, no. 3–4, pp. 180–185, 2010, doi: 10.1016/j.apcatb.2010.05.027.
- [28] Q. Dai, X. Wang, and G. Lu, "Low-temperature catalytic destruction of chlorinated VOCs over cerium oxide," *Catal. Commun.*, vol. 8, no. 11, pp. 1645–1649, 2007, doi: 10.1016/j.catcom.2007.01.024.
- [29] Q. Dai, X. Wang, and G. Lu, "Low-temperature catalytic combustion of trichloroethylene over cerium oxide and catalyst deactivation," *Appl. Catal. B Environ.*, vol. 81, no. 3–4, pp. 192–202, 2008, doi: 10.1016/j.apcatb.2007.12.013.
- [30] G. Leofanti, G. Tozzola, M. Padovan, G. Petrini, S. Bordiga, and A. Zecchina, "Catalyst characterization: Characterization techniques," *Catal. Today*, vol. 34, no. 3–4, pp. 307–

- 327, 1997, doi: 10.1016/S0920-5861(96)00056-9.
- [31] M. Thommes *et al.*, “Physisorption of gases, with special reference to the evaluation of surface area and pore size distribution (IUPAC Technical Report),” *Pure Appl. Chem.*, vol. 87, no. 9–10, pp. 1051–1069, 2015, doi: 10.1515/pac-2014-1117.
- [32] F. Ambroz, T. J. Macdonald, V. Martis, and I. P. Parkin, “Evaluation of the BET Theory for the Characterization of Meso and Microporous MOFs,” *Small Methods*, vol. 2, no. 11, p. 1800173, 2018, doi: 10.1002/smt.201800173.
- [33] A. F. Lee, C. M. A. Parlett, and K. Wilson, “Temperature Programmed Techniques,” *R. Soc. Chem.*, 2017.
- [34] C. Pirola, F. Galli, and G. S. Patience, “Experimental methods in chemical engineering: Temperature programmed reduction—TPR,” *Can. J. Chem. Eng.*, vol. 96, no. 11, pp. 2317–2320, 2018, doi: 10.1002/cjce.23317.
- [35] B. Azambre *et al.*, “Effects of a Pt/Ce<sub>0.68</sub>Zr<sub>0.32</sub>O<sub>2</sub> catalyst and NO<sub>2</sub> on the kinetics of diesel soot oxidation from thermogravimetric analyses,” *Fuel Process. Technol.*, vol. 92, no. 3, pp. 363–371, 2011, doi: 10.1016/j.fuproc.2010.09.029.
- [36] R. A. Van Santen, *Catalysis: An Integrated Approach*, vol. 123. 1999.
- [37] J. V. Sanders, “Transmission electron microscopy of catalysts,” *J. Electron Microsc. Tech.*, vol. 3, no. 1, pp. 67–93, 1986, doi: 10.1002/jemt.1060030108.
- [38] W. H. Thomas N. Otto and E. D. and M. Zimmermann, “Catalyst Characterization with FESEM / EDX by the Example of Silver-Catalyzed,” *Scanning Electron Microsc. Ed.*, p. 392, 2012.
- [39] E. Stavitski and B. M. Weckhuysen, “Infrared and Raman imaging of heterogeneous catalysts,” *Chem. Soc. Rev.*, vol. 39, no. 12, pp. 4615–4625, 2010, doi: 10.1039/c0cs00064g.
- [40] J. Epp, *X-Ray Diffraction (XRD) Techniques for Materials Characterization*. Elsevier Ltd, 2016.
- [41] R. Smith, “Surface characterisation of heterogeneous catalysts by XPS: Part I,” *Platin. Met. Rev.*, vol. 53, no. 1, pp. 55–56, 2009, doi: 10.1595/147106709X398997.
- [42] I. Chorkendorff and J. W. Niemantsverdriet, *Catalyst Characterization*. 2003.
- [43] Z. Xu *et al.*, “Topic review: Application of Raman spectroscopy characterization in micro/nano-machining,” *Micromachines*, vol. 9, no. 7, 2018, doi: 10.3390/mi9070361.
- [44] P. Larkin, *Infrared and Raman Spectroscopy: Principles and Spectral Interpretation*. 2011.
- [45] D.-W. Sun, “Principles of Infrared Spectroscopy,” in *Infrared Spectroscopy for Food Quality Analysis and Control.*, 2009, pp. 3–27.
- [46] J. B. Peri, “Infrared Spectroscopy in Catalytic Research,” in *Catalysis: Science and Technology*, vol. 5, 1984, pp. 171–220.
- [47] T. R. R. Cozzi and P. Protti, “Spettrofotometria infrarossa,” in *Analisi chimica moderni metodi strumentali*, 1987, pp. 343–422.
- [48] D.-W. Sun, “Fourier Transform Infrared (FTIR) Spectroscopy,” in *Infrared Spectroscopy for Food Quality Analysis and Control.*, 2009, pp. 145–178.
- [49] P. Larkin, “Instrumentation and Sampling Methods,” in *Infrared and Raman*

*Spectroscopy*, 2011, pp. 27–54.

- [50] G. Busca, “Spectroscopic characterization of the acid properties of metal oxide catalysts,” *Catal. Today*, vol. 41, no. 1–3, pp. 191–206, 1998, doi: 10.1016/S0920-5861(98)00049-2.
- [51] M. Tamura, K. I. Shimizu, and A. Satsuma, “Comprehensive IR study on acid/base properties of metal oxides,” *Appl. Catal. A Gen.*, vol. 433–434, pp. 135–145, 2012, doi: 10.1016/j.apcata.2012.05.008.
- [52] “Demand for rare earth oxides worldwide in 2019 and 2025 by end use (in metric tons),” *Statista*. <https://www-statista-com.ezproxy.biblio.polito.it/statistics/449722/rare-earth-estimated-demand-globally-by-application/> (accessed Aug. 04, 2020).
- [53] “Distribution of rare earth consumption value worldwide in 2018, by element,” *Statista*. <https://www-statista-com.ezproxy.biblio.polito.it/statistics/1060440/rare-earth-consumption-worldwide-by-element/> (accessed Aug. 04, 2020).
- [54] A. Trovarelli, C. De Leitenburg, M. Boaro, and G. Dolcetti, “The utilization of ceria in industrial catalysis,” *Catal. Today*, vol. 50, no. 2, pp. 353–367, 1999, doi: 10.1016/S0920-5861(98)00515-X.
- [55] M. Y. Mihaylov, E. Z. Ivanova, G. N. Vayssilov, and K. I. Hadjiivanov, “Revisiting ceria-NO<sub>x</sub> interaction: FTIR studies,” *Catal. Today*, no. December 2018, 2019, doi: 10.1016/j.cattod.2019.05.014.
- [56] P. Li, X. Chen, Y. Li, and J. W. Schwank, “A review on oxygen storage capacity of CeO<sub>2</sub>-based materials: Influence factors, measurement techniques, and applications in reactions related to catalytic automotive emissions control,” *Catal. Today*, vol. 327, no. February 2018, pp. 90–115, 2019, doi: 10.1016/j.cattod.2018.05.059.
- [57] U. Hennings and R. Reimert, “Investigation of the structure and the redox behavior of gadolinium doped ceria to select a suitable composition for use as catalyst support in the steam reforming of natural gas,” *Appl. Catal. A Gen.*, vol. 325, no. 1, pp. 41–49, 2007, doi: 10.1016/j.apcata.2007.02.054.
- [58] T. Kanazawa *et al.*, “Development of three-way catalyst using composite alumina-ceria-zirconia,” *SAE Tech. Pap.*, no. 724, 2003, doi: 10.4271/2003-01-0811.
- [59] A. Suda *et al.*, “Effect of specific surface area of ceria-zirconia solid solutions on their oxygen storage capacity,” *J. Ceram. Soc. Japan*, vol. 112, no. 1311, pp. 581–585, 2004, doi: 10.2109/jcersj.112.581.
- [60] A. Trovarelli and J. Llorca, “Ceria Catalysts at Nanoscale: How Do Crystal Shapes Shape Catalysis?,” *ACS Catal.*, vol. 7, no. 7, pp. 4716–4735, 2017, doi: 10.1021/acscatal.7b01246.
- [61] M. V. Ganduglia-Pirovano, A. Hofmann, and J. Sauer, “Oxygen vacancies in transition metal and rare earth oxides: Current state of understanding and remaining challenges,” *Surf. Sci. Rep.*, vol. 62, no. 6, pp. 219–270, 2007, doi: 10.1016/j.surfrep.2007.03.002.
- [62] Z. Wu, A. K. P. Mann, M. Li, and S. H. Overbury, “Spectroscopic investigation of surface dependent acid base property of ceria nanoshapes,” *J. Phys. Chem. C*, vol. 119, no. 13, pp. 7340–7350, 2015, doi: 10.1021/acs.jpcc.5b00859.
- [63] K. Zhou and Y. Li, “Catalysis based on nanocrystals with well-defined facets,” *Angew. Chemie - Int. Ed.*, vol. 51, no. 3, pp. 602–613, 2012, doi: 10.1002/anie.201102619.
- [64] J. Zhang, S. Ohara, M. Umetsu, T. Naka, Y. Hatakeyama, and T. Adschiri, “Colloidal

- ceria nanocrystals: A tailor-made crystal morphology in supercritical water,” *Adv. Mater.*, vol. 19, no. 2, pp. 203–206, 2007, doi: 10.1002/adma.200600964.
- [65] Q. Yuan, H. H. Duan, L. Le Li, L. D. Sun, Y. W. Zhang, and C. H. Yan, “Controlled synthesis and assembly of ceria-based nanomaterials,” *J. Colloid Interface Sci.*, vol. 335, no. 2, pp. 151–167, 2009, doi: 10.1016/j.jcis.2009.04.007.
- [66] T. J. Fisher, M. Wang, Y. Ibrahim, B. Steffensmeier, and C. L. Cheung, “Effect of sodium nitrate on microwave-assisted synthesis of ceria nanocubes,” *Mater. Lett.*, vol. 178, pp. 71–74, 2016, doi: 10.1016/j.matlet.2016.04.186.
- [67] S. Patil and H. P. Dasari, “Effect of fuel and solvent on soot oxidation activity of ceria nanoparticles synthesized by solution combustion method,” *Mater. Sci. Energy Technol.*, vol. 2, no. 3, pp. 485–489, 2019, doi: 10.1016/j.mset.2019.05.005.
- [68] M. Piumetti *et al.*, “Nanostructured ceria-based materials: Effect of the hydrothermal synthesis conditions on the structural properties and catalytic activity,” *Catalysts*, vol. 7, no. 6, 2017, doi: 10.3390/catal7060174.
- [69] M. Piumetti, T. Andana, S. Bensaid, N. Russo, D. Fino, and R. Pirone, “Study on the CO Oxidation over Ceria-Based Nanocatalysts,” *Nanoscale Res. Lett.*, vol. 11, no. 1, 2016, doi: 10.1186/s11671-016-1375-z.
- [70] Z. Wu, M. Li, J. Howe, H. M. Meyer, and S. H. Overbury, “Probing defect sites on CeO<sub>2</sub> nanocrystals with well-defined surface planes by Raman spectroscopy and O<sub>2</sub> adsorption,” *Langmuir*, vol. 26, no. 21, pp. 16595–16606, 2010, doi: 10.1021/la101723w.
- [71] J. E. Spanier, R. D. Robinson, F. Zhang, S. W. Chan, and I. P. Herman, “Size-dependent properties of CeO<sub>2-y</sub> nanoparticles as studied by Raman scattering,” *Phys. Rev. B - Condens. Matter Mater. Phys.*, vol. 64, no. 24, pp. 1–8, 2001, doi: 10.1103/PhysRevB.64.245407.
- [72] A. K. P. Mann, Z. Wu, and S. H. Overbury, “The Characterization and Structure-Dependent Catalysis of Ceria with Well-Defined Facets,” in *Catalysis by Materials with Well-Defined Structures*, 2015, pp. 71–97.
- [73] S. Agarwal, X. Zhu, E. J. M. Hensen, L. Lefferts, and B. L. Mojet, “Defect chemistry of ceria nanorods,” *J. Phys. Chem. C*, vol. 118, no. 8, pp. 4131–4142, 2014, doi: 10.1021/jp409989y.
- [74] Z. Wu, M. Li, D. R. Mullins, and S. H. Overbury, “Probing the surface sites of CeO<sub>2</sub> nanocrystals with well-defined surface planes via methanol adsorption and desorption,” *ACS Catal.*, vol. 2, no. 11, pp. 2224–2234, 2012, doi: 10.1021/cs300467p.
- [75] S. Dey and G. C. Dhal, “Cerium catalysts applications in carbon monoxide oxidations,” *Mater. Sci. Energy Technol.*, vol. 3, pp. 6–24, 2020, doi: 10.1016/j.mset.2019.09.003.
- [76] M. Piumetti, S. Bensaid, N. Russo, and D. Fino, “Nanostructured ceria-based catalysts for soot combustion: Investigations on the surface sensitivity,” *Applied Catal. B, Environ.*, vol. 165, pp. 742–751, 2015, doi: 10.1016/j.apcatb.2014.10.062.
- [77] E. Aneggi, D. Wiater, C. De Leitenburg, J. Llorca, and A. Trovarelli, “Shape-Dependent Activity of Ceria in Soot Combustion,” *ACS Catal.*, vol. 4, pp. 172–181, 2014, doi: 10.1021/cs400850r.
- [78] A. Aranda *et al.*, “Total oxidation of naphthalene with high selectivity using a ceria catalyst prepared by a combustion method employing ethylene glycol,” *J. Hazard.*

- Mater.*, vol. 171, no. 1–3, pp. 393–399, 2009, doi: 10.1016/j.jhazmat.2009.06.013.
- [79] A. Trovarelli, “Structural and oxygen storage/release properties of CeO<sub>2</sub>-based solid solutions,” *Comments Inorg. Chem.*, vol. 20, no. 4–6, pp. 263–284, 1999, doi: 10.1080/02603599908021446.
- [80] Y. Borchert, P. Sonström, M. Wilhelm, H. Borchert, and M. Bäumer, “Nanostructured praseodymium oxide: Preparation, structure, and catalytic properties,” *J. Phys. Chem. C*, vol. 112, no. 8, pp. 3054–3063, 2008, doi: 10.1021/jp0768524.
- [81] G. V. Antoshin, K. M. Minachev, “Mobility of oxygen and catalytic properties of rare earth oxides with respect to oxidation of hydrogen,” *Russ. Chem. Bull.*, no. 16, pp. 1793–1795, 1967.
- [82] P. Sonström *et al.*, “Nanostructured praseodymium oxide: Correlation between phase transitions and catalytic activity,” *ChemCatChem*, vol. 2, no. 6, pp. 694–704, 2010, doi: 10.1002/cctc.200900311.
- [83] J. G. Kang, B. K. Min, and Y. Sohn, “Physicochemical properties of praseodymium hydroxide and oxide nanorods,” *J. Alloys Compd.*, vol. 619, pp. 165–171, 2015, doi: 10.1016/j.jallcom.2014.09.059.
- [84] A. Dodd, “Synthesis of praseodymium hydroxide (Pr(OH)<sub>3</sub>) and praseodymium oxide (Pr<sub>6</sub>O<sub>11</sub>) nanorods via room temperature aging,” *J. Colloid Interface Sci.*, vol. 392, no. 1, pp. 137–140, 2013, doi: 10.1016/j.jcis.2012.10.001.
- [85] A. D. Logan and M. Shelef, “Oxygen availability in mixed cerium/praseodymium oxides and the effect of noble metals,” *J. Mater. Res.*, vol. 9, no. 2, pp. 468–475, 1994, doi: 10.1557/JMR.1994.0468.
- [86] H. Borchert *et al.*, “Electronic and chemical properties of nanostructured cerium dioxide doped with praseodymium,” *J. Phys. Chem. B*, vol. 109, no. 12, pp. 5728–5738, 2005, doi: 10.1021/jp045828c.
- [87] T. Andana, M. Piumetti, S. Bensaid, N. Russo, D. Fino, and R. Pirone, “Nanostructured ceria-praseodymia catalysts for diesel soot combustion,” *Appl. Catal. B Environ.*, vol. 197, pp. 125–137, 2016, doi: 10.1016/j.apcatb.2015.12.030.
- [88] N. Guillén-Hurtado, J. Giménez-Mañogil, J. C. Martínez-Munuera, A. Bueno-López, and A. García-García, “Study of Ce/Pr ratio in ceria-praseodymia catalysts for soot combustion under different atmospheres,” *Appl. Catal. A Gen.*, vol. 590, no. July 2019, p. 117339, 2020, doi: 10.1016/j.apcata.2019.117339.
- [89] J. Giménez-Mañogil, N. Guillén-Hurtado, S. Fernández-García, X. Chen, J. J. Calvino-Gámez, and A. García-García, “Ceria-Praseodymia Mixed Oxides: Relationships Between Redox Properties and Catalytic Activities Towards NO Oxidation to NO<sub>2</sub> and CO-PROX Reactions,” *Top. Catal.*, vol. 59, no. 10–12, pp. 1065–1070, 2016, doi: 10.1007/s11244-016-0591-1.
- [90] E. Sartoretti, D. Fino, F. Martini, M. Piumetti, S. Bensaid, and N. Russo, “Nanostructured equimolar ceria-praseodymia for total oxidations in low-O<sub>2</sub> conditions,” *Catalysts*, vol. 10, no. 2, 2020, doi: 10.3390/catal10020165.
- [91] T. Andana *et al.*, “Nanostructured equimolar ceria-praseodymia for NO<sub>x</sub>-assisted soot oxidation: Insight into Pr dominance over Pt nanoparticles and metal–support interaction,” *Appl. Catal. B Environ.*, vol. 226, no. x, pp. 147–161, 2018, doi: 10.1016/j.apcatb.2017.12.048.

- [92] M. F. Luo, Z. L. Yan, and L. Y. Jin, "Structure and redox properties of  $Ce_xPr_{1-x}O_{2-\delta}$  mixed oxides and their catalytic activities for CO, CH<sub>3</sub>OH and CH<sub>4</sub> combustion," *J. Mol. Catal. A Chem.*, vol. 260, no. 1–2, pp. 157–162, 2006, doi: 10.1016/j.molcata.2006.07.012.
- [93] M. Piumetti, S. Bensaid, N. Russo, and D. Fino, "Investigations into nanostructured ceria-zirconia catalysts for soot combustion," *Appl. Catal. B Environ.*, vol. 180, pp. 271–282, 2016, doi: 10.1016/j.apcatb.2015.06.018.
- [94] S. Rossignol, C. Descorme, C. Kappenstein, and D. Duprez, "Synthesis, structure and catalytic properties of Zr-Ce-Pr-O mixed oxides," *J. Mater. Chem.*, vol. 11, no. 10, pp. 2587–2592, 2001, doi: 10.1039/b102763h.
- [95] M. Piumetti; T. Andana; S. Bensaid; D. Fino, N. Russo, "Ceria-based nanomaterials as Catalysts for CO oxidation and Soot combustion: Effect of Zr-Pr Doping and Structural Properties on the Catalytic Activity," *AIChE J.*, vol. 63, no. 1, pp. 216–225, 2016, doi: 10.1002/aic.
- [96] B. Palanisamy and B. Paul, "Continuous flow synthesis of ceria nanoparticles using static T-mixers," *Chem. Eng. Sci.*, vol. 78, pp. 46–52, 2012, doi: 10.1016/j.ces.2012.04.032.
- [97] S. Bensaid *et al.*, "Catalytic Oxidation of CO and Soot over Ce-Zr-Pr Mixed Oxides Synthesized in a Multi-Inlet Vortex Reactor: Effect of Structural Defects on the Catalytic Activity," *Nanoscale Res. Lett.*, vol. 11, no. 1, pp. 1–14, 2016, doi: 10.1186/s11671-016-1713-1.
- [98] M. Piumetti, S. Bensaid, T. Andana, N. Russo, R. Pirone, and D. Fino, "Cerium-copper oxides prepared by solution combustion synthesis for total oxidation reactions: From powder catalysts to structured reactors," *Appl. Catal. B Environ.*, vol. 205, pp. 455–468, 2017, doi: 10.1016/j.apcatb.2016.12.054.
- [99] T. Andana *et al.*, "CuO nanoparticles supported by ceria for NO<sub>x</sub>-assisted soot oxidation: insight into catalytic activity and sintering," *Appl. Catal. B Environ.*, vol. 216, pp. 41–58, 2017, doi: 10.1016/j.apcatb.2017.05.061.
- [100] R. K. Grasselli, "Genesis of site isolation and phase cooperation in selective oxidation catalysis," *Top. Catal.*, vol. 15, no. 2–4, pp. 93–101, 2001, doi: 10.1023/a:1016683117255.
- [101] P. Sudarsanam, B. Hillary, M. H. Amin, U. Bentrup, A. Brückner, and S. K. Bhargava, "Heterostructured Copper-Ceria and Iron-Ceria Nanorods : Role of Morphology , Redox , and Acid Properties in Catalytic Diesel Soot Combustion," *Langmuir*, 2018, doi: 10.1021/acs.langmuir.7b03998.
- [102] J. Ning, C. Dong, M. Li, Y. Zhou, and W. Shen, "Dispersion of copper oxide species on nanostructured ceria," *J. Chem. Phys.*, vol. 152, no. 9, 2020, doi: 10.1063/1.5143585.
- [103] S. Hosokawa, M. Taniguchi, K. Utani, H. Kanai, and S. Imamura, "Affinity order among noble metals and CeO<sub>2</sub>," *Appl. Catal. A Gen.*, vol. 289, no. 2, pp. 115–120, 2005, doi: 10.1016/j.apcata.2005.04.048.
- [104] R. Peng *et al.*, "Shape effect of Pt/CeO<sub>2</sub> catalysts on the catalytic oxidation of toluene," *Chem. Eng. J.*, vol. 306, pp. 1234–1246, 2016, doi: 10.1016/j.cej.2016.08.056.
- [105] T. Andana *et al.*, "Ceria-supported small Pt and Pt<sub>3</sub>Sn nanoparticles for NO<sub>x</sub>-assisted soot oxidation," *Appl. Catal. B Environ.*, vol. 209, no. x, pp. 295–310, 2017, doi: 10.1016/j.apcatb.2017.03.010.

- [106] “Carbon Dioxide Emissions Factor, kg CO<sub>2</sub> per MWh,” *Intergovernmental Panel on Climate Change (IPCC)*. <https://ourworldindata.org/grapher/carbon-dioxide-emissions-factor?year=latest> (accessed Sep. 06, 2020).
- [107] R. J. Farrauto, “Low-temperature Oxidation of Methane,” *Science (80-. )*, vol. 337, no. August, pp. 659–660, 2012, doi: 10.1007/s12239.
- [108] G. Zhu, J. Han, D. Y. Zemlyanov, and F. H. Ribeiro, “Temperature dependence of the kinetics for the complete oxidation of methane on palladium and palladium oxide,” *J. Phys. Chem. B*, vol. 109, no. 6, pp. 2331–2337, 2005, doi: 10.1021/jp0488665.
- [109] S. Colussi, A. Trovarelli, G. Groppi, and J. Llorca, “The effect of CeO<sub>2</sub> on the dynamics of Pd-PdO transformation over Pd/Al<sub>2</sub>O<sub>3</sub> combustion catalysts,” *Catal. Commun.*, vol. 8, no. 8, pp. 1263–1266, 2007, doi: 10.1016/j.catcom.2006.11.020.
- [110] S. Colussi, P. Fornasiero, and A. Trovarelli, “Structure-activity relationship in Pd/CeO<sub>2</sub> methane oxidation catalysts,” *Chinese J. Catal.*, vol. 41, no. 6, pp. 938–950, 2020, doi: 10.1016/S1872-2067(19)63510-2.
- [111] A. Hellman *et al.*, “The active phase of palladium during methane oxidation,” *J. Phys. Chem. Lett.*, vol. 3, no. 6, pp. 678–682, 2012, doi: 10.1021/jz300069s.
- [112] Y. Xin, S. Lieb, H. Wang, and C. K. Law, “Kinetics of catalytic oxidation of methane over palladium oxide by wire microcalorimetry,” *J. Phys. Chem. C*, vol. 117, no. 38, pp. 19499–19507, 2013, doi: 10.1021/jp4058302.
- [113] J. J. Willis *et al.*, “Systematic Structure-Property Relationship Studies in Palladium-Catalyzed Methane Complete Combustion,” *ACS Catal.*, vol. 7, no. 11, pp. 7810–7821, 2017, doi: 10.1021/acscatal.7b02414.
- [114] T. Guo, J. Du, and J. Li, “The effects of ceria morphology on the properties of Pd/ceria catalyst for catalytic oxidation of low-concentration methane,” *J. Mater. Sci.*, vol. 51, no. 24, pp. 10917–10925, 2016, doi: 10.1007/s10853-016-0303-z.
- [115] T. Guo, J. Du, J. Wu, S. Wang, and J. Li, “Structure and kinetic investigations of surface-stepped CeO<sub>2</sub>-supported Pd catalysts for low-concentration methane oxidation,” *Chem. Eng. J.*, vol. 306, pp. 745–753, 2016, doi: 10.1016/j.cej.2016.08.020.
- [116] M. M. Khader, M. J. Al-Marri, S. Ali, and A. G. Abdelmoneim, “Active and stable methane oxidation nano-catalyst with highly-ionized palladium species prepared by solution combustion synthesis,” *Catalysts*, vol. 8, no. 2, 2018, doi: 10.3390/catal8020066.
- [117] M. Danielis, S. Colussi, C. de Leitenburg, L. Soler, J. Llorca, and A. Trovarelli, “Outstanding Methane Oxidation Performance of Palladium-Embedded Ceria Catalysts Prepared by a One-Step Dry Ball-Milling Method,” *Angew. Chemie - Int. Ed.*, vol. 57, no. 32, pp. 10212–10216, 2018, doi: 10.1002/anie.201805929.
- [118] N. Guillén-hurtado, A. García-garcía, and A. Bueno-lópez, “Applied Catalysis B: Environmental Active oxygen by Ce – Pr mixed oxide nanoparticles outperform diesel soot combustion Pt catalysts,” *Applied Catal. B, Environ.*, vol. 174–175, no. 2, pp. 60–66, 2015, doi: 10.1016/j.apcatb.2015.02.036.
- [119] A. Bueno-López, K. Krishna, B. van der Linden, G. Mul, J. A. Moulijn, and M. Makkee, “On the mechanism of model diesel soot-O<sub>2</sub> reaction catalysed by Pt-containing La<sup>3+</sup>-doped CeO<sub>2</sub>. A TAP study with isotopic O<sub>2</sub>,” *Catal. Today*, vol. 121, no. 3–4, pp. 237–245, 2007, doi: 10.1016/j.cattod.2006.06.048.

- [120] R. Peng *et al.*, “Size effect of Pt nanoparticles on the catalytic oxidation of toluene over Pt/CeO<sub>2</sub> catalysts,” *Appl. Catal. B Environ.*, vol. 220, pp. 462–470, 2018, doi: 10.1016/j.apcatb.2017.07.048.
- [121] M. Monai, T. Montini, C. Chen, E. Fonda, R. J. Gorte, and P. Fornasiero, “Methane Catalytic Combustion over Hierarchical Pd@CeO<sub>2</sub>/Si-Al<sub>2</sub>O<sub>3</sub>: Effect of the Presence of Water,” *ChemCatChem*, vol. 7, no. 14, pp. 2038–2046, 2015, doi: 10.1002/cctc.201402717.
- [122] W. R. Schwartz, D. Ciuparu, and L. D. Pfefferle, “Combustion of methane over palladium-based catalysts: Catalytic deactivation and role of the support,” *J. Phys. Chem. C*, vol. 116, no. 15, pp. 8587–8593, 2012, doi: 10.1021/jp212236e.
- [123] Z. Wu, M. Li, and S. H. Overbury, “On the structure dependence of CO oxidation over CeO<sub>2</sub> nanocrystals with well-defined surface planes,” *J. Catal.*, vol. 285, no. 1, pp. 61–73, 2012, doi: 10.1016/j.jcat.2011.09.011.
- [124] V. Sánchez Escribano *et al.*, “A study of a ceria-zirconia-supported manganese oxide catalyst for combustion of Diesel soot particles,” *Combust. Flame*, vol. 153, no. 1–2, pp. 97–104, 2008, doi: 10.1016/j.combustflame.2007.11.010.
- [125] L. Soler *et al.*, “Ambient Pressure Photoemission Spectroscopy Reveals the Mechanism of Carbon Soot Oxidation in Ceria-Based Catalysts,” *ChemCatChem*, vol. 8, no. 17, pp. 2748–2751, 2016, doi: 10.1002/cctc.201600615.
- [126] C. Binet, M. Daturi, and J. C. Lavalley, “IR study of polycrystalline ceria properties in oxidised and reduced states,” *Catal. Today*, vol. 50, no. 2, pp. 207–225, 1999, doi: 10.1016/S0920-5861(98)00504-5.
- [127] S. Liu, X. Wu, D. Weng, M. Li, and R. Ran, “Roles of acid sites on Pt/H-ZSM<sub>5</sub> catalyst in catalytic oxidation of diesel soot,” *ACS Catal.*, vol. 5, no. 2, pp. 909–919, 2015, doi: 10.1021/cs5018369.
- [128] T. Andana, M. Piumetti, S. Bensaid, N. Russo, and D. Fino, “Heterogeneous mechanism of NO<sub>x</sub>-assisted soot oxidation in the passive regeneration of a bench-scale diesel particulate filter catalyzed with nanostructured equimolar ceria-praseodymia,” *Appl. Catal. A Gen.*, vol. 583, no. x, p. 117136, 2019, doi: 10.1016/j.apcata.2019.117136.
- [129] P. J. Jodłowski, R. J. Jędrzejczyk, D. Chlebda, M. Gierada, and J. Łojewska, “In situ spectroscopic studies of methane catalytic combustion over Co, Ce, and Pd mixed oxides deposited on a steel surface,” *J. Catal.*, vol. 350, pp. 1–12, 2017, doi: 10.1016/j.jcat.2017.03.022.
- [130] A. Filtschew and C. Hess, “Unravelling the mechanism of NO and NO<sub>2</sub> storage in ceria: The role of defects and Ce-O surface sites,” *Appl. Catal. B Environ.*, vol. 237, no. 2, pp. 1066–1081, 2018, doi: 10.1016/j.apcatb.2018.06.058.
- [131] R. Marques, P. Darcy, P. Da Costa, H. Mellottée, J. M. Trichard, and G. Djéga-Mariadassou, “Kinetics and mechanism of steady-state catalytic NO + O<sub>2</sub> reactions on Pt/SiO<sub>2</sub> and Pt/CeZrO<sub>2</sub>,” *J. Mol. Catal. A Chem.*, vol. 221, no. 1–2, pp. 127–136, 2004, doi: 10.1016/j.molcata.2004.06.023.



### 13. Acknowledgments

First of all, I would like to thank my supervisor Samir Bensaid for giving me the opportunity to carry out a thesis on such fascinating and engaging topics. Thank you so much for your willingness and your interest in my work. I would also like to thank my co-supervisor Marco Piumetti for his precious help in the IR spectroscopy. A heartfelt thanks to Enrico for all his lessons in the laboratory and for always being polite and available for advice and explanation during these last few months.

I would like to thank all the people who have been close to me during these five challenging years. In particular, thanks to my childhood friend Silvia who has come along with me from the admission test until today without ever abandoning me. She would do anything to see me happy. Thank you to Paolo and Vale for our laughter and the time spent together. Thanks to Michael for the work carried out together and to be present even though we have gone through different routes during this last year. Thank you so much to Nancy and Cesare for standing by me in my beautiful adventures and misadventures over the last two years. Lastly, thank you to Elena and Claudia.

A huge thank you to my parents, I am sure that I could have never got this far without them. Thank you to my mum Anna for being there for me in the hardest choices and for always having believed in me with absolutely no doubt. Thanks to my dad Franco for his support during the last few years. Thanks to you I have learned how to always do my best, to love what I do, no matter how simple or complicated things are, and to never give up in difficult times. Thank you to my grandmother Miranda for always being informed on my exams and, most importantly, on how much I eat. Thanks to my grandmother Anna for being by my side. Thanks to my cousin Denise who, besides being the youngest of the family, has been able to take care of me several times with her kind support and smile. Thanks to my uncle Max for our great conversations and helped me find new ways to grow more and more. A sincere thank you goes to my aunt Vilma for always being interested in the things I do and for her gentle speeches whenever I get to see her. Thank you to Aurora. Thanks to my godfather Gianni and my godmother Manuela for being with me over the last few years. Finally, thank you to my grandpa Luigi, who will always have a special place in my heart even if he cannot be here anymore.

Thank you, because as beautiful as today would be on its own, the presence of each one of you makes it even more special.



## 14. Acknowledgments – Italian version

Ringrazio prima di tutto il mio relatore Samir Bensaid per avermi dato la possibilità di svolgere la tesi su argomenti così interessanti e coinvolgenti, per la sua disponibilità e il suo interesse nel mio lavoro. Ringrazio, in particolar modo, il mio correlatore Marco Piumetti per il prezioso aiuto inerente alla spettroscopia IR. Un caro ringraziamento a Enrico per le lezioni in laboratorio e per essere stato sempre disponibile e gentile, durante questi mesi, per spiegazioni e chiarimenti.

Grazie a tutte le persone che mi sono state accanto in questi cinque impegnativi anni. In particolare, grazie a Silvia, la mia amica storica, che mi ha accompagnata dal test di ingresso fino ad oggi senza mai abbandonarmi e che farebbe di tutto pur di vedermi sempre felice. Grazie a Paolo e a Vale per le nostre risate e il tempo trascorso insieme. Grazie a Michael per i lavori svolti insieme e per essere presente nonostante quest'ultimo ci abbia fatto percorrere strade diverse. Grazie a Nancy e a Cesare per essermi stati accanto nelle belle e un po' meno belle esperienze di questi ultimi due anni. Grazie infine a Elena e a Claudia.

Un grazie immenso ai miei genitori, sono certa che senza di loro non sarei mai arrivata a questo punto. Grazie a mamma Anna per essermi stata vicina nelle scelte più difficili e per aver sempre creduto in me senza mai dubitare un momento. Grazie a papà Franco per il suo supporto durante questi anni. Grazie a te ho imparato a mettere tutta me stessa e ad amare le cose che faccio, siano esse semplici o complicate, e a non arrendermi di fronte ad ogni difficoltà. Grazie a nonna Miranda per essere stata sempre super informata sui miei esami e soprattutto su quanto mangio. Grazie a nonna Anna per essermi stata vicina. Grazie alla mia cuginetta Denise che, seppur la più piccina, ha dimostrato più volte di prendersi cura di me con il suo supporto e il suo sorriso. Grazie a zio Max per i nostri grandi discorsi e per cercare il modo di aiutarmi a crescere sempre di più. Un sincero grazie a zia Vilma per essere stata sempre interessata alle cose che faccio e ai suoi discorsi gentili quando salgo a trovarla. Grazie ad Aurora. Grazie a padrino Gianni e a madrina Manuela per essere stati presenti in questi anni. Grazie infine a nonno Luigi che, pur non potendo essere qui con noi, è sempre presente in un angolino del mio cuore.

Grazie perché, per quanto bello possa essere questo giorno, solo la presenza di ognuno di voi lo rende così speciale.